The Effects of Surface Finish on Piston Ring-pack Performance in Advanced Reciprocating Engine Systems

by

Jeffrey Jocsak

B.Sc., Mechanical Engineering
Queen's University at Kingston, 2003

Submitted to the Department of Mechanical Engineering in Partial Fulfillment of the Requirements of the Degree of

Masters of Science in Mechanical Engineering
at the
Massachusetts Institute of Technology

June 2005

Signature of Author: _____
Department of Mechanical Engineering
May 6, 2005

Certified by: _____
Dr. Tian Tian
Lecturer, Department of Mechanical Engineering
Thesis Supervisor

Certified by: _____
Dr. Victor W. Wong
Lecturer, Department of Mechanical Engineering
Thesis Supervisor

Accepted by: _____
Professor Lallit Anand
Chairman, Department Committee on Graduate Studies
Department of Mechanical Engineering

(This page was intentionally left blank)

The Effects of Surface Finish on Piston Ring-pack Performance in Advanced Reciprocating Engine Systems

by

Jeffrey Jocsak

Submitted to the Department of Mechanical Engineering on May 6, 2005 in Partial Fulfillment of the Requirements for the Degree of Master of Science in Mechanical Engineering

Abstract

Frictional losses in the piston ring-pack of an engine account for approximately 20% of the total frictional losses within an engine. Methods of surface texture optimization were investigated to reduce piston ring-pack friction and increase engine brake thermal efficiency. Adverse effects of surface texture optimization on engine oil consumption and durability were also considered.

Although many non-conventional cylinder liner finishes are now being developed to reduce friction and oil consumption, the effects of surface finish on ring-pack performance is not well understood. To enable the study of cylinder liner surface texture on predicted piston ring-pack performance, the description of surface texture in MIT's current ring-pack models was improved. Modifications were made to the asperity contact and oil flow resistance sub-models to enable a more accurate and more general description of surface texture. The accuracy of the new sub-models was validated with experimental results obtained from a ring reciprocating tester. With the use of these sub-models, ring pack friction reduction strategies were investigated. The effects of surface skewness, roughness, and honing cross-hatch angle were considered in detail.

The analytical results suggest that a negatively skewed surface finish, such as that produced by plateau honing, will lead to a ring-pack friction reduction relative to a conventionally honed surface. This predicted friction reduction was due to a decrease in rough surface asperity contact between the rings and liner. Additional friction reduction was predicted by decreasing the honing cross hatch angle. The smaller angle decreased friction by blocking lubricant flow transport between the ring and liner thereby increasing the lubricant's effective viscosity and the effective lubricant film thickness between the ring and liner. Both of these effects enabled more ring load to be supported by hydrodynamic pressure, reducing ring-pack friction. There are potential adverse effects related to these surface finish modifications including an increase in the engine's susceptibility to scuffing, and an increase in oil consumption. Nonetheless, these modifications in surface finish reduce predicted ring-pack friction by approximately 1-10%.

Thesis Supervisors:
Dr. Tian Tian (Lecturer, Department of Mechanical Engineering)
Dr. Victor W. Wong (Lecturer, Department of Mechanical Engineering)

(This page was intentionally left blank)

Acknowledgements

The contributions of many people have helped to make my time at MIT an enjoyable and rewarding experience. These contributions have given me many opportunities for development on both a personal and professional level.

First and foremost, I would like to thank my advisors, Dr. Tian Tian and Dr. Victor W. Wong, for their advice and guidance throughout the course of my work. I have learned a great deal through my exposure to Tian's depth of knowledge, insight, and logical and reasoned approach to problem solving. I am grateful to Dr. Wong for trusting in my abilities and giving me a great deal of autonomy in the development of my work. Through Dr. Wong's encouragement, I have had opportunities to continuously publish my and present my work, which has been one of the most important factors in my professional development while at MIT.

I would also like to thank the other people and organizations that have contributed significantly to my work over the past two years. Through my interaction with the members of the MIT Lubrication Consortium, I received exposure and feedback from my work that has greatly improved both the quality of my research and my experience at MIT. Thank you to the representatives from Volvo, Renault, PSA Peugeot Citroën, Dana Perfect Circle, and MAHLE, especially Dr. Eduardo Tomanik, for sharing their experiences and expertise with me. I was very fortunate to be exposed to the wealth of knowledge of the Consortium members. I would also like to thank Rick Donahue and Ed Reinbold from Waukesha Engine for their help throughout the project, and the United States Department of Energy for their financial support of the program.

There are also several people from the Sloan Automotive Laboratory that I would like to acknowledge. These people have made significant contributions to my research: Fiona McClure, Liang Liu, Yeunwoo Cho, Yong Li, and especially Grant Smedley for his advice and guidance from the first day I visited the Lab. I would like to extend a special thanks to Devon Manz for reviewing my work and providing invaluable technical feedback throughout the course of my research.

Finally, I would like to thank my family for their support throughout my time here, especially my brother Jamie, who served as my commission-free mathematical consultant.

(This page was intentionally left blank)

Table of Contents

(This page was intentionally left blank)

List of Figures

List of Tables

(This page was intentionally left blank)

1 Introduction

1.1 Sources of Friction in an Internal Combustion Engine

Mechanical losses in an internal combustion engine consume approximately 10% of the total energy in the fuel, and approximately 20% of engine mechanical losses can be contributed to losses in the piston ring pack, as is illustrated in Fig. 1.1 [1]. The piston and piston ring-pack are the two largest contributors to engine mechanical losses.

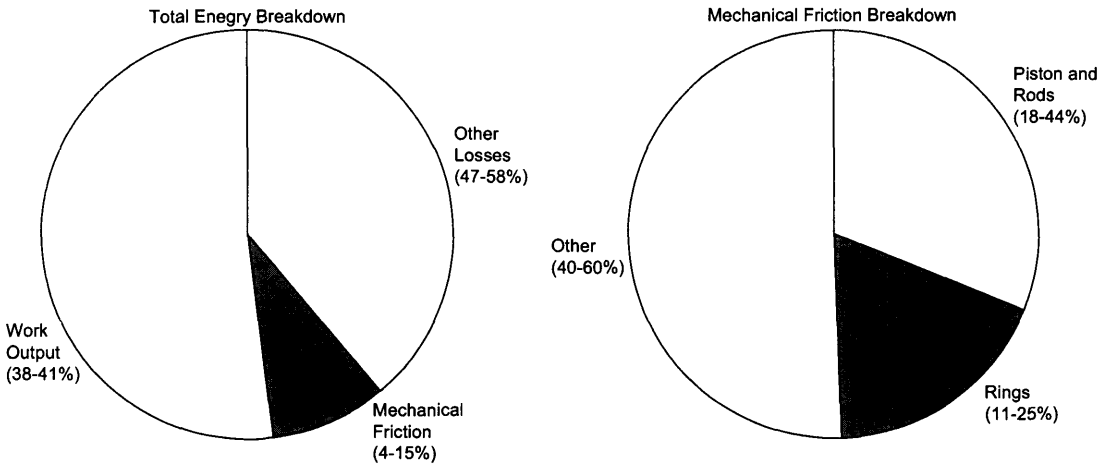

Fig. 1.1: Breakdown of total fuel energy usage and engine mechanical losses [1]

Therefore, friction reduction in the piston and piston ring-pack will produce greater gains in engine thermal efficiency than reducing other sources of mechanical friction by an equivalent amount. Reducing piston and piston ring-pack friction also reduces the thermal load on the cooling system of the engine by reducing the amount of heat generated in the power cylinder. The challenge in designing modern power cylinder systems is minimizing friction while maintaining engine durability and meeting increasingly stringent emissions standards.

1.2 The Piston Ring-pack

Piston rings are an integral component in the design of any piston-driven heat engine. The piston ring pack has three main functions within an internal combustion engine [2]:

1. The rings act as a seal, preventing excessive amounts of combustion gases from escaping the combustion chamber and entering into the crankcase.
2. The rings prevent lubricant from traveling into the combustion chamber, and being consumed in the combustion process.
3. The rings control piston temperature by transferring combustion heat away from the piston and to the cylinder liner, although this function is less important in recent high-output engines with an oil gallery in the piston for cooling.

The design of piston rings has evolved with the advances in engine power and, more recently, with increasingly stringent emissions standards. Recent improvements in piston ring design have necessitated a better theoretical understanding of the operating characteristics of the piston ring pack.

1.2.1 A Historical Perspective

The invention and use of piston rings far predate the industrial revolution. The Greeks were known to have used a sealed piston-cylinder system to raise water in 250 BC [3]. However, the development of such machines was abandoned during the Middle Ages in Europe, and the piston-cylinder system technology was not popularized until the 17th Century [4].

With the development of piston-driven engines throughout the 18th and 19th Centuries in Europe, first steam powered followed by internal combustion, the demands and requirements of the piston seal increased dramatically. Early piston rings were made of leather or hemp and lubricated with animal tallows. James Watt was the first to record the use of multiple piston seals in his steam engine design, to help minimize the leakage of pressure. This advance was effectively the invention of a piston ring-pack [4].

As the pressures and temperatures of steam engines, and subsequently internal combustion engines, increased, functional and durability concerns necessitated the development of metallic seals. Early metallic rings were typically made of brass or iron, and necessitated complex spring mechanisms to maintain a good seal between the ring and cylinder liner. The advent of the modern piston ring, which has a larger diameter than the bore of cylinder in free form, was invented by John Ramsbottom in 1854. The Ramsbottom ring, as it was known, used the elastic force of the ring to apply seal pressure when it was installed on the piston in the cylinder. The Ramsbottom ring quickly became the standard for piston ring design, became known simply as a piston ring, and was universally used by the beginning of the 20th Century [4].

Piston ring design in the 20th Century has been focused on design and material improvements to allow the piston ring to cope with increasing pressure, temperature, and durability requirements. The scientific study of piston rings began in the 1930's when engineers, in search of performance improvements, began to develop a fundamental understanding of the behavior of piston rings within an engine. Realization of the presence of hydrodynamic lubrication between the rings and liner during most of the stroke soon followed, which allowed for the optimization of basic ring parameters [5]. In the later half of the 20th Century, an increasingly complex understanding of piston ring-pack behavior was sought to control engine emissions and oil consumption. This quest led researchers to explore increasingly smaller scales of detail from the millimeter scale of piston ring dimensions to the micron scale of cylinder liner roughness. The understanding and optimization of small-scale effects, such as liner surface finish, has become the focus of researchers and engineers in order to meet future engine performance and durability requirements.

1.2.2 Modeling of the Piston Ring-pack

Substantial developments have been made by researchers in the past several decades that have led to a better understanding of the behavior of the piston rings and their effect on engine performance. The focus of this work has been on the modeling of lubricant behavior between the piston rings and liner, and the modeling of piston ring dynamics and gas flow within the power cylinder system.

Early work in piston ring-pack lubrication focused on modeling the piston rings under hydrodynamic lubrication with little attention given to mixed lubrication or boundary lubrication conditions [5]. Advancements were made in ring-pack modeling with the inclusion of lubricant continuity between the rings in the ring-pack, and the inclusion of a cavitation boundary condition at the fluid separation location on the ring that accounted for the tendency of saturated air to leave oil at sub-ambient pressure. Rough surface contact between the ring and liner was first incorporated into a ring-pack model using a stochastic description of surface roughness [6]. The importance of ring dynamic behavior, including ring twist, on ring lubrication behavior highlighted the need for a complete piston and ring-pack dynamic and gas flow model to accurately describe ring-pack lubrication [7].

Thus, researchers focused on the modeling of piston ring dynamics and gas flow. Ring-pack conditions, including inter-ring gas pressures and instantaneous ring twist along the cycle, are required to adequately describe ring-pack lubrication. Various models were developed that coupled the effects of piston tilt, piston ring dynamic behavior and gas flow to predict instantaneous ring-pack conditions throughout the stroke [8, 9].

Recently, the ring-pack lubrication model developed by Tian at MIT incorporated a detailed description of geometry, including ring profiles and ring twist, starved and unsteady inlet and exit conditions for each ring, and continuity along the liner and between the individual rings [10]. Complementary to the ring-pack lubrication model is a ring-pack dynamics and gas flow model that is capable of predicting inter-ring gas pressures and ring twist as inputs into the aforementioned ring-pack lubrication model [11].

1.2.3 Studies on Cylinder Liner Surface Finish

The understanding of small-scale effects, on the order of microns, on piston ring-pack performance has become necessary to improve ring-pack friction and oil consumption. There has been significant effort devoted to both experimental and analytical research on the effects of liner finish on various aspects of ring-pack performance.

The inclusion of surface roughness effects in ring-pack models became possible as usable tribological models were developed to describe rough surface interaction. The advent of stochastic asperity contact models enabled the inclusion of mixed and boundary lubrication into ring-pack models that previously considered only purely hydrodynamic lubrication [6, 12]. Statistical contact models are a practical method of determining asperity contact pressure between the ring and liner for a given mean separation of the contact surfaces, and are presently

the most common method of modeling mixed and boundary lubrication regimes. Greenwood and Tripp's asperity contact model for two nominally flat, rough surfaces is a common model used by researchers to account for asperity contact in modeling the piston ring-pack [12]. The development of flow factors by Patir and Cheng enabled the effect of surface roughness on oil flow behavior, believed to be especially important in understanding oil consumption, to be included in ring-pack modeling. Flow factors adjust the solution of the Reynolds equation for the effects of surface roughness [13]. However, both asperity contact and flow resistance models were typically applied assuming Gaussian surface roughness.

Numerous experimental studies have been conducted that analyze the effects of different cylinder bore finishes on ring-pack performance [14-16]. Recently, particular attention has been paid to the effect of surface finish on oil consumption [15, 16]. The experimental results suggest that smooth, plateau surface finishes offer the lowest friction, oil consumption, and wear. However, an increase in scuffing susceptibility was also observed with smooth plateau surface finishes.

Recently, there have been analytical studies on the effect of various liner surface finishes on ring-pack performance. Analytical studies have focused on relaxing the previously accepted assumption of Gaussian surface roughness and have varied the character of surface finish in addition to simply analyzing the effect of surface root-mean-square (RMS) roughness [17, 18]. These studies have found that the detailed nature of the surface finish plays an important role in ring friction and oil film thickness predictions. However, analytical modeling, and the corresponding fundamental understanding, has generally lagged the experimental research. Thus, many of the results seen experimentally have not been verified in an analytical fashion. Additionally, there appears to be very little evidence in the literature, experimentally or analytically, on the effect of anisotropic surface characteristics, such as honing groove cross-hatch angle, on friction.

1.3 Surface Finish on Modern Cylinder Liners

1.3.1 Cylinder Bore Honing

The final surface finish on a cylinder bore is created by a process known as honing. Honing is an operation designed to create a controlled surface finish on the cylinder liner. Typically a series of fine abrasive honing sticks, or stones, are attached to a rotating honing head. The honing sticks are spring loaded and the honing head is allowed to float, allowing a uniform loading pressure to be applied to the honing sticks as they drag along the bore surface, ensuring a consistent finish. A typical cylinder liner honing tool is shown in Fig. 1.2.

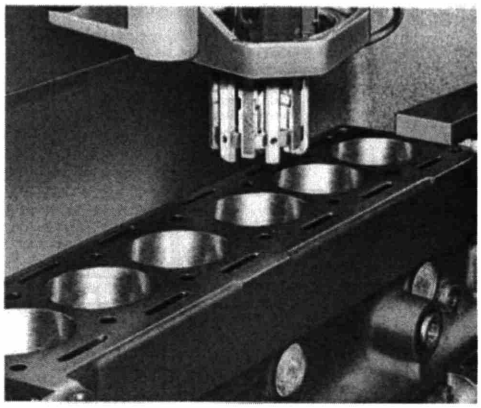

Fig. 1.2: Cylinder bore honing tool [19]

The honing head is fed into and out of the cylinder bore as is rotates. The ratio of the tool's feed and speed control the honing cross hatch angle created by the abrasive particles as they advance in a helical fashion down then up the cylinder bore, as is shown diagrammatically in Fig. 1.3.

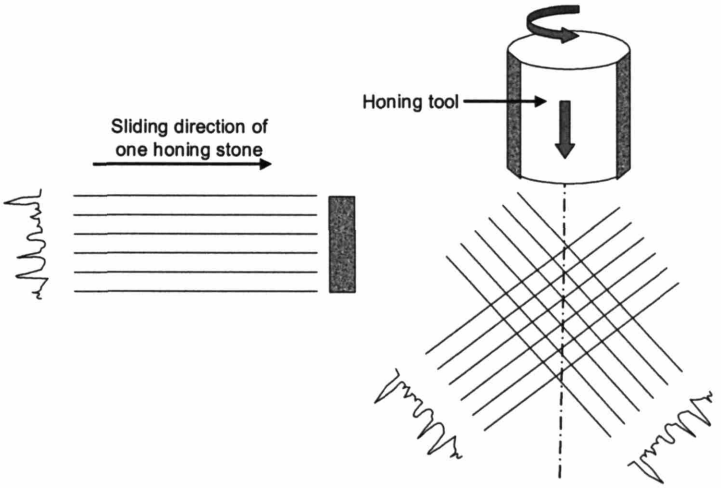

Fig. 1.3: Simplified honing process layout

The surface finish created by the honing process is controlled by the size and dispersion of abrasive particles adhered to the surface of the honing sticks. Modern cylinder liners are typically honed using a sequence of passes with successively finer abrasives. The first honing step uses a relatively rough abrasive and creates deep scratches along the liner surface. The high peaks of the scratches are removed by the following honing steps using successively finer abrasives. The end surface profile created typically contains deep valleys, corresponding to the first honing step, with a flat smooth surface as a result of the final honing steps. Such a surface, referred to as plateau, is shown in Fig. 1.4, and is thought to reduce engine break-in time and improve ring-pack performance [20,21].

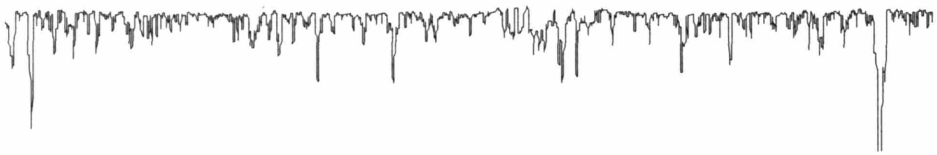

Fig. 1.4: Typical plateau honing finish

1.3.2 Classifying Cylinder Liner Finishes

Cylinder liner surface roughness character can differ between surfaces with the same RMS roughness. This difference can have a significant effect on the performance and behavior of the surface within the piston ring-pack system. Recently, there have been attempts made to better characterize liner roughness in terms of key parameters, in addition in RMS roughness, that affect its performance within the power cylinder. The rough surface analysis detailed in Deutsches Instutut fur Normung DIN 4776 is a common method used in the engine industry to improve the characterization of surface roughness, and it is summarized below.

The methodology outlined in DIN 4776 is based on the analysis of a bearing curve, which is simply a plot of the cumulative probability distribution of surface roughness height. A bearing curve can be separated into discrete peak, core, and valley regions, and is shown qualitatively in Fig. 1.5.

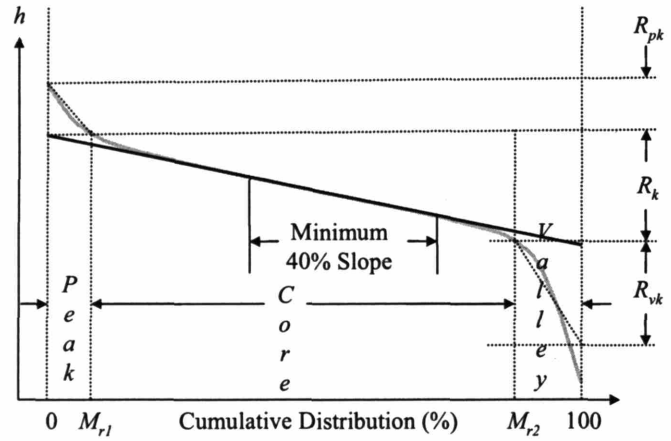

Fig. 1.5: Illustration of bearing curve analysis outlined in DIN 4776

In Fig. 1.5, h is the height from the mean of the surface. Rk is defined by extending over the whole distribution the secant line that has the minimum slope for 40% of the distribution. Rk represents the span of height that falls into the core region of the distribution, which is the region that bears most of the applied load. M_{r1} is the percentage of the distribution in the peak region of the distribution and M_{r2} is the percentage of the distribution that lies above the valley region of the distribution. The peak and valley heights, R_{pk} and R_{vk} respectively, are defined as the height of the triangle that has the equivalent area as the peak and core tails of the bearing curve, respectively. The peak height is an estimate of the typical height of a peak above the core region of the distribution, which will likely wear down over the life of the surface. The valley height is an estimate of the typical depth of valley available to retain lubricant.

There is an alternate standard in existence that is also designed for the characterization of cylinder liner surface roughness using bearing curve analysis. The standard ISO 1365-3 divides the surface roughness into peak and core Gaussian roughness regions that are characterized by the RMS roughness values R_{pq} and R_{vq}, respectively, and defines a transition height between the two regions, R_{mq}. The R_{pq} and R_{vq} correspond roughly to the R_{pk} and R_{vk} values of the DIN 4776 definition. In the following work, the DIN 4776 standard has been chosen, somewhat arbitrarily, to characterize the surfaces analyzed.

Both of the methodologies described enable cylinder liner surface roughness to be characterized in terms of parameters that affect the function of surface within the lubricated conditions present in the power cylinder. It should be noted that bearing curve analysis is one-dimensional, and provides no information about the spatial characteristics of surface roughness.

1.3.3 Production Cylinder Liner Finishes

Increasingly stringent engine emissions standards and power requirements are driving an evolution in cylinder liner surface finish [22]. The standard, or conventional, honed surface is being substituted by other surface finishes with the goal of reducing oil consumption, friction, and wear. In general, these surface finishes tend to be smoother than conventional cylinder liner finishes. Figure 1.6 shows typical fax films of different surface finishes currently in production in diesel engines [23]. Referring to Fig. 1.6, it can be seen that new surface finishes, such as those produced by slide and plateau honing, are smoother than a standard honed surface but still contain relatively deep valleys.

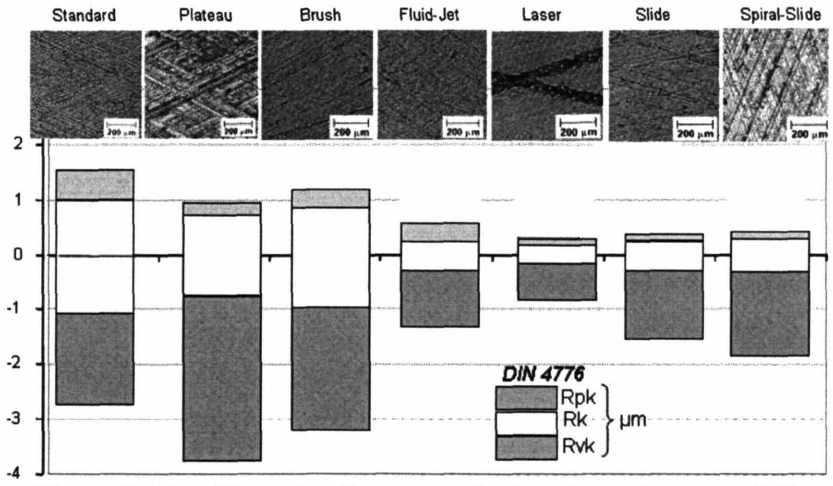

Fig. 1.6: Fax film of different cylinder liner finishes [23]

The full effect of different cylinder liner finishes on ring-pack performance is not well understood. Plateau and slide honed surface liners have been shown experimentally to be more susceptible to scuffing failure. In addition, there is little known about the effects of varying surface anisotropic characteristics, such as honing cross-hatch angle, on ring-pack performance.

1.4 Scope of Thesis Work

The purpose of this work was to investigate the effects of cylinder liner surface finish character on ring-pack performance. Using MIT's current ring-pack dynamic and friction models as a basis, improved sub-models describing rough surface contact and lubricant flow resistance were developed and verified experimentally. These sub-models allowed the inclusion of accurate rough surface textures into the ring-pack model, including surface spatial features such as honing angle. Thus, a tool was developed that was capable of analyzing the performance of a given three-dimensional surface finish on the performance of a given piston ring-pack.

The improved ring-pack model, including the improved surface sub-model, was used to develop ring-pack friction reduction strategies through the optimization of surface texture. Potentially adverse effects of these strategies on ring-pack durability and oil consumption were also considered. An analysis of the effects of friction between the piston ring and groove on ring-pack performance is presented in the final section of this work.

2 Fundamentals of Piston Ring-pack Performance

2.1 The Piston Ring-pack

The piston ring-pack is a vital component in the efficient and reliable operation of an internal combustion engine. Lubrication is supplied to the piston ring-pack by flooding the cylinder liner with lubricant below the position of the oil control ring. A diagram of a typical piston ring-pack is shown in Fig. 2.1.

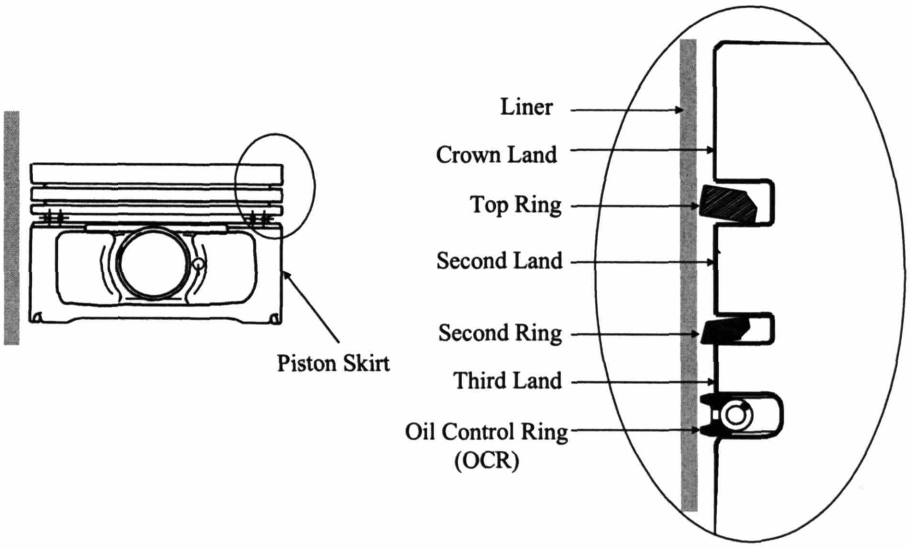

Fig. 2.1: Typical piston ring-pack

A typical piston ring-pack in both gasoline and diesel engines contains three rings: an oil control ring, a second or scraper ring, and a top or compression ring. The typical design of each ring and its intended functions within the piston ring-pack are described below.

The oil control ring (OCR) is the ring situated lowest down on the piston, closest to the piston skirt. Oil control rings are composed of two or three separate components depending on the design of the ring. Typically there are two thin rails that contact the liner and a separate supporting spring that applies radial loading. The oil control ring's primary purpose is the control of lubricant transported to the two rings above it. Sufficient lubricant must be supplied to the top two rings to provide adequate lubrication, without allowing a high rate of oil consumption. To ensure good conformability between the ring and liner despite the absence of high gas pressures behind the ring, the OCR is typically the highest tension ring in the ring-pack. As a result, the OCR typically contributes half of the total ring-pack friction.

The top ring is the ring situated highest up on the piston, closest to the piston crown. Typically having a single barrel-shaped ring profile, the primary purpose of the top ring is to prevent blow-by of high pressure and temperature combustion gases into the crankcase. Since the top ring is farthest away from the oil control ring, the top ring is typically starved of lubrication during parts

of the stroke. Lack of lubrication combined with high gas pressures present behind ring during the expansion stroke creates severe lubrication conditions for the top ring during parts of the engine cycle. As a result, it tends to be the most susceptible to scuffing failure.

The scraper ring is situated between the OCR and top ring on the piston. The scraper ring's cross-section is very close to a wedge in its general shape with the lower edge of the ring closest to the cylinder liner, as is shown in Fig. 2.1. This type of ring is usually referred to as a Napier style ring. The scraper ring supports both the OCR ring and top ring in their functions. The scraper ring helps to control the amount of lubricant supplied to the top ring and minimize the amount of lubricant that is consumed in the combustion chamber, which results in oil consumption. In addition, the scraper ring helps prevent blow-by of combustion chamber gases that have breached the top ring. As a result of greater oil supply and lower gas pressures than the top ring, the contribution of the scraper ring to ring-pack friction is typically small.

2.2 Modes of Lubrication

Piston rings experience a wide range of lubrication conditions as a result of the reciprocating nature of the piston, high gas pressures present during parts of the stroke, and limited lubricant supply. Piston rings will typically experience a full range of lubrication conditions, ranging from fully hydrodynamic lubrication to boundary lubrication during an engine cycle. The three lubrication regimes are illustrated in Fig. 2.2 and described in detail below.

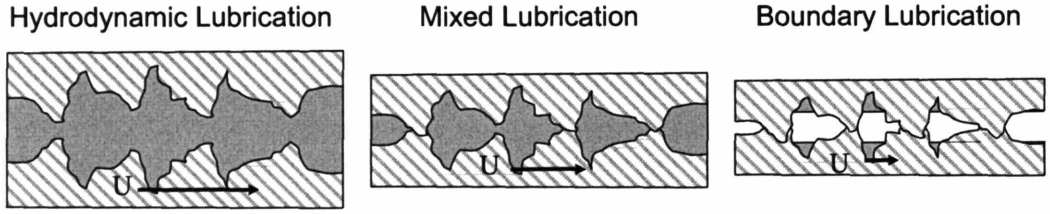

Fig. 2.2: Different modes of lubrication

Hydrodynamic lubrication is present between a ring and liner when the oil film thickness is sufficiently large to prevent contact between the two surfaces. Under this lubrication regime, sufficient hydrodynamic pressure is generated to carry the ring load. Hydrodynamic lubrication is typically present during mid-stroke conditions when sufficient lubrication is present, and sliding speeds are relatively high.

Boundary lubrication is present between a ring and liner when insufficient lubrication is available to wet the ring. Under this lubrication regime, no hydrodynamic pressure is present, and ring load is carried by rough surface contact. Boundary lubrication typically occurs near the top of the piston's stroke, when piston speeds are low and gas pressure is high. Under this regime, friction is proportional to ring load, analogous to dry surface contact.

Mixed lubrication is occurs when both lubricant and rough surface contact is present between the ring and liner. Under this regime, ring load is carried by a combination of hydrodynamic

pressure generated in the lubricant film and rough surface contact. Mixed lubrication is a transition regime between boundary and hydrodynamic lubrication.

2.3 Overview of Piston Ring-pack Modeling Tools

The current work was based on a previously developed MIT mixed-lubrication ring-pack model that has been used extensively in the automotive industry in predicting piston-ring/liner oil film thickness, friction, and oil-transport processes along the liner. The model considers three lubrication regimes, shear thinning of the lubricant, and the unsteady ring wetting conditions at the leading and trailing edges of the ring. The model incorporates the effects of surface roughness using Patir and Cheng's average flow model and the Greenwood and Tripp statistical asperity contact model, assuming a Gaussian distribution of surface roughness. The model is axis-symmetric, and considers hydrodynamic, mixed, and boundary lubrication regimes [10].

Due to the complex geometry and behavior of the oil control ring, which are usually made of two or three separate pieces as was described in Section 2.1, oil control ring friction and dynamics are determined using a separate program [24]. However, the lubrication between the oil control ring and liner is solved for in an identical manner as the MIT ring-pack model. Details of the underlying theory are given below.

2.3.1 Governing Equations

A two-dimensional axis-symmetric lubrication model requires simultaneous solution of momentum conservation equations in the axial and radial directions of the cylinder, and lubricant mass conservation in the axial direction of the cylinder between the ring and liner. The ring inertial force in the radial direction is neglected because ring acceleration in the radial direction is negligible compared to the other radial forces acting on the ring. Therefore, a quasi-steady force balance is assumed in the radial direction. The ring load experienced by a single ring, which is the summation of gas pressure acting against the back of the ring and ring tension, is counteracted by a combination of asperity contact pressure, lubricant hydrodynamic pressure, and gas pressure acting on the running face of the ring. This is shown schematically in Fig. 2.3.

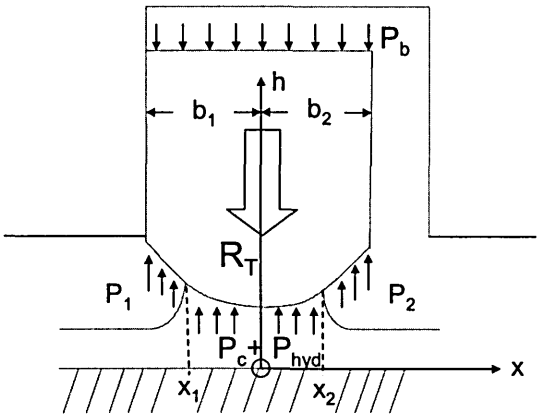

Fig. 2.3: Model layout for each piston ring

In Fig. 2.3, P_b, P_1, and P_2 are the gas pressures acting on the back of the ring and on the running surfaces of the ring, respectively, x_1 and x_2 are the attachment and detachment locations of the lubricant from the ring, respectively, and b_1 and b_2 are the widths of each ring half relative to the origin of the x-axis, respectively. P_c and P_{hyd} are the load supporting pressures developed by asperity contact and hydrodynamic shear. The radial force balance on the ring is

$$\sum F_{radial} \approx 0,$$
$$\int_{x_1}^{x_2} P_{hyd}\,dx + \int_{-b_1}^{b_2} P_c\,dx + P_1(b_1 + x_1) + P_2(b_2 - x_2) - (R_T + P_b)\cdot(b_1 + b_2) = 0. \tag{2.1}$$

Depending on lubrication conditions, either asperity contact pressure or hydrodynamic pressure may not be present. During a mixed lubrication regime, both carry ring load. The lubricant flow in the axial direction of the cylinder is highly viscous. Thus, the lubricant axial momentum and mass balances can be represented by the Reynolds equation. In this work, the Reynolds equation was modified to include the effects of surface roughness,

$$\frac{\partial}{\partial x}\left(\phi_p \frac{h^3}{\mu}\frac{dp}{dx}\right) = 6U\frac{\partial}{\partial x}\left(h\cdot\phi_g + R_q\cdot\phi_s\right) + 12\frac{\partial h}{\partial t}, \tag{2.2}$$

where U is the ring sliding velocity, h is the local nominal film thickness, μ is fluid dynamic viscosity, R_q is the surface roughness, and ϕ_p, ϕ_g, and ϕ_s are factors developed by Patir and Cheng that account for the effects of surface roughness on lubricant flow [13]. These factors are discussed in detail in Section 3.4. The Reynolds equation is applied between the fluid attachment and detachment locations on each ring.

It is also important to include the dynamic behavior of the piston rings to arrive at accurate predictions of ring-pack oil film thickness and friction. Static and dynamic twists of the ring, piston tilt, and bore distortion alter the effective ring running face profile. This in turn can have a significant effect on ring-pack performance predictions.

2.3.2 Boundary Conditions

It is necessary to prescribe the appropriate boundary conditions in applying the Reynolds equation to the fluid flow between each ring and the cylinder liner. It is assumed that the fluid pressure is uniform and equal to the adjacent gas pressure at both the inlet and exit of the ring,

$$p(x_1) = P_1,$$
$$p(x_2) = P_2. \tag{2.3}$$

The Reynolds equation predicts the existence of negative lubricant pressures on divergent portions of a ring face profile. In reality, dissolved air in the lubricant may leave solution, resulting in cavitation and effectively preventing the local oil pressure from dropping below the

lubricant saturation pressure, which is typically similar to ambient pressure [25]. Therefore, as has been done for the solution of journal bearings, Reynolds exit condition,

$$\left(\frac{dP}{dx}\right)_{x=x_2} = 0, \tag{2.4}$$

is applied at the fluid detachment point on the ring face. This boundary condition conserves mass at the fluid detachment location of the ring and prevents sub-ambient lubricant pressures.

Reynolds exit condition is valid throughout most of the piston's stroke, when the exit of the piston ring is starved. As piston sliding speed approaches zero, near the ends of the piston's stroke, the piston ring exit will typically flood, provided that sufficient lubrication is present, because unsteady "squeeze" flow begins to dominate. Under these conditions a fluid non-separation condition is assumed at the exit location of the ring, with fluid accumulating at the trailing edge of the ring.

Continuity at the inlet of each ring is maintained by solving the rings sequentially each stroke, starting with the leading ring. The inflow condition for each ring in the ring pack at a given location on the liner is dependant on the oil film left by the last ring to pass that location, with the exception of the oil control ring on the downstroke, which is assumed to be flooded with lubricant. Thus, the oil distribution along the section of liner traversed by the rings is carefully tracked throughout the entire engine cycle. Further details on MIT's piston ring-pack lubrication model can be found in [10].

2.3.3 Ring-pack Friction

Total ring pack friction is determined by summing the friction due to asperity contact and hydrodynamic friction. Asperity contact friction is given by

$$F_{f,asp} = \int_{ring\ running\ face} a_{bc} P_{asp} dA, \tag{2.5}$$

where $F_{f,asp}$ is the friction due to asperity contact, and a_{bc} is the coefficient of friction for boundary lubrication. Hydrodynamic friction is given by

$$F_{f,hyd} = \int_{ring\ wetted\ area} \left[\frac{\mu U}{h}\left(\phi_{fg} + \phi_{fs}\right) - \phi_{fp} \frac{h}{2}\frac{dP}{dx} \right] dA, \tag{2.6}$$

where ϕ_{fp}, ϕ_{fg}, and ϕ_{fs} are factors developed by Patir and Cheng that account for the effect of surface roughness on hydrodynamic friction, which are discussed in detail in Section 3.4.

2.3.4 Modeling Uncertainties

MIT's current ring-pack lubrication program carefully tracks lubricant transport along the cylinder liner. However, lubricant transport can also occur through the piston ring grooves, and ring gap. In addition, oil can accumulate on the piston lands during engine operation. As a result, the exact oil supply condition to the scraper ring is uncertain, and is the subject of ongoing research. For this work, the oil control ring profile was chosen to ensure that the scraper ring is flooded on the downstroke. This oil supply condition is discussed in detail in [26]. Therefore, all piston ring-pack friction and oil film thickness results given for the scraper and top ring assume that the scraper ring is under this supply condition.

In addition, all engine analyses performed in the work using the ring-pack models, which are axis-symmetric, considered the ring-cross section inline with the piston pin. The behavior of the ring at this cross-section is simplified because the effects of piston tilt are negated. Piston tilt changes the effective ring profile at different ring cross-sections around the circumference of the piston. Although the results presented in this work will vary depending on the piston circumferential location considered, the general trends seen in the following analysis will be unaffected by circumferential location. The trends are dependent on surface finish characteristics, not ring profile.

3 Modeling of Surface Roughness

Surface texture affects asperity contact pressure generation and oil flow between the rings and liner. In accounting for the effect of surface roughness on ring-pack friction, it has typically been assumed that the surface roughness on the cylinder liner is isotropic and Gaussian in nature. In reality, the normal running-in of a cylinder liner typically leaves a surface that is anisotropic and highly non-Gaussian in nature. Therefore, the classical assumption of Gaussian isotropic surface roughness is not generally applicable to cylinder liner surfaces.

Two new approaches are developed, which can characterize the contact and oil flow resistance behavior of a given cylinder liner surface. The first approach employs a stochastic description of surface roughness, and requires only discrete statistical parameters as input. This approach is appropriate for parametric studies, or when a detailed description of the liner surface is not available. The second approach employs a deterministic description of surface roughness, and requires detailed information on the surface texture as input. This approach is necessary if three-dimensional surface effects are to be analyzed accurately.

3.1 Stochastic Surface Roughness Characterization

In many practical situations, a detailed description of piston ring and liner surface texture is not available. In such circumstances, a statistical approach to the characterization of surface texture may be appropriate. Using this approach, surface roughness is characterized utilizing discrete statistical parameters known for the surface and the probability distribution function that describes the surface roughness, which can be inferred from these parameters.

3.1.1 Statistical Parameters

In addition to root-mean-square roughness, skewness and kurtosis are two statistical parameters that can be used to quantify the nature of a surface. Standard deviation or RMS roughness (σ), skewness (Sk) and kurtosis (Ku) are defined below:

$$\sigma = \sqrt{\int_{-\infty}^{\infty} y^2(z)\phi(z)dz}\,, \tag{3.1}$$

$$Sk = \frac{1}{\sigma^3}\int_{-\infty}^{\infty} y^3(z)\phi(z)dz\,, \tag{3.2}$$

and

$$Ku = \frac{1}{\sigma^4}\int_{-\infty}^{\infty} y^4(z)\phi(z)dz, \tag{3.3}$$

where $y(z)$ is the distance from the mean of the distribution and $\phi(z)$ is probability distribution function of the distribution, normalized to give a total population of unity,

$$\int_{-\infty}^{\infty} \phi(z)dz = 1. \tag{3.4}$$

Skewness is a measure of the distance between the mean and mode, the asymmetry, of a distribution. Kurtosis is a measure of the "peaked ness" of a distribution. A Gaussian probability density function is symmetric about its mean (zero skewness), and has a kurtosis value of three. Figure 3.1 demonstrates the effect of skewness on surface roughness profiles.

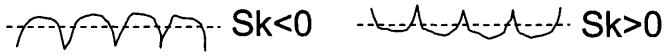

Fig. 3.1: The effect of skewness on roughness profiles

A surface with a negatively skewed, or plateau, profile generally has deep valleys and flat peaks. As a result, a large portion of the surface bearing area is concentrated slightly above the surface mean height. A surface with high kurtosis generally contains high peaks or deep valleys.

3.1.2 Pearson System of Frequency Curves

The Pearson system of frequency curves is a curve-fitting method that infers the shape of a probability distribution function in terms of its standard deviation, skewness and kurtosis. The probability distribution of surface roughness can be estimated using the Pearson system of frequency curves provided that the skewness, kurtosis, and RMS roughness of the surface are known. Implementation of the system of frequency curves follows the same methodology as has been done in the literature [27,28], and is detailed in Appendix A. Probability distribution functions with different values of skewness, and a kurtosis equal to three, are illustrated in Fig. 3.2. In Fig. 3.2, h is surface height. Probability density functions for a wide range of skewness and kurtosis values can be generated using the Pearson system of frequency curves.

3.2 Deterministic Surface Texture Characterization

If a more accurate description of surface texture is necessary and practical, a deterministic description of surface finish may be used. A deterministic approach requires a detailed knowledge of the rough surface topography. Measurement of real cylinder liner surface profiles is necessary to describe the surface deterministically. Asperity contact can be described with the use of a two-dimensional or three-dimensional surface, while oil flow resistance requires a three-dimensional surface profile for analysis.

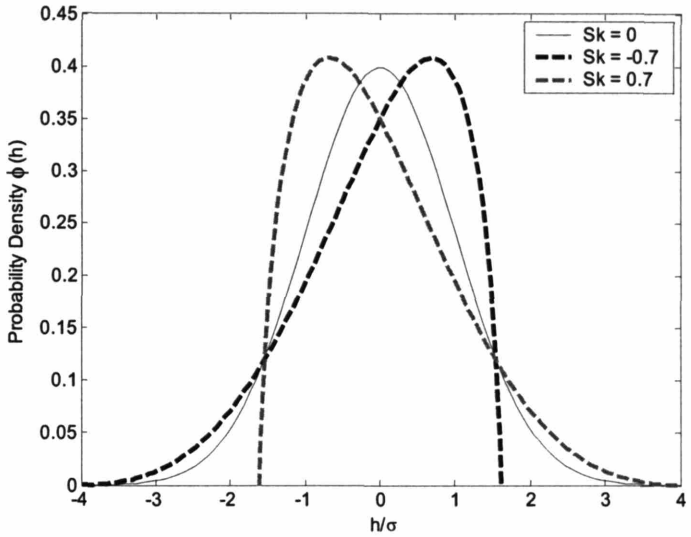

Fig. 3.2: Probability density functions (*Ku* = 3)

3.2.1 Two-Dimensional Surface Measurement

A linear trace of surface roughness is obtained using a profilometer, which measures the profile of a rough surface by accurately measuring the vertical motion of a stylus that is swept across a section of the surface. The precision of the profilometer is limited by the radius of the tip of the stylus [29]. Therefore, it is important that the radius of the stylus tip is smaller than radii of the asperity peaks present on the rough surface being measured. A picture of a typical portable profilometer and a profilometer trace is shown in Fig. 3.3.

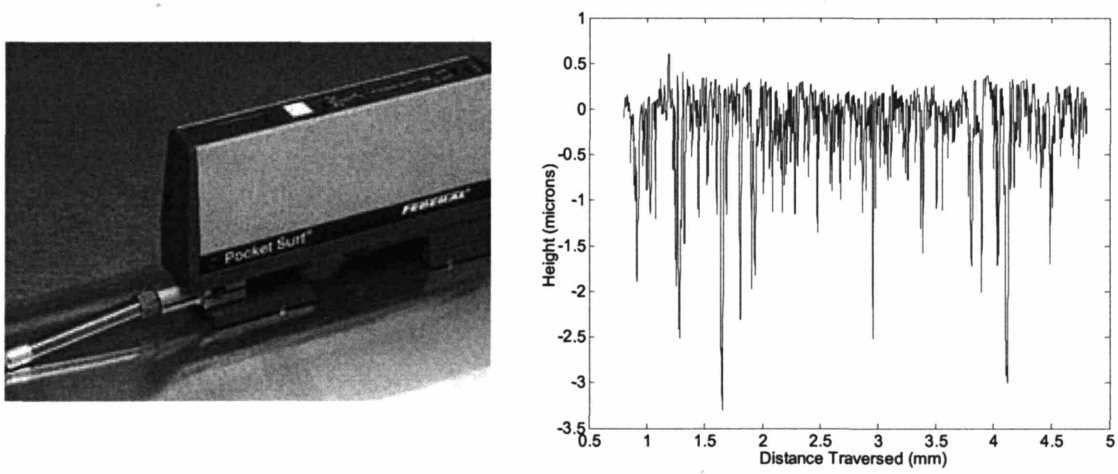

Fig. 3.3: Typical profilometer and trace

An underlying assumption in using a two-dimensional profilometer trace is that the surface trace provides a good representation of the liner surface.

3.2.2 Three-Dimensional Surface Measurement

A three-dimensional surface measurement of the cylinder liner finish is typically obtained with by using a two-axis profilometer or White Light Interferometry (WLI). A two-axis profilometer measures a surface through a series of line measurements, as were described in Section 3.2.1. This method tends to be slow and limited by the radius of the stylus tip. WLI measurement is an optical measurement process that uses the reflectivity of a metal specimen and the resulting intensity of the reflected light to gain an accurate measurement of distance. This distance measurement can be used to determine surface texture quickly without contacting the surface. WLI measurement systems can experience measurement difficulties as a result of contaminants on the measured surface, or sharp grooves that do not receive enough reflected light [29]. A reproduction of a typical surface measured using WLI is shown in Fig. 3.4.

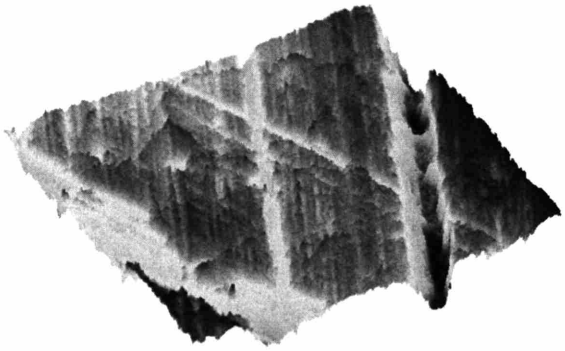

Fig. 3.4: WLI surface measurement

An accurate three-dimensional surface measurement is required to determine the effect of surface texture on lubricant flow characteristics. As with a two-dimensional profilometer trace, it is assumed that the three-dimensional surface measurement is an accurate representation of the cylinder liner surface.

3.2.3 Surface Measurement Filtering

Surface measurement data, two- or three-dimensional, contains the surface roughness, waviness, and the nominal surface shape. Filtering is required to isolate the surface roughness from the raw surface topography. Waviness is removed from profile traces in this work with the use of an Rk filter. The Rk filter, as defined by DIN 4776, is designed to reduce the overshoot in the roughness profile that occurs on both sides of a deep valley. The Rk filter is preferred over the use of other filtering methods because it will generally give a better representation of roughness for cylinder liner surfaces, which generally contain deep valleys, as seen in the trace in Fig. 1.6.

3.3 Asperity Contact

Asperity contact between two rough surfaces is described using the model developed by Greenwood and Tripp [12]. An asperity is a roughness peak, or local maximum, in the surface

roughness trace; the population of asperities is different than the population of surface roughness. The Greenwood and Tripp model calculates micro-contact and pressures that arise when two rough surfaces approach and contact each other. According to the Greenwood and Tripp model, nominal asperity contact pressure between two rough surfaces is expressed as

$$P_c\left(\frac{d}{\sigma}\right) = K'E' \int_{\frac{d}{\sigma}}^{\infty} \left(z - \frac{d}{\sigma}\right)^{2.5} \phi(z)dz, \tag{3.5}$$

where

$$K' = \frac{8\sqrt{2}\pi}{15}(\eta\beta\sigma)^2\sqrt{\frac{\sigma}{\beta}}. \tag{3.6}$$

In Equations (3.5) and (3.6), P_c is the nominal asperity contact pressure between the two surfaces, d is the mean separation of the two surfaces, η is the asperity density per unit area, β is the asperity peak radius of curvature, $\phi(z)$ is the probability distribution of asperity heights, and z_s is defined as the offset between the asperity height mean and the surface height mean. The composite Young's modulus and the composite standard deviation of asperity heights used by the Greenwood and Tripp model are given by

$$E' = \frac{2}{\frac{1-\nu_1^2}{E_1} + \frac{1-\nu_2^2}{E_2}} \tag{3.7}$$

and

$$\sigma = \sqrt{\sigma_1^2 + \sigma_2^2}, \tag{3.8}$$

respectively, where E_1 and E_2, and ν_1 and ν_2 are the respective Young's modulus and Poisson's ratio of the two contacting surfaces, and σ_1 and σ_2 are the standard deviation of asperity heights of the two surfaces. The Greenwood and Tripp model assumes that contact is elastic, and the asperities are parabolic in shape and identical on the contacting surfaces.

In reality contact between the ring and cylinder liner in an engine may include some plastic deformation, especially during the initial break-in period. As a result, ring to liner contact may enter an elastic-plastic regime. However, as has been done by other researchers, it is assumed that contact between the cylinder liner and ring can be treated as elastic even though plastic deformation may be occurring [30]. Greenwood and Tripp have shown that the nominal asperity pressure calculated for elastic contact is very similar to that calculated for plastic deformation. It should be noted that the effect of oil film and oxide layers on the surfaces of the ring and liner may also play an important role in asperity contact, and have not been considered in this work.

3.3.1 Stochastic Surface Texture

The Pearson frequency curves, described in Section 3.1.2, can be combined with the Greenwood and Tripp model to describe asperity contact between the piston ring and cylinder bore surface

stochastically. Reasonable assumptions must be made for the values of asperity density and peak radius of curvature. For illustration, the effect of varying skewness on asperity contact pressure is illustrated in Fig. 3.5. In Fig. 3.5, asperity contact pressure is plotted against the mean separation of two rough surfaces being brought into contact with each other (normalized by σ) when the asperity distributions on the two surfaces are negatively skewed (Sk = -0.7). The predicted contact pressure assuming the distribution of asperity heights is Gaussian is also plotted in Fig. 3.5 for comparison. Values for asperity density, asperity radius of curvature, the standard deviation of asperity heights, and the composite Young's modulus typical of cylinder liner and piston ring finish were assumed, and are listed in Table 3.1.

Table 3.1: Typical Greenwood and Tripp parameters

Parameter	Value	Unit
$(\sigma\beta\eta)$	0.06	-
E'	1.75×10^{11}	Pa
K'	2.396×10^{-3}	-

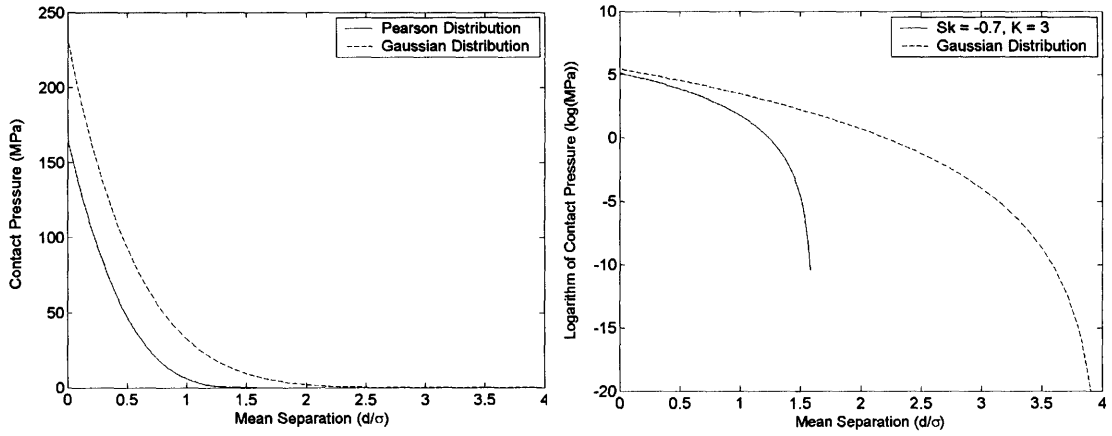

Fig. 3.5: Comparison of predicted contact pressure verses skewness

From analyzing Fig. 3.5, two differences are observed when comparing the contact behavior of two rough surfaces with negatively skewed asperity height distributions to the contact behavior assuming a Gaussian distribution of asperity heights. Firstly, initial asperity contact occurs at a smaller mean separation of surfaces when the distribution of asperity heights is negatively skewed. Secondly, once initial contact occurs, contact pressure rises more rapidly when the distribution of asperity heights is negatively skewed. This observation is better illustrated in right-hand figure of Fig. 3.5, in which the natural logarithm of the contact pressure is plotted against the mean separation of two surfaces with negatively skewed and Gaussian asperity height distributions.

Using this methodology, asperity contact pressure can be predicted between the ring and liner using only discrete statistical parameters if detailed information on the liner surface texture is not available.

3.3.2 Deterministic Surface Texture

With the availability of a profilometer trace, the rough surface parameters and asperity height probability distribution can be determined directly. This removes the need to infer the shape of the probability distribution and assume values for asperity density and radius of curvature, as is done with a stochastic description of surface texture. Thus, a method of determining the rough surface input parameters for the Greenwood and Tripp model from a two-dimensional profilometer trace is proposed. This methodology can be easily extended for use with three-dimensional surface data if available.

An asperity peak is defined as a data point from the surface roughness trace that is higher than both of its adjacent points,

$$asp(i) \equiv h(i) > \left(h(i-1), h(i+1)\right), \tag{3.9}$$

where *h(i)* is the height of the data point *i* in the profilometer trace and *asp(i)* is the height of an asperity peak. This definition of an asperity is influenced by the distance between data points in the profilometer trace. Therefore, it is important to choose a sampling rate high enough that asperity peaks can be properly identified. It is also necessary to estimate the number of asperities per unit area, or asperity summit density, from the asperity peak density per unit length obtained from a two-dimensional profilometer trace. Based on both experimental and analytical analysis, the three-dimensional density of asperity summits is related approximately to the two-dimensional density of asperity peaks [31],

$$\eta \approx 1.8\left(\frac{\#\ of\ asperities}{length}\right)^2. \tag{3.10}$$

The asperity peak radius of curvature, β, is determined using an average of the radii of the best-fit curves through each point in the trace identified as an asperity and its immediate neighbors, as is illustrated in Fig. 3.6.

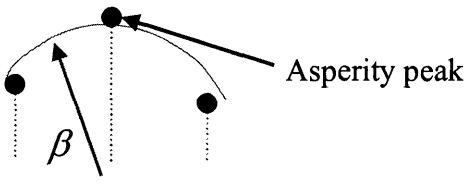

Fig. 3.6: Asperity radius definition

The Greenwood and Tripp model also requires the statistical distribution of asperity peak heights to determine asperity contact pressure. The measured surface data from a two-dimensional profilometer trace can be used to infer the shape of the asperity height distribution. The methodology behind the construction of the asperity height distribution is described below.

The population of asperities in a surface roughness trace, and the respective height of each asperity peak, is identified based on the definition given in Equation (3.9). The total range of asperity peak heights is subsequently divided into equal height subintervals. The number of subintervals used is dependent on the number of asperities present within the trace. In the present study, the number of subintervals was set equal to the square root of the total number of asperities, rounded to the nearest integer [32]. Each asperity is assigned to the appropriate subinterval based on its height, and a frequency distribution of asperity heights is computed. The frequency distribution is assumed to be a discrete representation of the actual probability distribution of asperity heights. Figure 3.7 displays the surface height and asperity height distributions calculated for a typical production cylinder liner finish. The noise present in the asperity height frequency distribution in Fig. 3.7 does not affect the calculation of asperity contact because the Greenwood and Tripp model integrates the frequency distribution when calculating asperity contact pressure.

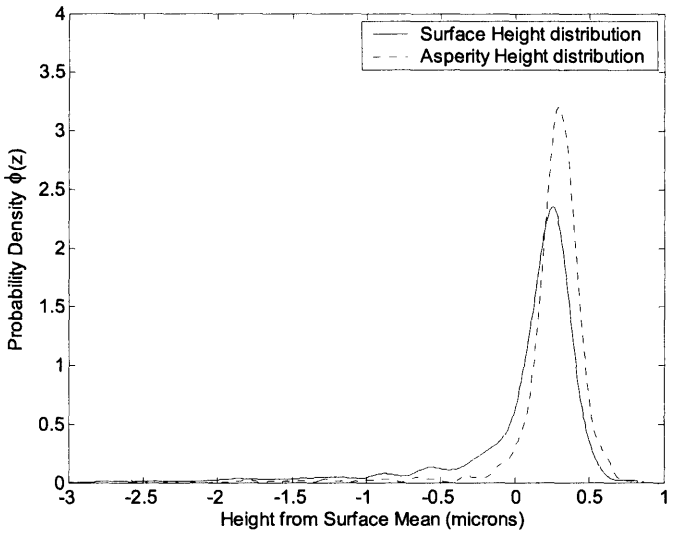

Fig. 3.7: Comparison of surface and asperity height probability density functions

Using this methodology, asperity contact behavior for a specific liner surface texture can be accurately modeled.

3.4 Oil Flow Resistance

The current ring-pack model accounts for the effect of surface roughness on oil flow using an average one-dimensional Reynolds equation developed by Patir and Cheng,

$$\frac{\partial}{\partial x}\left(\phi_p \frac{h^3}{\mu}\frac{dp}{dx}\right) = 6U\frac{\partial}{\partial x}\left(h\cdot\phi_g + R_q\cdot\phi_s\right) + 12\frac{\partial h}{\partial t}, \tag{2.2}$$

introduced in Section 1.2.2 [13]. If follows that the flow rate per unit width in the cross-flow direction can be written as

$$q_x = -\phi_p \frac{h^3}{12\mu}\frac{dP}{dx} + \frac{U}{2}\left(h\phi_g + R_q\phi_s\right), \tag{3.11}$$

where q_x is the oil volume flow rate, h is the nominal oil film thickness, U is the piston sliding speed, μ is the oil dynamic viscosity, R_q is the composite standard deviation of roughness of the two surfaces, dP/dx is the pressure gradient in the flow direction, ϕ_g is the geometric flow factor that is the ratio of the average clearance over the nominal clearance between the two surfaces, and ϕ_x and ϕ_s are the pressure and shear flow factors, respectively. The geometric flow factor has been added by the author so that the oil flow rate predicted is in terms of the nominal oil film thickness alone and does not include the average rough surface oil film thickness, as was done by Patir and Cheng [13].

In a similar manner, Patir and Cheng developed stress factors that modify the predicted shear stress acting on a rough surface in a highly viscous flow [13]. The average shear stress is given by

$$\tau_x = \frac{\mu U}{h}\left(\phi_{fg} + \phi_{fs}\right) - \phi_{fp}\frac{h}{2}\frac{dP}{dx}, \tag{3.12}$$

where τ_x is the shear stress acting on the ring surface, ϕ_f is a geometric stress factor that is the ratio of the nominal clearance over the average clearance between the two surfaces, and ϕ_{fp} and ϕ_{fs} are the pressure and shear stress factors, respectively.

The geometric and pressure flow factors and stress factors are a function of the rough surface separation only,

$$\phi_i = \phi_i(h), i = p, fp, g, fg, \tag{3.13}$$

while the shear flow and stress factors are functions of both the rough surface separation and the relative roughness of the two surfaces,

$$\phi_i = \phi_i(h, R_{q1}^2 / R_{q2}^2), i = s, fs, \tag{3.14}$$

where R_{q1} and R_{q2} are the surface roughness values for the two rough surfaces. The extra dependence of the shear flow and stress factors on the relative roughness of the two surfaces is result of the relative motion between the surfaces. Physically, the movement of a rough surface generally enables extra flow to be transported, while a static rough surface generally traps and restricts flow. Therefore, the effective shear and flow stress factors are defined by the counteracting effect between the two rough surfaces moving relative to each other,

$$\phi_i = \frac{1}{\sqrt{R_{q1}^2 + R_{q2}^2}}\left[\phi_1 \cdot R_{q1} - \phi_2 \cdot R_{q2}\right], i = s, fs, \tag{3.15}$$

where surface 1 is the moving surface and surface 2 is the static surface, and ϕ_1 and ϕ_2 are their respective flow factors. The flow factors, ϕ_1 and ϕ_2, are determined by combining each rough surface with a smooth surface to isolate the rough surface's effect on lubricant flow. For two surfaces with identical roughness and texture, there will be no additional shear flow or shear stress due to surface roughness because the effects of the two rough surfaces will effectively cancel each other out. All flow and stress factors were calculated by Patir and Cheng for artificially generated surfaces with Gaussian surface roughness. However, cylinder liner surfaces are highly non-Gaussian in nature. Deep honing grooves are also typically present in a cross-hatch pattern on the liner surface. Therefore, Patir and Cheng's results cannot be used directly for ring-pack performance analysis.

3.4.1 Stochastic Surface Texture

A stochastic description of surface roughness, with no details of surface texture, necessitates a simplified approach for the determination of oil flow resistance. As has been done in the literature, Patir and Cheng's Gaussian flow and stress factors were used in combination with a truncated surface roughness. This method uses a bearing curve truncation method to determine an equivalent Gaussian roughness that represents the core and peak regions of the non-Gaussian liner surface, and this truncated liner roughness is used in calculating the flow and stress factors [26,33]. The main assumption underlying this methodology is that the deep valleys do not play a significant role in oil flow resistance, and can therefore be neglected. Details of the truncation method are given below.

Employing the definitions of peak, core, and valley regions of surface roughness described in Section 1.3.2, an equivalent Gaussian distribution can be determined that has the same peak and core regions as the actual distribution,

$$\int_{-0.5R_k}^{-\infty} \frac{a}{\sqrt{2\pi}R_q^*} \exp\left(\frac{-z^2}{2\left(R_q^*\right)^2}\right) dz = M_{r1} \tag{3.16}$$

and

$$\int_{-0.2R_k}^{0.2R_k} \frac{a}{\sqrt{2\pi}R_q^*} \exp\left(\frac{-z^2}{2\left(R_q^*\right)^2}\right) dz = 0.4, \tag{3.17}$$

respectively, where R_q^* is the equivalent truncated Gaussian roughness and a is a truncation factor that scales the Gaussian distribution to fit the peak and core regions of the actual distribution. It should be noted that *100(1-a)* represents the percentage of the distribution in the valley region that has been truncated [26].

The Pearson system of frequency curves was used to represent the probability distribution of surface roughness for surfaces with non-Gaussian values of skewness. The relationship between the actual surface roughness and the truncated surface roughness, R_q and R_q^* respectively, is shown in Fig. 3.8. As the skewness of the surface is decreased, the truncated surface roughness

representing the peak and core regions of the distribution decreased because a greater proportion of the surface lies within the truncated valley region of the distribution.

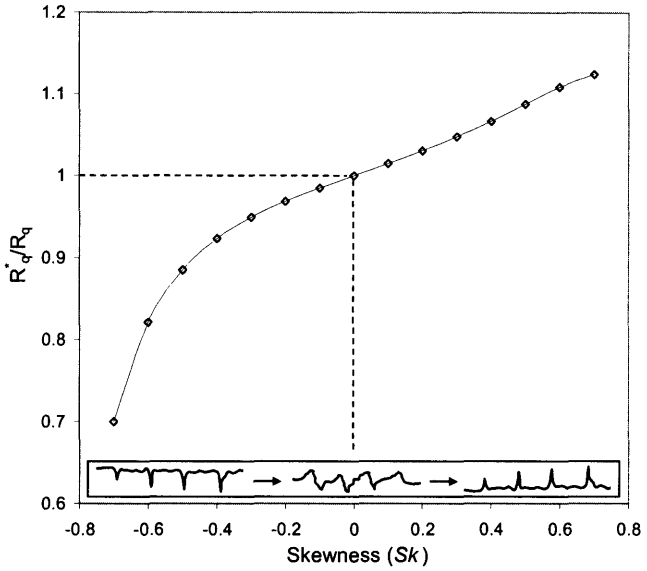

Fig. 3.8: The effect of surface skewness on equivalent truncated Gaussian roughness

Using this methodology, the effect of surface roughness on oil flow can be estimated if detailed information about the liner surface texture is not available.

3.4.2 Deterministic Surface Texture

Similar to asperity contact, a more accurate prediction of the oil flow resistance due to surface texture can be obtained if details of the surface finish are available. Unlike asperity contact, which only requires a two-dimensional description of surface roughness, a three-dimensional measurement of the liner surface texture is needed to determine oil flow resistance characteristics. A model has been developed at MIT that calculates flow factors through a flow simulation incorporating measured three-dimensional liner surfaces using a methodology similar to Patir and Cheng [13]. Details of the calculation of flow factors using the flow simulation are outlined in Section 3.6. These flow factors can be implemented into MIT's ring-pack model, and allow for the effects surface texture on oil flow resistance to be accurately modeled if a three-dimensional measurement of a surface is available.

3.5 Relationship between Surface and Asperity Height Distribution

There is an important subtlety underlying the modeling of rough surfaces. The modeling of asperity contact requires a description of asperity peak heights, while the modeling of oil flow resistance requires a description of surface heights. Recall that an asperity is a local maximum in the surface roughness trace. In a mixed lubrication regime when asperity contact and hydrodynamic pressure are coupled, an assumption must be made concerning the surface

reference height at which the fluid is assumed stagnant relative to the surface, and a no-slip condition is valid. In the following work, the mean height of each rough surface was assumed to be the appropriate reference height. Therefore, the fluid film height between the piston ring and cylinder is defined as the separation between the mean heights of the two rough surfaces.

When modeling surface roughness and asperity contact stochastically, usually only parameters on surface roughness are available. Therefore, it is necessary to make an assumption on the relationship between the statistical nature of surface heights and asperity peak heights. In analyzing typical cylinder bore finishes, a similarity between the actual asperity height and surface height probability distributions was observed. In general, the behavior of the two probability distributions was very similar when a wide variety of cylinder bore finishes were analyzed. Figure 3.9 displays the relationship between the standard deviation, skewness, and kurtosis of the surface height and asperity height distributions for a variety of SI cylinder bore finishes in new condition, and after a 15 hour dynamometer test.

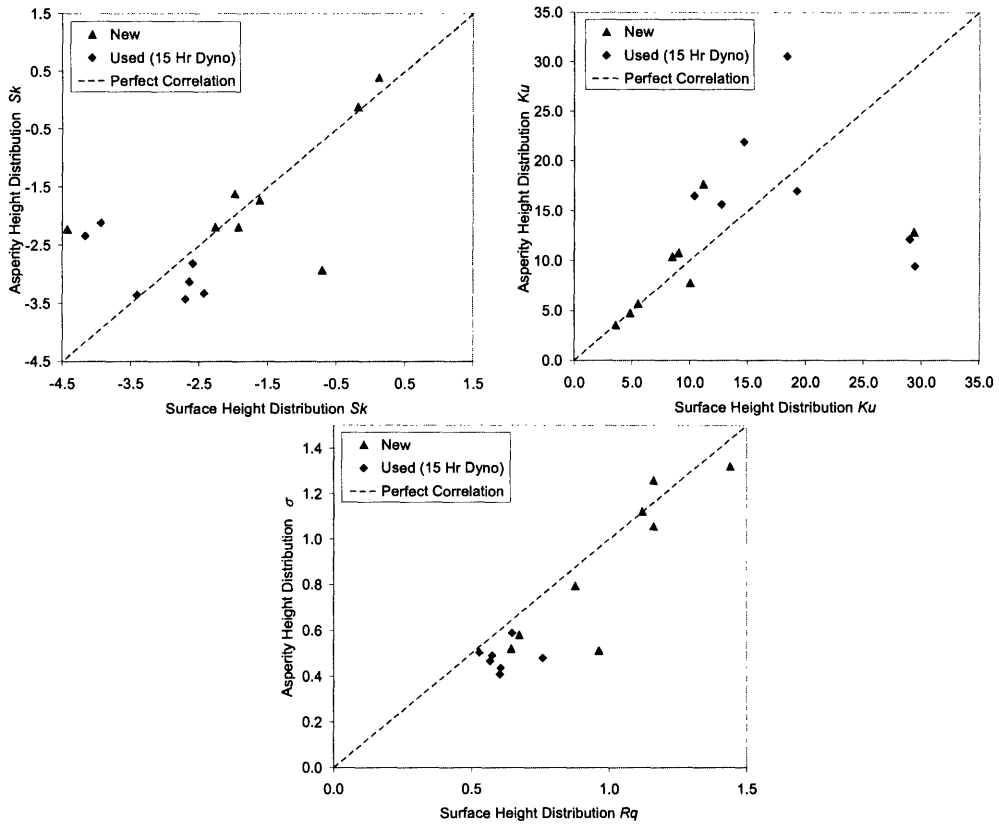

Fig. 3.9: Comparison of surface and asperity distribution parameters

From examining Fig. 3.9, there appears to be a strong correlation between the nature of the surface height distribution and the asperity height distribution in the case of typical SI cylinder bore finishes. This finding is significant in that it does not agree with the assumption made by Greenwood and Tripp, as well as other researchers, that the complete distribution of asperity heights tends towards a Gaussian distribution regardless of the shape of the underlying surface height distribution [12, 34]. Thus, it assumed in this work that the surface height and asperity height distributions are the same when no additional information is available.

3.6 Rough Surface Flow Simulation

A program was developed by Yong Li at MIT to determine the highly viscous flow solution between a smooth plate and a user-defined rough surface for a given set of boundary conditions. In this work, the program was used to calculate flow and stress factors. Since only one surface is rough, the dependence of the shear flow factor and stress factor on the relative roughness of the two surfaces, as shown in equation (3.15), is removed. The shear flow factor and stress factor calculated using the program are both equal to those for the user-defined rough surface. It is assumed that the effect of the liner surface texture dominates that of the ring surface texture; therefore, the ring can be approximated by a smooth surface in the flow simulation. This is a reasonable assumption in most cases because the ring surface is typically much smoother than the liner, with no deep characteristic grooves. A composite surface roughness, including ring roughness, is used in this work when evaluating flow and stress factors between the ring and liner, although the flow and stress factors were developed using the liner texture alone. The setup of the program is shown diagrammatically in Fig. 3.10.

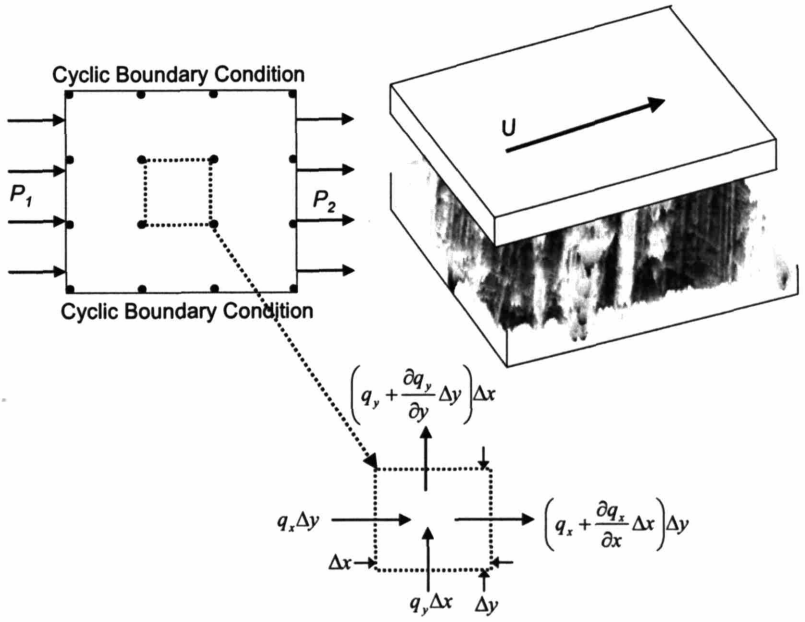

Fig. 3.10: Flow factor program setup

In Fig. 3.10, q_x and q_y are the unit flow rates in the x- and y-directions, respectively, and Δx and Δy are the element dimensions, which are determined by the spacing of the user-supplied rough surface. The cyclic boundary condition requires the surface profile at the sides of the patch perpendicular to the imposed flow direction to be identical, and the net flow through these sides to be equal. In essence, the patch is treated as a closed cylinder in the direction perpendicular to the imposed flow. To satisfy this criterion, a routine has been implemented in MIT's rough surface code that modifies the surface profile near the sides of the patch perpendicular to the imposed flow so that they are identical. The cyclic boundary condition is more correct than the no-flow boundary condition applied by Patir and Cheng because it allows unrestricted flow in both the x- and y-directions. In addition to inputting the rough surface profile, the program user must specify the pressure gradient across the patch, the relative sliding velocity between the two

surfaces, the fluid viscosity, and the separation between the mean of the rough surface and the smooth surface.

3.6.1 Patch Size

It is important to choose dimensions of the rough surface patch carefully. The patch must be large enough to include a large number of asperities. The patch must still be small compared with the total contact area between the ring and liner so that large scale effects, such as surface geometry, do not affect the results. A diagram displaying some key parameters pertinent to selecting the patch size between the ring and liner is shown in Fig. 3.11.

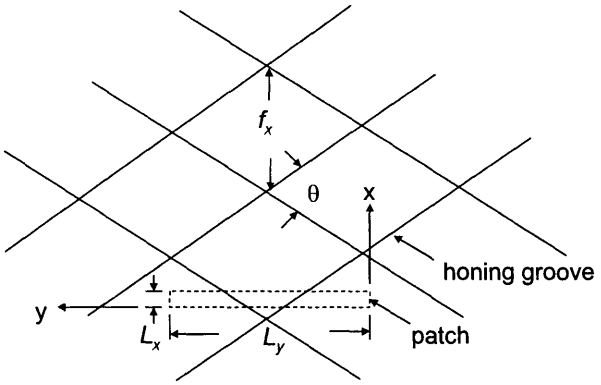

Fig. 3.11: Appropriate rough surface patch size for flow factor analysis

In Fig. 3.11, L_x and L_y are the patch lengths in the axial and circumferential directions, respectively, f_x is the axial distance between honing marks, and θ is the honing cross hatch angle.

For the ring-to-liner interaction being considered, the axial patch length was chosen as one fortieth of a typical ring width in the axial direction of the cylinder bore,

$$L_x = (n-1)\Delta x = \frac{B}{40}, \tag{3.18}$$

where n is the number of nodes in the x-direction and B is the ring axial width. This is the same nodal distance used when solving the Reynolds equation between the ring and liner within MIT's ring pack program. In the circumferential direction, it is desirable to have a patch length that is greater than the distance between honing marks,

$$L_y = (m-1)\Delta y > \frac{f_x}{\tan(\theta/2)}, \tag{3.19}$$

where m is the number of nodes in the y-direction. This ensures that a honing groove will be present within the patch. A typical patch used for the flow factor calculation is shown in Fig. 3.12.

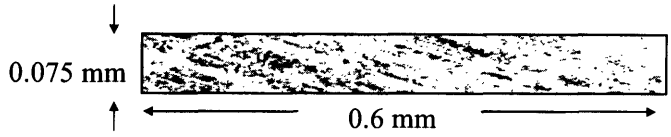

Fig. 3.12: Typical cylinder liner patch for flow factor analysis

3.6.2 Key Assumptions

Several assumptions were made in describing rough surface flow behavior. With MIT's rough surface simulation program, cavitation was neglected at the asperity level. As a result, negative hydrodynamic pressures are predicted by the model on any divergent portion of the rough surface profile. In reality, dissolved air in the lubricant may leave solution, effectively preventing the local oil pressure from dropping below the lubricant saturation pressure, which is typically similar to ambient pressure [25]. Nonetheless, this assumption was also made by Patir and Cheng in their work, and incorporation of asperity scale cavitation is outside the scope of this work [13]. It was also assumed that as rough surface contact occurs, the portion of the rough surface in interference with the smooth surface is sheared off cleanly, and has no further effect on the interaction of the two surfaces.

Hydrodynamic pressure and local oil film thicknesses are output from the MIT program in discrete form. It has been assumed that the rough surface can be interpolated linearly between the nodes, as is illustrated in Fig. 3.13.

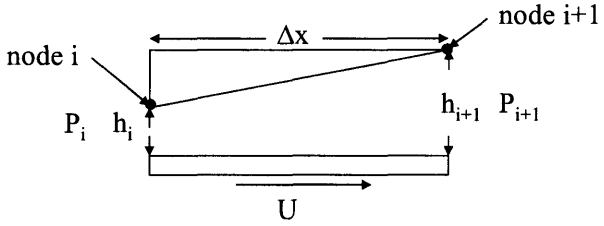

Fig. 3.13: Surface interpolation between nodes for flow factor calculation

A highly viscous flow wedge solution was applied between surface nodes, and the local flow and shear stress predictions are given by

$$q_x = -\frac{1}{12\mu}\frac{(P_{i+1}-P_i)}{\Delta x}\cdot\left[\frac{2h_i^2h_{i+1}^2}{h_i+h_{i+1}}\right]+\frac{U}{2}\cdot\left[\frac{2h_ih_{i+1}}{h_i+h_{i+1}}\right]$$
$$= -\frac{1}{12\mu}\frac{(P_{i+1}-P_i)}{\Delta x}\cdot\left[H_p^3\right]+\frac{U}{2}\cdot\left[H_s\right] \qquad (3.20)$$

and

$$\tau_x = -\frac{1}{2}\frac{(P_{i+1}-P_i)}{\Delta x}\cdot\left[\frac{2h_ih_{i+1}}{h_i+h_{i+1}}\right]+\mu U\cdot\left[\frac{\ln(h_i/h_{i+1})}{h_i-h_{i+1}}\right]$$
$$= -\frac{1}{2}\frac{(P_{i+1}-P_i)}{\Delta x}\cdot\left[H_{fp}\right]+\mu U\cdot\left[1/H_{fs}\right], \qquad (3.21)$$

respectively, where H_p and H_s are the equivalent heights used to calculate local pressure and shear driven flow between nodes i and $i+1$, respectively, and H_{fp} and H_{fs} are the equivalent heights used to calculate the corresponding local shear stress due pressure and shear flow, respectively. It should be noted that all equivalent heights are sensitive to small gap heights,

$$\lim_{h_i, h_{i+1} \to 0} H_p, H_s, H_{fp}, H_{fs} = 0. \tag{3.22}$$

As a direct extension of this property, the local shear stress prediction between nodes on the rough surface will become unbounded as either node height approaches zero provided a non-zero relative velocity is present between the two surfaces,

$$\lim_{h_i, h_{i+1} \to 0} \frac{\mu U}{H_{fs}} = \infty. \tag{3.23}$$

Physically, this represents the local onset of infinite shear stress between an asperity peak on the rough surface and the adjacent smooth surface just prior to contact. As separation decreases and approaches the molecular scale, the assumption of Newtonian shear stress behavior, which has been assumed in calculating shear stress, is no longer valid. In reality, fluids can only sustain a finite shear stress. A detailed analysis of molecular rheology is outside the scope of this study. Therefore, a limiting shear stress of 1 MPa, which the literature gives as a typical limiting shear stress for a lubricating fluid, has been assumed [35]. The minimum local separation for which Newtonian shear stress is assumed to exist is

$$H_{fs,\min} \equiv \frac{\mu U}{\tau_{\max}}, \tag{3.24}$$

where τ_{max} represents the limiting shear stress. When H_{fs} decreases below this minimum value, the local shear stress is assumed equal to the limiting shear stress.

3.6.3 Determination of Flow Factors

With the use of MIT's rough surface flow simulation program, flow and stress factors can be determined by specifying the appropriate boundary conditions, using the methodology developed by Patir and Cheng. The smooth surface solution for highly viscous flow between two surfaces is compared to the solution predicted by MIT's rough surface simulation program with the same nominal separation,

$$q_x = -\phi_p \frac{h^3}{12\mu} \frac{dP}{dx} + \frac{U}{2}\left(h\phi_g + R_q\phi_s\right) = \frac{1}{m(n-1)} \sum_{i=1}^{n-1} \sum_{j=1}^{m} \left[\frac{-H_p^3}{12\mu} \frac{(P_{i+1,j} - P_{i,j})}{\Delta x} + \frac{U}{2} H_s \right] \tag{3.25}$$

and

$$\tau_x = \frac{\mu U}{h}\left(\phi_{fg} + \phi_{fs}\right) - \phi_{fp}\frac{h}{2}\frac{dP}{dx} = \frac{1}{m(n-1)}\sum_{i=1}^{n-1}\sum_{j=1}^{m}\left[-\frac{H_{fp}}{2}\frac{(P_{i+1,j} - P_{i,j})}{\Delta x} + \frac{\mu U}{H_{fs}}\right], \quad (3.26)$$

where dP/dx represents the average hydrodynamic pressure gradient applied across the entire patch. The right-hand sides of equations (3.25) and (3.26) are the average of the local flow and shear stress predictions, respectively, from the MIT program for all of the rough surface elements. Recall that m and n are the respective number of nodes in the radial and circumferential directions of the patch.

The geometric factors, ϕ_g and ϕ_{fg}, are functions only of rough surface geometry, and are defined by

$$\phi_g = \frac{1}{h}\cdot\frac{1}{m(n-1)}\sum_{i=1}^{n-1}\sum_{j=1}^{m}H_s \quad (3.27)$$

and

$$\phi_{fg} = h\cdot\frac{1}{m(n-1)}\sum_{i=1}^{n-1}\sum_{j=1}^{m}\frac{1}{H_{fs}}, \quad (3.28)$$

respectively. Both ϕ_g and ϕ_{fg} will be equal to unity when no contact is occurring between the rough and smooth surface. The geometric factor ϕ_{fg} becomes unbounded as local rough surface contact begins to occur. Therefore, H_{fs} was set equal to the minimum height given in equation (3.28) when it H_{fs} was less than the minimum height for reasons discussed in detail in Section 3.6.2.

The pressure flow and pressure stress factors are calculated by setting the relative velocity between the surfaces equal to zero and applying a non-zero pressure gradient, thereby isolating the effects of pressure driven flow. Under these boundary conditions, equations (3.25) and (3.26) reduce to

$$\phi_p = \frac{\frac{1}{m(n-1)}\sum_{i=1}^{n-1}\sum_{j=1}^{m}H_p^3\frac{(P_{i+1,j} - P_{i,j})}{\Delta x}}{h^3\frac{dP}{dx}} \quad (3.29)$$

and

$$\phi_{fp} = \frac{\frac{1}{m(n-1)}\sum_{i=1}^{n-1}\sum_{j=1}^{m}H_{fp}\frac{(P_{i+1,j} - P_{i,j})}{\Delta x}}{h\frac{dP}{dx}}, \quad (3.30)$$

respectively, allowing determination of the pressure flow and pressure stress factors. Equations (3.29) and (3.30) represent a ratio of the rough surface oil flow rate and shear stress to the equivalent smooth surface quantities.

To calculate the shear flow and shear stress factors, the pressure gradient across the patch is set equal to zero, and a non-zero relative velocity is applied between the surfaces. Under these boundary conditions, equations (3.25) and (3.26) reduce to

$$\phi_s = \frac{\frac{1}{m(n-1)}\sum_{i=1}^{n-1}\sum_{j=1}^{m}\frac{H_p^3}{12\mu}\frac{(P_{i+1,j}-P_{i,j})}{\Delta x}}{\frac{U\cdot R_q}{2}} \tag{3.31}$$

and

$$\phi_{fs} = \frac{\frac{1}{m(n-1)}\sum_{i=1}^{n-1}\sum_{j=1}^{m}\frac{H_{fp}}{2}\frac{(P_{i+1,j}-P_{i,j})}{\Delta x}}{\frac{\mu U}{h}}, \tag{3.32}$$

respectively, allowing determination of the shear flow and shear stress factors.

It should be noted that no net pressure flow would exist for two smooth parallel surfaces subjected to a zero net applied pressure gradient. However, a net pressure driven flow and corresponding shear stress will generally exist between parallel rough and smooth surfaces with no net applied pressure gradient. This is due to the local wedge flow conditions that exist as a result of the rough surface at the asperity level, as is shown in Fig. 3.13. The shear flow factor is the ratio of the net pressure flow over the additional shear flow transport expected due to the movement of the rough surface, $U \cdot R_q/2$. Similarly, the shear stress factor is the ratio of the additional shear stress due to the net pressure flow over the smooth surface shear stress, $\mu \cdot U/h$.

In this manner, all three flow factors and all three stress factors can be determined for a user-defined rough surface profile as a function of the nominal separation between the smooth and rough surface.

4 Experimental Verification of Surface Texture Model

A new method of characterizing surface texture deterministically was presented in Section 3. Experiments were performed to determine the capability of the deterministic rough surface contact and oil flow resistance models to accurately predict ring friction. Due to difficulties involved in precisely measuring ring-pack friction in an operating engine, experimental data was obtained by the component supplier MAHLE with the use of a reciprocating bench tester. Both friction and wear measurements for different liner surfaces were obtained from the experiments. A summary of this work can be found in [36].

4.1 Reciprocating Bench Tester

A CETR UMT-2 reciprocating tester was used in this work. Normal load was applied using a closed-loop servo mechanism, and normal load and friction forces were measured with strain-gages. The experimental setup is shown in Fig. 4.1. The tests were conducted using a procedure developed by MAHLE to accelerate ring wear and facilitate its evaluation. The accelerated ring wear test is designed to simulate the extreme ring conditions of heavy duty diesel (HDD) engines.

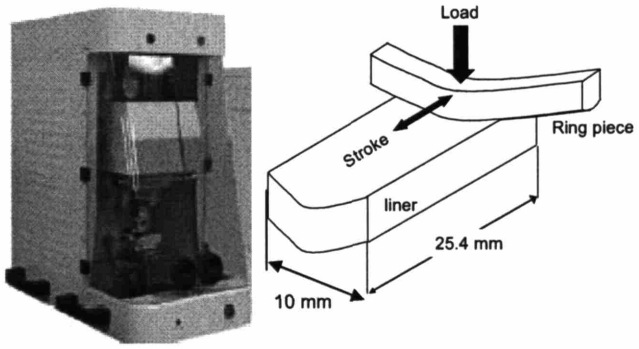

Fig. 4.1: CETR UMT-2 reciprocating tester

The test consists of a four hour test with an applied ring pressure of 120bar, a rotational speed of 900rpm, and the liner specimen flooded with 20ml of SAE 30 Texaco Regal oil. To accelerate ring wear, the oil is doped with 0.57g of 0.05 μm diameter Alumina particles and 1.9g of quartz 600 mesh per liter of oil. The testing procedure is as follows. For the first five seconds the ring and liner are broken-in by varying the applied load from 75 to 360N, at which point a constant load of 360N is maintained for the next four hours. The accelerated wear test is used to rank the wear behavior between ring coatings and liner materials and finishes, and a minimum of six replications are done for each ring/liner combination. For this work, the liner specimens were obtained from regular production Pearlitic cast iron cylinder liners from a heavy-duty diesel engine with a 130mm diameter bore. The top ring specimens were obtained from 3mm wide production gas nitride steel rings with a CrN PVD coating.

4.1.1 Modeling Reciprocating Tester

A computer model was developed to predict the friction produced by the ring specimen during the reciprocating tests. The model was based on MIT's axis-symmetric ring-pack friction model, details of which are given in Section 2.3 [10]. The model layout for a cross-section of the ring specimen is detailed in Fig. 4.2.

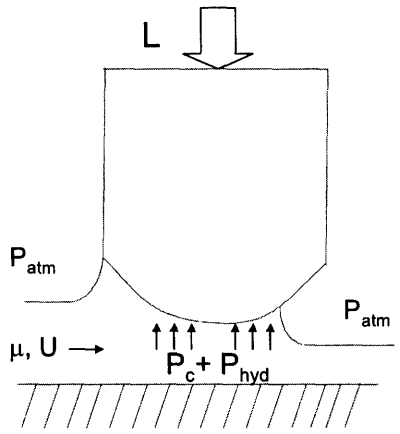

Fig. 4.2: Model layout of ring specimen in reciprocating tester

In Fig. 4.2, P is the unit pressure applied to the ring specimen, U is the instantaneous sliding velocity of the ring, μ is the lubricant dynamic viscosity, P_{atm} is atmospheric pressure, and P_c and P_{hyd} are the pressures generated by asperity contact and hydrodynamic shear, respectively. In the bench test the oil covers the entire liner specimen, so it was assumed in the analysis that there was sufficient lubricant supply to flood the inlet of the ring specimen throughout the entire stroke of the ring. The total friction force experienced by the ring specimen, F_f, is the summation of hydrodynamic and boundary contact friction, as described in Section 2.3.3. The instantaneous total coefficient of friction at time t, $a(t)$, is given by

$$a(t) \equiv \frac{F_f(t)}{L}. \tag{4.1}$$

The average coefficient of friction observed over one cycle of ring motion, a_T, is defined by

$$a_T \equiv \frac{N}{60} \int_0^{60/N} a(t)dt, \tag{4.2}$$

where N refers to the rotational speed of the crankshaft in revolutions per minute.

The operating conditions and geometric parameters of the reciprocating tester required as model inputs for this study are summarized in Table 4.1. Both the lubricant temperature and coefficient of boundary contact friction values were estimated. Note that the effects of the alumina and quartz on oil viscosity were also neglected.

Table 4.1: Operating conditions and geometric parameters

Parameter	Value	Unit
Ring Stroke	10	mm
Ring Specimen Length	10	mm
Ring Face Profile	Skewed Barrel	-
Ring Young's Modulus	350	GPa
Liner Young's Modulus	100	GPa
Lubricant	SAE 30W	-
Lubricant Temperature	25	°C
Applied Pressure, P	120	bar
Reciprocating Speed, N	900	rpm
a_{bc}	0.1	-

4.1.2 Applicability of Bench Tester Results to Engine Conditions

A significant range of lubrication conditions seen in an engine also occur during a cycle of the bench tester. Lubrication conditions ranging from primarily boundary lubrication to primarily hydrodynamic lubrication are predicted to occur despite the high ring load and low sliding speeds during the bench test. This is due to offsetting effect of high oil viscosity at the low operating temperatures of the test, and the large ring wetted area due to the flooded inlet condition. The wide range of lubrication conditions is illustrated in Fig. 4.3, in which the predicted proportions of total ring load carried by asperity contact and hydrodynamic pressure over a cycle are plotted for a slide honed surface. During ring reversal, boundary lubrication is almost reached as the majority of total ring load is supported by asperity contact. During mid-stroke conditions, pure hydrodynamic lubrication is almost attained with very little asperity contact present.

The coefficient of boundary contact friction was assumed to be similar to that found in an engine. A rough comparison can be made between the average hydrodynamic coefficient of friction predicted by the Reynolds equation,

$$f \approx \sqrt{\frac{\mu U}{PB}}, \tag{4.3}$$

during the bench test and during an engine cycle,

$$\frac{f_E^2}{f_T^2} \approx \left(\frac{\mu_E}{\mu_T}\right)\cdot\left(\frac{U_E}{U_T}\right)\cdot\left(\frac{P_T}{P_E}\right)\cdot\left(\frac{B_T}{B_E}\right). \tag{4.4}$$

In equations (4.3) and (4.4), f is the coefficient of hydrodynamic friction, U is the sliding velocity, P is the applied ring pressure, B is the ring wetted width, and the subscripts E and T refer to engine and test, respectively. Table 4.2 provides an estimate of the cycle average values of these parameters for the bench test, and for typical diesel engine operating conditions. It

should be noted that f is also the dimensionless duty parameter for the Stribeck curve that defines the lubrication regime under which the ring is operating.

Table 4.2: Estimated bench tester and diesel engine operating parameters

Parameter	Bench Tester	Diesel Engine
Liner Temperature, [°C]	25	130
μ, [Pa·s]	0.2	0.005
U, [m/s]	0.5	10
P, [bar]	120	20
B, [mm]	1.5*	0.5*

* Wetting widths based on ring width of 3mm

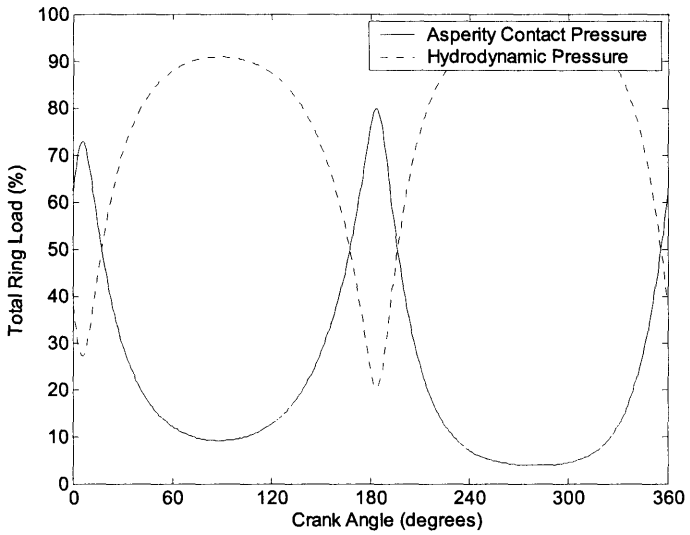

Fig. 4.3: Breakdown of total ring support in reciprocating tester

By combining the estimates given in Table 4.2 and Equation (4.4), it is seen that the average coefficient of hydrodynamic friction estimate for a diesel engine is the same order of magnitude to that of the bench tester,

$$\frac{f_E}{f_T} \approx \sqrt{\left(\frac{0.005}{0.2}\right)\cdot\left(\frac{10}{0.5}\right)\cdot\left(\frac{120}{20}\right)\cdot\left(\frac{3}{1}\right)} \approx 3. \tag{4.5}$$

Since the coefficients of boundary contact friction and hydrodynamic friction are similar for the bench tester and a diesel engine, the reciprocating tester operates in similar range of lubrication conditions, or covers a similar range on the Stribeck diagram, as a diesel engine. Therefore, the results obtained from the bench tester are not incomparable to the conditions seen by a piston ring in a diesel engine.

4.2 Experimental and Modeling Results

4.2.1 Ring and Liner Surfaces

The intention of this work was to study surface finishes that are representative of production cylinder bores. Thus, a typical plateau honed liner and a typical slide honed liner were chosen. A steel ring specimen, representative of a production top ring, was used in conjunction with both production cylinder bores. Table 4.3 summarizes the finishes of the two liner surfaces used in the experiment. Table 4.4 summarizes the input parameters predicted for the Greenwood and Tripp model for the two surfaces considered. The standard deviation of asperity heights for the piston ring was taken as 0.15 μm.

Table 4.3: Characteristics of liner surfaces considered

	Plateau Honed	**Slide Honed**
R_q [μm]	0.84	0.49
R_{pk} [μm]	0.25	0.28
R_k [μm]	0.74	0.39
R_{vk} [μm]	1.85	1.47
Sk	-2.79	-3.85
Ku	13.82	25.99
Honing angle	35° - 45°	35° - 45°

Table 4.4: Calculated Greenwood and Tripp Parameters

	Plateau Honed	**Slide Honed**
σ [μm]	0.64	0.29
β [μm]	29.2	27.6
η x10^{10} [m^{-2}]	2.10	2.50
z_s [μm]	0.01	0.06
Sk	-2.95	-5.35
Ku	17.16	52.53

4.2.2 Predicted Asperity Contact Pressure

A comparison was made between the contact pressure predicted for the slide honed and plateau honed surfaces. Fig. 4.4 shows the contact pressure predicted by the Greenwood and Tripp model for a slide honed and plateau honed surface.

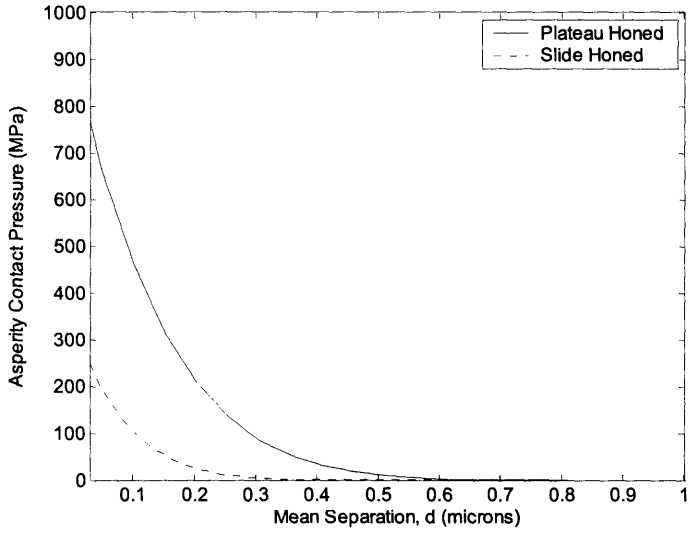

Fig. 4.4: Predicted asperity contact pressure for slide and plateau honed surfaces

By examining Fig. 4.4, it is seen that the asperity contact pressure predicted by the Greenwood and Tripp model is significantly higher for the rougher plateau honed surface. It should be stressed that it is not the shape of the probability distribution alone that is affecting predicted contact pressure. The underlying populations of asperities for the plateau and slide-honed surfaces obtained from the two-dimensional profilometer traces are different, leading to different values of asperity density, asperity peak radius of curvature, and the standard deviation of asperity heights. These values in turn affect predicted contact pressure.

4.2.3 Predicted Flow Factors

Flow factors were determined for the plateau and slide honed surfaces using the methodology described in Section 3.6. WLI measurements of the cylinder liner surfaces were used in conjunction with MIT's rough surface flow model, which is also described in Section 3.6. These flow factors account for the different effects of the two surface finishes on oil flow resistance and hydrodynamic shear stress. An average of three patches from each surface was used in determining the six flow factors required. The dimensions of these patches, 0.075 mm in the axial direction of the cylinder and 0.6 mm in circumferential direction, were chosen according the guidelines stipulated in Section 3.6.1. The average flow factor results for the plateau and slide honed surfaces, including the flow factors predicted by Patir and Cheng for a Gaussian isotropic surface for reference, are given in Fig. 4.5. Curve-fit equations for these flow factor curves were developed using regression analysis, and are given in Appendix B.

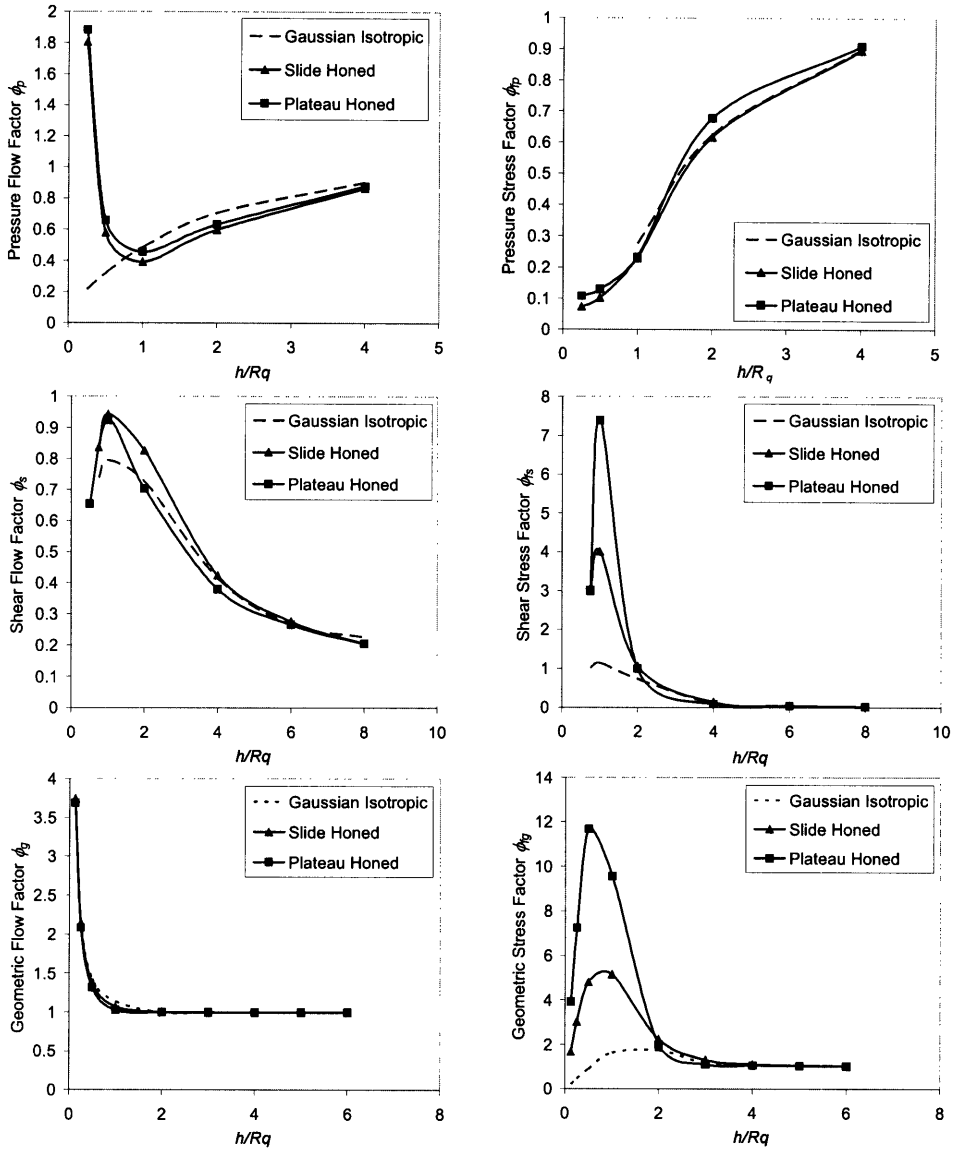

Fig. 4.5: Flow factors for slide and plateau honed surfaces

By Examining Fig. 4.5, it is seen that there are differences between the flow behavior of the shear and plateau honed surfaces. It should be noted that the flow and stress factors are normalized by the surface roughness, and are therefore independent of its value. Both surfaces also behave differently than a Gaussian isotropic surface, in large part because of the deep grooves present as a result of the honing process.

Two main differences in the flow factors arise when comparing the plateau and slide honed surfaces to the Gaussian surface. The pressure flow factor increases rapidly for both the plateau and slide honed surfaces at small nominal separations, which is a result of flow through the deep valleys. A higher peak value in the shear and geometric stress factors is reached for both the plateau and slide honed surface as compared to a Gaussian isotropic surface. This due to the large area of contact that occurs as a result of the many flat peaks characteristic of negatively skewed plateau and slide honed finishes. Large shear stresses are present near local contact areas,

causing the higher peaks in the geometric and shear stress factors as compared to a Gaussian isotropic surface.

Since the plateau and slide honed surfaces have the same honing cross-hatch angle, the differences in flow factors observed between these two finishes is a mainly a result of surface peak and valley characteristics. The slide honed surface tends to block flow more than the plateau honed surface, corresponding to the slightly lower pressure flow factor curve and slightly higher shear flow factor curve for the slide honed surface. Additionally, a higher degree of surface contact occurs for the slide honed surface, leading to slightly higher geometric and shear stress factors. These differences will in turn affect the predicted ring friction.

4.2.4 Predicted Oil Film Thickness

The reciprocating tester is not capable of measuring oil film thickness between the ring and liner specimen. Therefore, only the predicted oil film thickness is presented in this work. The predicted ring minimum oil film thickness for the slide honed and plateau honed surfaces is shown in Fig. 4.6.

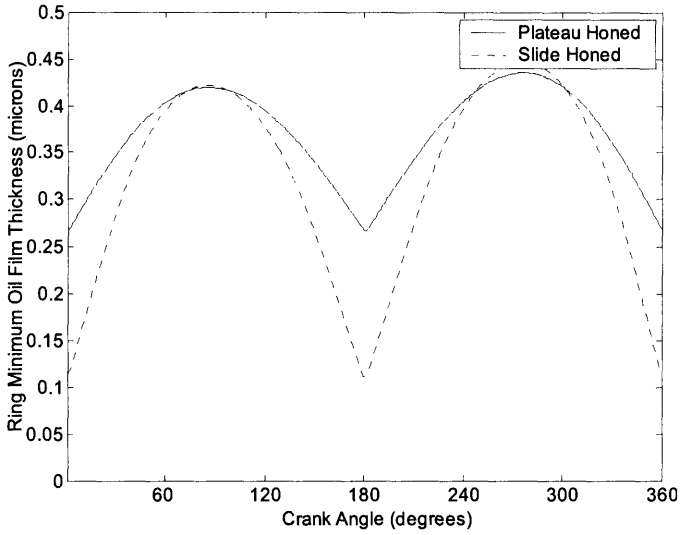

Fig. 4.6: Ring specimen minimum predicted oil film thickness

By examining Fig. 4.6, it is evident that a larger minimum oil film thickness is predicted for the plateau honed surface as a result of the higher asperity contact pressure prediction. In addition, the maximum predicted oil film thickness reached mid-stroke is similar for the plateau and slide honed surfaces when very little asperity contact is present. It should be noted that the effective ring profiles were slightly different in each experiment. This difference was a result of both manufacturing variations in the ring profile and slight installation misalignment in the apparatus. The ring misalignment caused non-symmetry in the effective ring profile for the slide honed surface experiments, which is the source of the difference in predicted maximum oil film thickness when the ring is traveling in different directions along the liner.

4.2.5 Comparison of Measured and Predicted Friction

The lubrication model results were compared with the experimental results obtained from the reciprocating tester. To minimize the influence on measured friction of both the change in the ring profile and liner finish during the test, only the first five seconds (75 cycles) were used to compare the friction measured experimentally with the friction predicted through simulation. The experimental data was obtained with an acquisition rate of 345Hz, which corresponds to one sampling point per 15 degrees of crank angle rotation at 900RPM, and proved to be too low to obtain a good representation of the instantaneous friction evolution along the stroke.

As a result, only the average friction coefficients obtained from simulation and experimentally from the reciprocating tester were compared. Three separate surface roughness traces from different locations on the liner specimen of both the slide honed and plateau honed surface were analyzed. Thus, the sensitivity of the model results to different measurements of the same surface was considered. In Fig. 4.7, the cycle average friction coefficient measured experimentally is compared with the model predicted average friction coefficient. In Fig. 4.7, error bars are included to illustrate the variation in the predicted cycle average friction coefficient using different traces of the same surface.

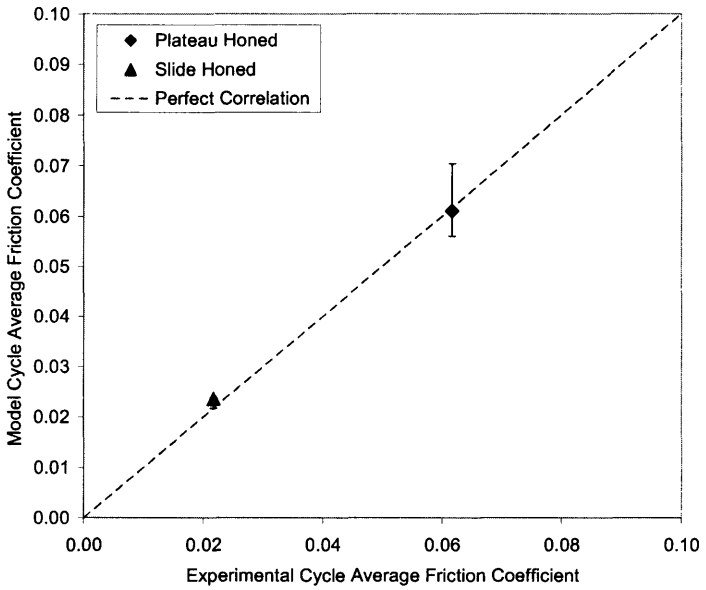

Fig. 4.7: Comparison of predicted and measured cycle average friction coefficient

Examining Fig. 4.7, it is evident the model accurately predicted the cycle average friction coefficient for the slide and plateau honed surfaces. It should also be noted that the variation in the predicted cycle average friction coefficient is significantly larger when analyzing different surface traces from the plateau honed liner. This is a result of a higher occurrence of a high peak or low valley in the plateau honed surface trace, leading to variation in calculated surface roughness parameters.

4.2.6 Comparison of Measured and Predicted Ring Wear

In addition to data on friction, the reciprocating bench tests also provided information on the wear rates experienced by both the ring and liner specimen. As the ring and liner specimens wear during the test, the measured friction will typically reduce. Figure 4.8 shows the friction variation for both the plateau and slide honed surfaces for the duration of the test.

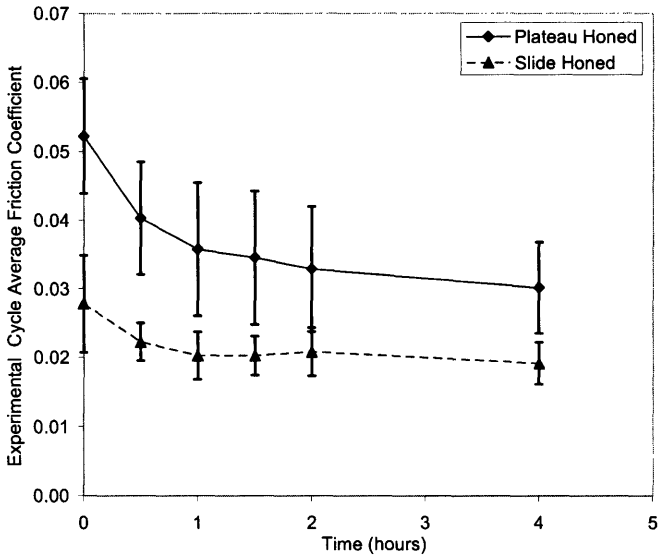

Fig. 4.8: Variation of measured friction coefficient during test

Both ring and liner wear at the conclusion of the four hour test, as measured by profile variation, was very low. This is thought to be a consequence of the PVD coating used on the ring specimens. The ring wear volume per unit length is listed in Table 4.5. Figure 4.9 shows typical ring profiles, new and after test, and the ring and liner maximum wear thickness.

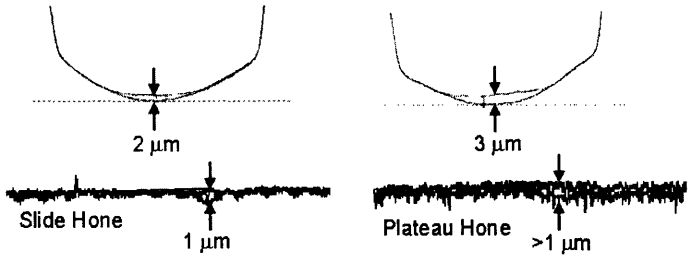

Fig. 4.9: Typical new versus worn ring/liner profiles

The difference in ring wear predicted by the simulation for the two surface finishes was estimated using the empirical model developed by Archard [37]. Archard's model predicts wear assuming

$$W = \left(\frac{K}{HV}\right) L \cdot \Delta s, \tag{4.6}$$

where W is the amount of wear, HV is the Vickers surface hardness, L is the normal load, Δs is the distance slid, and K is the wear coefficient. It is assumed that only the normal load carried by asperity contact, and not the load carried by hydrodynamic pressure, contributes to wear [38]. Since the ring and liner materials were kept constant in the current study, it was also assumed that both K and HV were the same for all experiments. The total load carried by asperity contact was used to estimate L at each point during the cycle. The total wear per cycle can be estimated by

$$W = \left(\frac{K}{HV}\right) \int_{cycle} \left(\int_{ring\ face} P_c dx \right) ds, \tag{4.7}$$

where W is the total wear per revolution. Determining predicted wear for the test requires the determination of the unknown constant K, and including the wear evolution of the ring profile in the simulation. As the ring wears its running face will generally flatten, as is seen in Fig. 4.9, leading to lower asperity contact pressures as the total ring load is carried more uniformly along the ring running face. This analysis is beyond the scope of this work, however, a rough estimate of the ratio of initial wear predicted by the model between the plateau and slide honed surfaces can be obtained. Table 4.5 shows the wear per cycle divided by (K/HV) predicted by the model for both surfaces.

Table 4.5: Measured wear and predicted initial wear

	Plateau		Slide	
	Measured	**Predicted**	**Measured**	**Predicted**
$(HV/K) \cdot W_{cycle}$ [Nm]	-	3.87	-	0.88
Wear Volume [μm^2]	30	-	9	-

The ratio of observed ring wear volume for the plateau and slide honed surfaces, and the ratio of the initial wear predicted by the model for the two surfaces given by

$$\frac{W_{T,PH}}{W_{T,SH}} = 3.33 \tag{4.8}$$

and

$$\left(\frac{K/HV}{K/HV}\right)\frac{W_{P,PH}}{W_{P,SH}} = \frac{W_{P,PH}}{W_{P,SH}} = 4.4, \tag{4.9}$$

respectively, where the subscripts T and P refer to test and predicted, respectively, and PH and SH refer to the plateau and slide honed surfaces. By comparing the two equations, it can be seen that the both the model predictions and experimental results associate higher wear with the plateau honed surface. The ratio of initial wear predicted by the model for the two surfaces is slightly higher than the ratio of ring wear observed during the experiment. This result is expected since the difference in initial wear rate will generally be higher than the difference in average wear rate throughout the test.

The instantaneous wear rate along the cycle divided by (*K/HV*) predicted by equation (4.7) is given in Fig. 4.10 for both the slide and plateau honed surfaces. It is interesting to note that the wear rate predicted for the plateau honed surface is more uniform throughout the stroke than the wear rate for the slide honed surface. This is a result of higher asperity contact for the plateau honed surface during mid-stroke conditions. This observation suggests that the plateau honed liner will exhibit more uniform wear along the swept surface, although this behavior was not considered during the experiments.

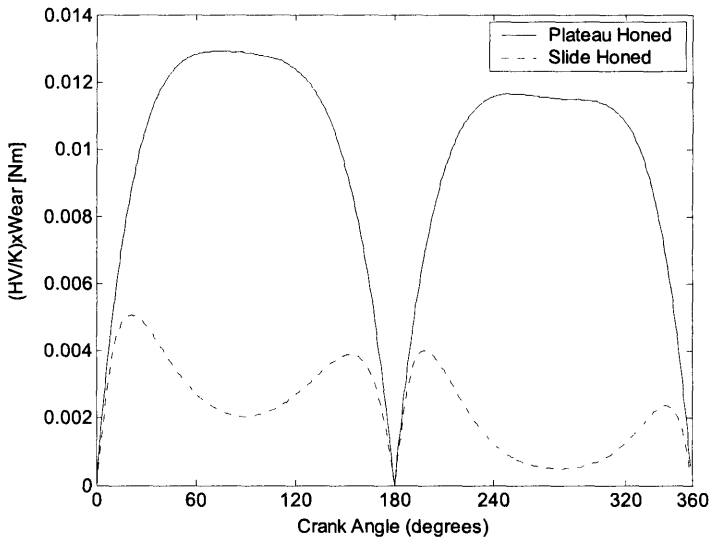

Fig. 4.10: Instantaneous wear rate for plateau and slide honed surfaces

4.3 General Conclusions

Experimental validation was performed for the deterministic method of surface characterization described in Section 3 in terms of both friction and wear. The MAHLE accelerated ring wear bench test procedure was used to measure the relative time evolution of friction and the relative wear behavior of the plateau and slide honed surfaces. These experimental results were compared with model predictions.

Higher friction was observed for the plateau honed surface throughout the four hour test, and the plateau honed surface appeared to settle to a higher steady-state level of friction. Both the ring and liner wear measured at the end of the test were higher for the plateau honed surface, and preliminary wear estimations from the model simulation predicts higher wear for the plateau honed surface.

The deterministic method of surface roughness characterization is capable of accurately predicting both the absolute average friction for the plateau and slide honed surfaces, as well as the relative difference in cycle average friction between the two surfaces. However, the deterministic method proved to be sensitive to outlying peaks and deep valleys in the surface roughness trace.

5 Low Friction Liner Finish Design

5.1 Engine Description

The improved surface characterization and modeling presented in Section 3 was used to analyze possible friction reduction strategies in the piston ring-pack. Although the general concepts can be applied to any piston ring-pack system, the following analysis was performed on a Waukesha stationary natural gas engine, shown in Fig. 5.1. Details of the engine geometry and operating conditions considered are given in Table 5.1.

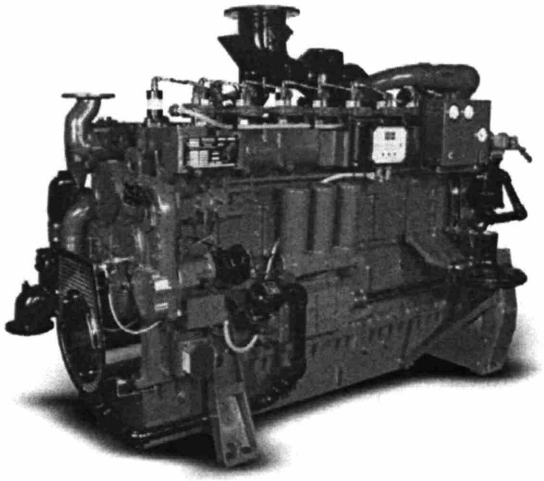

Fig. 5.1: Waukesha natural gas engine

Table 5.1: Description of engine and engine operating conditions

Parameter	Value	Unit
Manufacturer	Waukesha	-
Engine type	Natural gas, SI	-
Bore x Stroke	0.152 x 0.165	m x m
Number of cylinders	6	-
Displacement	18	L
Engine Speed	1800	RPM
BMEP @ 1800 RPM	1379	kPa
Lubricant	SAE 40W	-
Top Ring Type	Skewed barrel	-
Second Ring Type	Napier	-
OCR Type	Twin land	-

Piston ring-pack friction reduction strategies through cylinder liner finish optimization were analyzed with the goal of improving the engine's brake thermal efficiency.

5.2 Optimization of Surface Profile for Low Friction

5.2.1 The Importance of Skewness on Ring-pack Performance

There have been several experimental investigations conducted on the effects of plateau honing on friction and wear in the ring-pack [20,21]. Experimental results have suggested that a plateau-honed liner, which has a roughness profile that is negatively skewed, exhibits lower friction and wear compared to a conventionally honed liner that has an approximately Gaussian roughness profile with zero skewness. In Fig. 5.2 the profile of a negatively skewed surface is contrasted qualitatively against a surface with a Gaussian profile, with both surfaces having the same surface roughness.

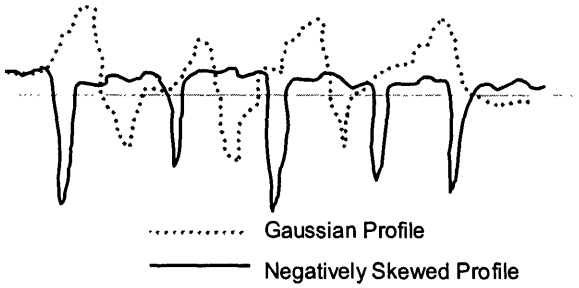

Fig. 5.2: Comparison of Gaussian and negatively roughness profiles

Although decreasing surface skewness has been identified experimentally for its friction reduction potential, its effect on piston ring friction and oil film thickness has not been considered extensively in an analytical fashion.

5.2.2 Modeling Surface Roughness and Skewness

The piston ring-pack and film thickness model described in Section 2.3 was used in conjunction with the stochastic surface model presented in Section 3 to study the effect of negative skewness and roughness on ring-pack friction and oil film thickness. The effects of surface skewness on both asperity contact and oil flow resistance were modeling using the Pearson system of frequency curves, as described in Section 3.1.2.

In the following analysis, a Waukesha stationary natural gas powered spark ignition engine was considered. Details of the engine, and the operating conditions considered are described in Table 5.1. Maintaining all other parameters constant, the skewness and standard deviation of the surface roughness were varied. Ranges of these variables were chosen to cover a practical range allowed by the Pearson system of frequency curves. Skewness values ranging from –0.8 to 0.8 and standard deviations of 0.25 and 0.5 μm were considered. The skewness and standard deviation of asperity heights were assumed to be equal to the skewness and RMS roughness of the surface, respectively. The validity of the assumption is discussed in Section 3.5. A coefficient of friction for boundary lubrication of 0.1 was assumed.

The Gaussian roughness flow factor truncation method discussed in Section 3.4.1 was used to approximate the effect of surface skewness on oil flow resistance. However, the accuracy of this truncation method becomes questionable at small oil film thicknesses, less than approximately two times the surface roughness. The top and second rings experience oil film thicknesses much greater than two times the surface roughness for the majority of an engine's cycle. However, the oil film thickness predicted between the two thin rails of the oil control ring are typically less than this amount during the complete engine cycle. Therefore, the oil control ring was excluded from the following analysis because reliable friction predictions are not possible for the OCR using the above methodology. A summary of this work can be found in [18].

5.2.3 Source of Friction Reduction

As a direct result of the underlying assumptions in this work, any reduction in friction realized through implementing non-Gaussian surface roughness will be in the mixed lubrication regime. During boundary lubrication the total ring load is carried solely by asperity contact. Since the coefficient of friction during boundary lubrication was assumed to be constant, friction is constant during boundary lubrication regardless of the nature of surface roughness. During hydrodynamic lubrication no asperity contact occurs, and the effect of flow and stress factors on ring-pack friction is small.

Reducing the skewness of the surface finish typically reduces friction. The source of the friction reduction predicted by the model is rooted in the tradeoff between the ring load carried by the asperities and the ring load carried by hydrodynamic pressure during mixed lubrication. As the skewness of surface roughness is decreased, initial asperity contact will not occur until a smaller separation of the ring and liner mean surfaces has been reached, as is demonstrated qualitatively in Fig. 5.3.

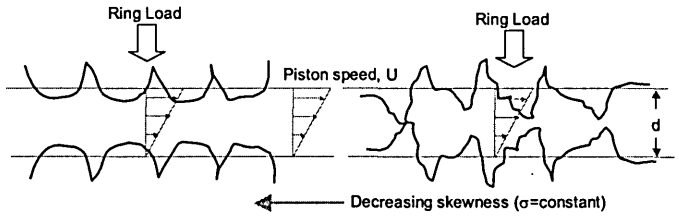

Fig. 5.3: The effect of skewness on initial asperity contact

Therefore, a greater proportion of the ring load per cycle will be supported by hydrodynamic pressure as the skewness of surface roughness is decreased. As a direct result, ring-pack friction will be reduced. The source of this friction reduction is illustrated for a single ring during typical mixed lubrication conditions in an approximate fashion. Neglecting the hydrodynamic friction contribution due to pressure gradient in equation (2.6), which is typically small, the instantaneous hydrodynamic friction prediction becomes

$$F_{f,hyd} \approx \int_{ring\ wetted\ area} \frac{\mu U}{h} dA, \tag{5.1}$$

where $F_{f,hyd}$ is hydrodynamic friction, μ is the dynamic viscosity, b is the ring axial width, U is the piston velocity, and the integration is carried out over the wetted area of the ring. It follows that

$$a_{hyd} \approx \sqrt{\frac{\mu U}{P_{hyd} b}} \approx \sqrt{\frac{10^{-2} \cdot 10}{10^{6} \cdot 10^{-3}}} \approx 0.01,$$
$$\frac{a_{bc}}{a_{hyd}} \approx 10. \tag{5.2}$$

In equation (5.2), P_{hyd} is the average hydrodynamic pressure, a_{bc} is the coefficient of friction during boundary lubrication, and a_{hyd} is the apparent coefficient of hydrodynamic friction. An order-of-magnitude analysis demonstrates that during a mixed lubrication regime, the apparent coefficient of hydrodynamic friction is typically an order of magnitude smaller than the coefficient of friction during boundary lubrication. Therefore, shifting load from the asperities to the hydrodynamic pressure developed in the lubricant will result in an overall friction reduction.

This result is illustrated in Fig. 5.4, which displays a crank-angle-to-crank-angle comparison of the instantaneous friction shift of a negatively skewed surface (Sk = -0.6, σ= 0.5 μm) relative to a Gaussian surface with the same RMS roughness. This comparison was done during the onset of mixed lubrication on the first half of the power stroke in the Waukesha engine. The surface with negatively skewed surface roughness exhibits a decrease in total friction, the sum of boundary and hydrodynamic friction, at each crank angle during mixed lubrication as a result of a load shift from the asperities to hydrodynamic pressure.

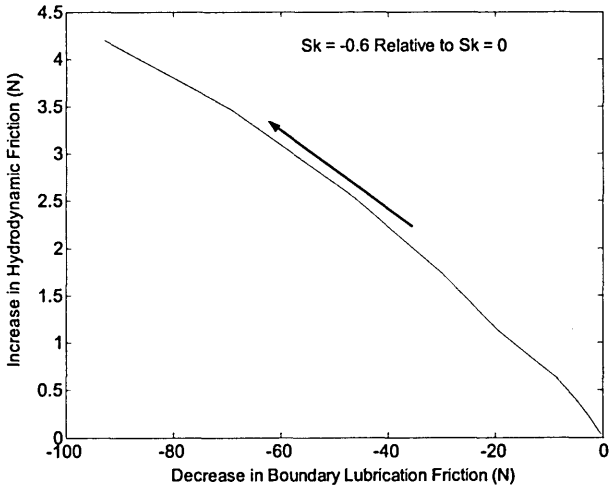

Fig. 5.4: Asperity contact and hydrodynamic pressure trade-off (σ = 0.5 μm)

In addition, based on the assumptions made in the current analysis, reducing the skewness of the liner surface will, in general, also reduce predicted hydrodynamic friction. It was demonstrated in Section 3.4.1 that decreasing the skewness of the surface roughness distribution decreases the effective truncated Gaussian surface roughness used to determine the resistance to oil flow. This decrease in effective surface roughness decreases the predicted hydrodynamic friction in the current model.

5.2.4 Predicted Friction Reduction

The hydrodynamic and boundary lubrication FMEP for the top and second rings are shown in Fig. 5.5. The change in boundary lubrication friction with respect to skewness was typically opposite to the change in hydrodynamic friction. In general, a decrease in the skewness of the surface roughness distribution reduced boundary lubrication friction, but increased hydrodynamic friction. However, the rate of decrease of boundary lubrication friction was larger than the rate of increase in hydrodynamic friction. As a result, when the two sources of friction were summed, a net friction reduction was realized.

Total FMEP for the top and second ring are illustrated in Fig. 5.6 for two different surface roughness values. Reducing the skewness and the standard deviation of the surface roughness distribution both reduced friction.

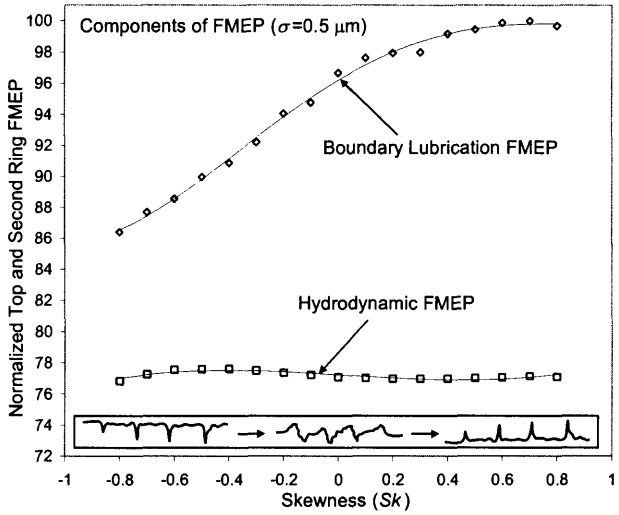

Fig. 5.5: Components of top and second ring FMEP verses skewness

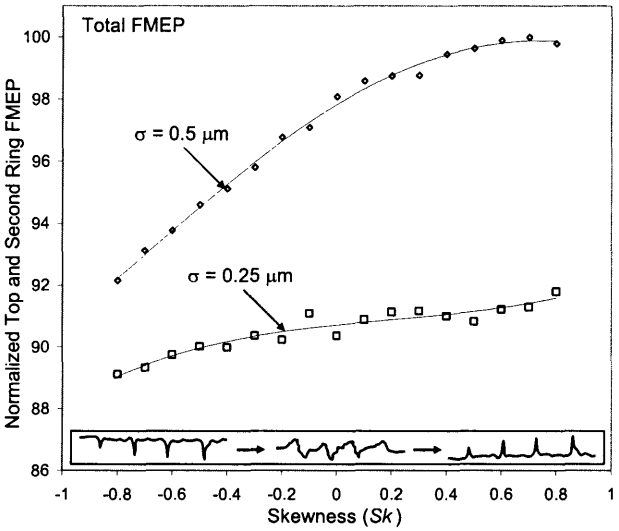

Fig. 5.6: Total top and second ring FMEP verses skewness

5.2.5 Predicted Minimum Ring Clearance and Valley Depth

Modifying the skewness of the surface roughness distribution affects the predicted minimum ring-to-liner clearance for each of the rings during mixed and boundary lubrication. Ring clearance is defined as the distance between the mean surfaces of the ring and the liner. As the skewness of the surface roughness was decreased, initial asperity contact did not occur until a smaller mean separation of the two contacting surfaces. Therefore, predicted minimum ring clearance was expected to decrease as the skewness of the surface decreased. This trend is illustrated for the Waukesha engine in Fig. 5.7. In Fig. 5.7, the minimum clearance observed by the top and second ring over one engine cycle is plotted against the surface skewness.

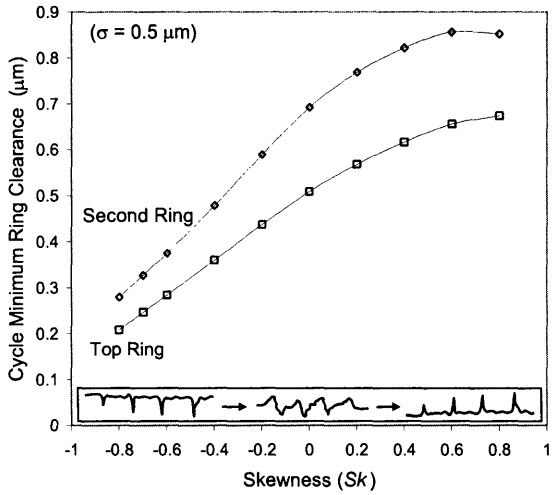

Fig. 5.7: Top and second ring cycle minimum clearance verses skewness

Decreasing skewness decreased the predicted minimum ring clearance during mixed and boundary lubrication. However, the volume in the valleys below the surface mean increased. This trend is illustrated in Fig. 5.8, in which the average valley depth below the surface mean, d_v, normalized by the surface standard deviation of roughness is plotted verses skewness.

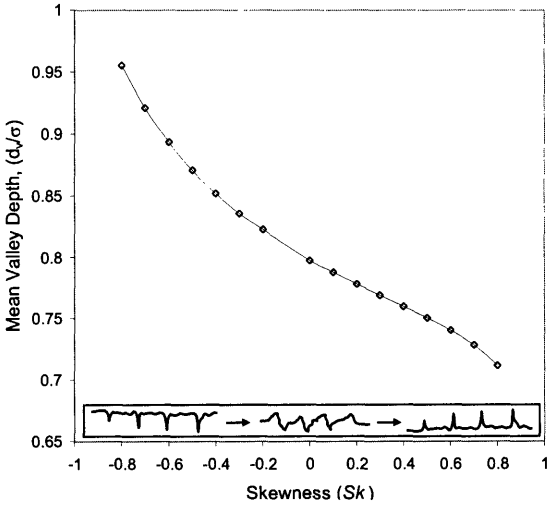

Fig. 5.8: The effect of skewness on average valley depth verses skewness

The increase in valley volume may increase oil supply through the valleys of the surface, helping to offset the decreased oil film thickness that is a result of decreased ring clearance.

5.2.6 Predicted Real Area of Contact and Scuffing Tendency

As the skewness of the surface roughness distribution is modified, the real area of contact required to support a given load will change. As the skewness of the surface roughness distribution is decreased, the real area of contact required to carry a fixed load will increase. This can be explained by examining the probability density function for a negatively skewed distribution in Fig. 3.2. For a negatively skewed distribution, the highest asperities are very close in height to each other relative to a less negatively skewed distribution. Therefore, a given load will be distributed over more asperities as skewness is decreased. The load carried by each asperity will decrease and the total real area of contact of the asperities in the aggregate will increase. This trend is illustrated in Fig. 5.9, in which the maximum real area of contact observed by the top ring over an engine cycle is plotted verses the skewness of the surface roughness distribution.

Since the coefficient of boundary lubrication friction was assumed constant in this study, the real area of contact does not influence predicted ring-pack friction. However, the real area of contact may be an important factor in determining the sensitivity of a cylinder liner to scuffing. A plateau honed surface with a negatively skewed surface roughness distribution will experience a greater area of asperity contact for given conditions, which may increase the probability of liner scuffing under extreme conditions. In this respect, the model results agree with experimental studies that have found plateau-honed liners to be more prone to scuffing [21].

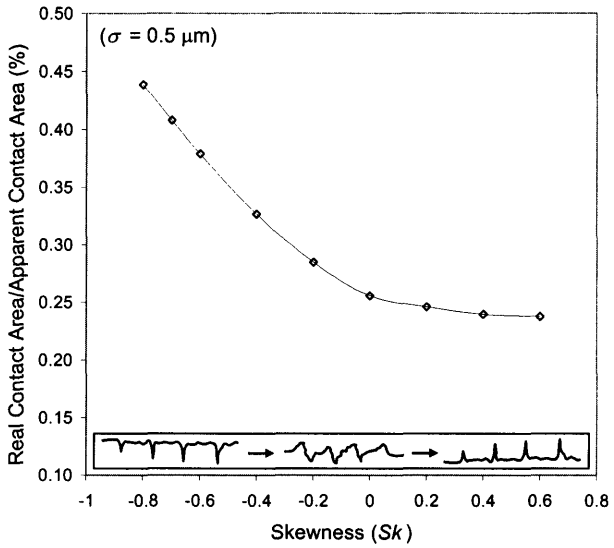

Fig. 5.9: Top ring cycle maximum real area of contact verse skewness

5.2.7 Strategy for Minimizing Friction

Decreasing the skewness and roughness of the surface finish decreases predicted top and second ring friction. Decreasing skewness delays the onset of asperity contact, increasing the proportion of ring load per cycle supported by hydrodynamic pressure. This reduces friction because the effective coefficient of hydrodynamic friction is typically an order of magnitude smaller than the coefficient of boundary friction during a mixed lubrication regime. Reducing the standard deviation of roughness also reduces friction for much the same reason.

Although the oil control ring was excluded from the following parametric analysis due to accuracy issues with the flow factor truncation method, refer to Section 5.2.2, the general findings for the top two rings are also applicable to the oil control ring.

Reducing the skewness and roughness of the surface has other potentially troublesome effects on ring-pack performance. Decreasing the skewness tends to decrease oil film thickness and increase the maximum real area of asperity contact. This may increase the chances of scuffing failure during extreme running conditions [21]. Therefore, the smoothest and most plateau surface possible while not comprising the durability of the engine is recommended to reduce ring-pack friction.

5.3 Optimization of Honing Cross-hatch Angle for Low Friction

5.3.1 The importance of Honing Grooves on Ring-pack Performance

The cylinder liner surface texture created by honing is anisotropic, with deep visible scratches left by the honing process as shown in Fig. 5.10. The angle between honing grooves perpendicular to the cylinder axis is termed the cross-hatch angle. The honing grooves contain valleys with depths that are greater than the surface roughness, as can be seen by examining Fig. 1.6. The prominence of the honing grooves suggests that they play an important role in the effect of surface texture on ring-pack performance. However, this effect is not well understood.

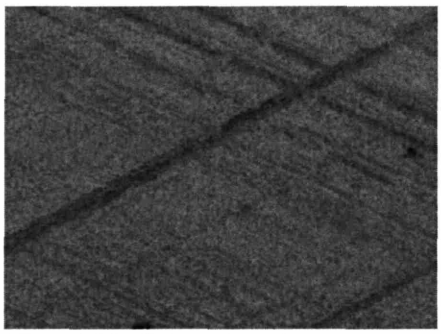

Fig. 5.10: Liner honing grooves

Resolving the effects of the honing grooves requires analysis of a three-dimensional surface, and is the focus of this Section. Three-dimensional surface flow analysis is accomplished using MIT's flow simulation program, described in Section 3.6. The flow and stress factors developed using the results from this program allow for the inclusion of the three-dimensional effects of

honing grooves into MIT's axis-symmetric ring-pack model in an average sense. The inclusion of these flow and stress factors allow the three-dimensional flow effects of honing grooves on ring-pack performance to be analyzed. Therefore, it is important to understand the effects of flow and stress factors on ring friction in order to interpret the effects of honing grooves, and surface anisotropy in general, on ring friction.

5.3.2 The Effect of Flow Factors on Friction

The effect of shear stress factors on predicted ring-pack friction is easily understood because the factors directly modify predicted hydrodynamic shear stress, as is shown in equation (3.12). However, the effect of flow factors on predicted ring-pack friction is less obvious since they do not affect predicted hydrodynamic shear stress directly. Within the ring-pack, flow factors affect the amount of hydrodynamic pressure generated, which has a direct impact on total ring-pack friction. This effect is seen mostly during mixed lubrication, when an interaction exists between asperity contact pressure and hydrodynamic pressure generation. A diagram displaying the typical layout of a ring cross-section used in MIT's ring-pack program is shown in Fig. 5.11.

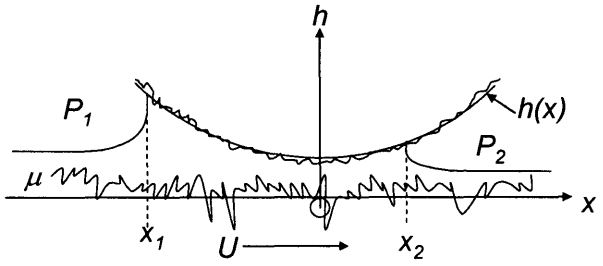

Fig. 5.11: Ring cross-section

In Fig. 5.11, x_1 and x_2 refer to fluid attachment and detachment locations on the ring face, respectively, P_1 and P_2 are the gas pressure on either side of the ring, and *h(x)* is the ring face profile.

By examining the unit flow rate between the ring and liner given by equation (3.11), which is re-written below, the pressure flow factor can be thought of as viscosity modifier, and the shear and geometric flow factors can be thought of as ring face profile modifiers.

$$q_x = -\phi_p \frac{h^3}{12\mu}\frac{dP}{dx} + \frac{U}{2}\left(h\phi_g + R_q\phi_s\right). \tag{3.11}$$

Thus, an equivalent smooth surface viscosity and smooth surface ring face profile for shear driven flow can be defined that incorporate the effects of surface roughness. These quantities are given by

$$\mu^* \equiv \frac{\mu}{\phi_x} \tag{5.3}$$

and

$$h^* \equiv h \cdot \phi_g + R_q \cdot \phi_s. \tag{5.4}$$

To illustrate the effect of these equivalent quantities on hydrodynamic pressure, and subsequently ring-pack friction, equations (5.3) and (5.4) have been incorporated into the hydrodynamic pressure prediction during typical piston ring mid-stroke conditions,

$$F_{hyd} = 6U \int_{x_1}^{x_2} \int_{x_1}^{x'} \frac{\mu^*}{h^3} \left[h^*(x) - h^*(x_2) \right] dx' dx + P_1(x_2 - x_1). \tag{5.5}$$

It has been assumed in deriving equation (5.5) that the ring is under steady-state conditions with Reynolds exit condition valid, which is typically true for a large portion of the stroke. It should be noted that flow factors have small effects at surface separations larger than four times the surface roughness, and a smooth surface solution is appropriate. Therefore, the effect of flow factors will in general be significant only at separations smaller than four times the surface roughness, where mixed lubrication exists between the ring and liner. Under these conditions, an increase in hydrodynamic load carrying capacity will typically reduce total ring friction by decreasing the load carried by asperity contact. This phenomenon is discussed in detail in Section 5.2.3.

By examining equation (5.5), it can be seen that an increase in equivalent viscosity will increase the load carrying capacity of the ring. This corresponds to a decrease in the pressure flow factor, which can be interpreted as an increase in flow restriction or blockage. The effect of the shear flow factor is somewhat more complex. Referring to equation (3.15), since the liner is stationary, an increase in the liner shear flow factor will decrease the effective shear flow factor. Examining equation (5.4), it is observed that a decrease in shear flow factor decreases the effective oil film thickness between the ring and liner, which increases the local shear stress and subsequently the hydrodynamic pressure. Therefore, a decrease in ring-pack friction will be realized by increasing the liner shear flow factor thereby increasing the hydrodynamic load-carrying capability of the ring. In a physical sense, this corresponds to increasing the amount of oil trapped and retained in the liner roughness.

5.3.3 Modeling Honing Grooves

To isolate the effect of honing cross-hatch angle on ring-pack friction, a program developed by Volvo was employed to generate three-dimensional rough surfaces with different cross-hatch angles. The program constructs a simulated surface using a methodology that mimics the honing process. The honing process is described in Section 1.3.1. The surface profile created by a multiple stage honing process with successively finer grit honing stones is simulated by the surface generator with overlapping Gaussian roughness distributions. The user must specify the equivalent plateau and valley Gaussian roughness according to the definition given by ISO 1365-3, which is briefly introduced in Section 1.3.2. The honing cross-hatch angles are determined in the actual honing process by the way in which the honing stone spirals down the cylinder liner, which itself is determined by the feed and speed rates of the honing tool. Different honing angles are produced in the simulation by transcribing the simulated surface profile at different angles

relative to the cylinder axis. Thus, varying the honing angle in this work corresponds approximately to using the same set of honing stones, and changing the feed-to-speed ratio of the honing tool. In this manner, surfaces representative of actual cylinder liner finishes were simulated.

For the following study, a typical production plateau finish was used as the underlying surface finish. Surfaces with three different honing angles were simulated, and are shown in Fig. 5.12.

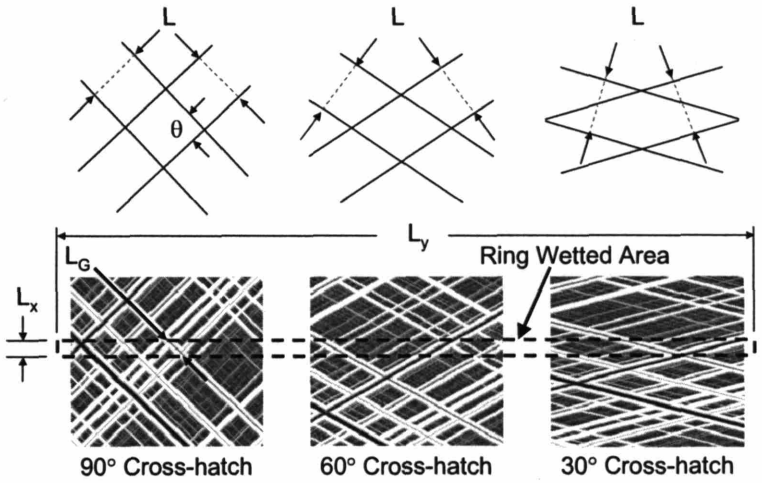

Fig. 5.12: Varying cross-hatch angle

In Fig. 5.12, θ is the honing cross-hatch angle, L_x is the radial width and L_y is the circumferential width of the ring wetted area, respectively, L_G is the groove length necessary to penetrate the radial width of the ring wetted area, and L is the characteristic distance between honing grooves perpendicular to the sliding direction of the honing stick, which is held constant when varying honing angle on the simulated surfaces. Details of the parameters of the surface are given in Table 5.2.

Table 5.2: Generated Surface Parameters for honing angle study

Parameter	Value	Unit
Circumferential patch width, L_y	2	mm
Radial patch width, L_x	0.075	mm
R_q	0.5	μm
R_{pk}	0.1	μm
R_{vk}	1.0	μm
R_k	0.6	μm
Cross-hatch angle	30, 60, 90	Degrees

The radial and circumferential patch widths used in the flow simulation were determined using the criterion given in Section 3.6.1.

The effect of varying honing angle on asperity contact pressure generation can be understood by examining the required parameters for the Greenwood and Tripp asperity contact model. The Greenwood and Tripp model is described in Section 3.3. Only the spatial Greenwood and Tripp

parameters, asperity density η and asperity peak radius β, are affected by varying honing cross angle. The spatially-independent surface profile parameters were held constant for the simulated surfaces as cross-hatch angle was varied, and are listed in Table 5.2. Recall that all surfaces were simulated assuming that they were produced by the same set of honing stones advanced at different feed-to-speed ratios to produce different honing angles. The characteristic distance between honing grooves, L, stays constant irrespective of honing angle. Therefore, the change in the spatial characteristics of the surface texture can be analyzed by defining characteristic lengths in the radial and circumferential directions of the liner, Δx and Δy respectively, that maintain the characteristic length between honing marks constant. These characteristic lengths are given by

$$\Delta x = \frac{L}{\cos(\theta/2)} \text{ and } \Delta y = \frac{L}{\sin(\theta/2)}, 0 < \theta < \pi/2. \tag{5.6}$$

The density and radii of asperities on the generated surface are directly dependent on the radial and circumferential characteristic lengths. Using equation (5.6), the dependence of asperity density and radius of curvature on honing angle can be determined.

$$\eta \propto \frac{1}{\Delta x \cdot \Delta y} \propto \sin\theta \tag{5.7}$$

and

$$\beta \propto \sqrt{(\Delta x)^2 + (\Delta y)^2} \propto \frac{1}{\sin\theta}. \tag{5.8}$$

Substituting equations (5.7) and (5.8) back into the Greenwood and Tripp model, the dependence of asperity contact pressure on honing cross-hatch angle is resolved,

$$P_c \propto \eta^2 \beta^{3/2} \propto \sqrt{\sin\theta}. \tag{5.9}$$

Thus, asperity contact pressure increases slightly as a function of honing cross-hatch angle for a given mean separation of the ring and liner. In addition to this effect, differences in observed ring-pack performance between the surfaces with different cross-hatch angles can be attributed to differences in lubricant flow behavior, which is expressed analytically through a difference in flow and stress factors.

5.3.4 Shear and Stress Factors

Shear and stress factors were calculated for simulated surfaces with different cross-hatch angles using the three-dimensional flow simulation program described in Section 3.6. Two surfaces for each honing angle were analyzed to quantify the effect of random variability on the flow factor results. Insignificantly small variation was observed in flow and stress factors for replications of statistically identical surfaces. All six flow and stress factors for the simulated surfaces with 30°, 60°, and 90° cross-hatch angles, as well as for a Gaussian isotropic surface, are shown in Fig. 5.13. Curve-fit equations for these flow factor curves were developed using regression analysis, and are given in Appendix B.

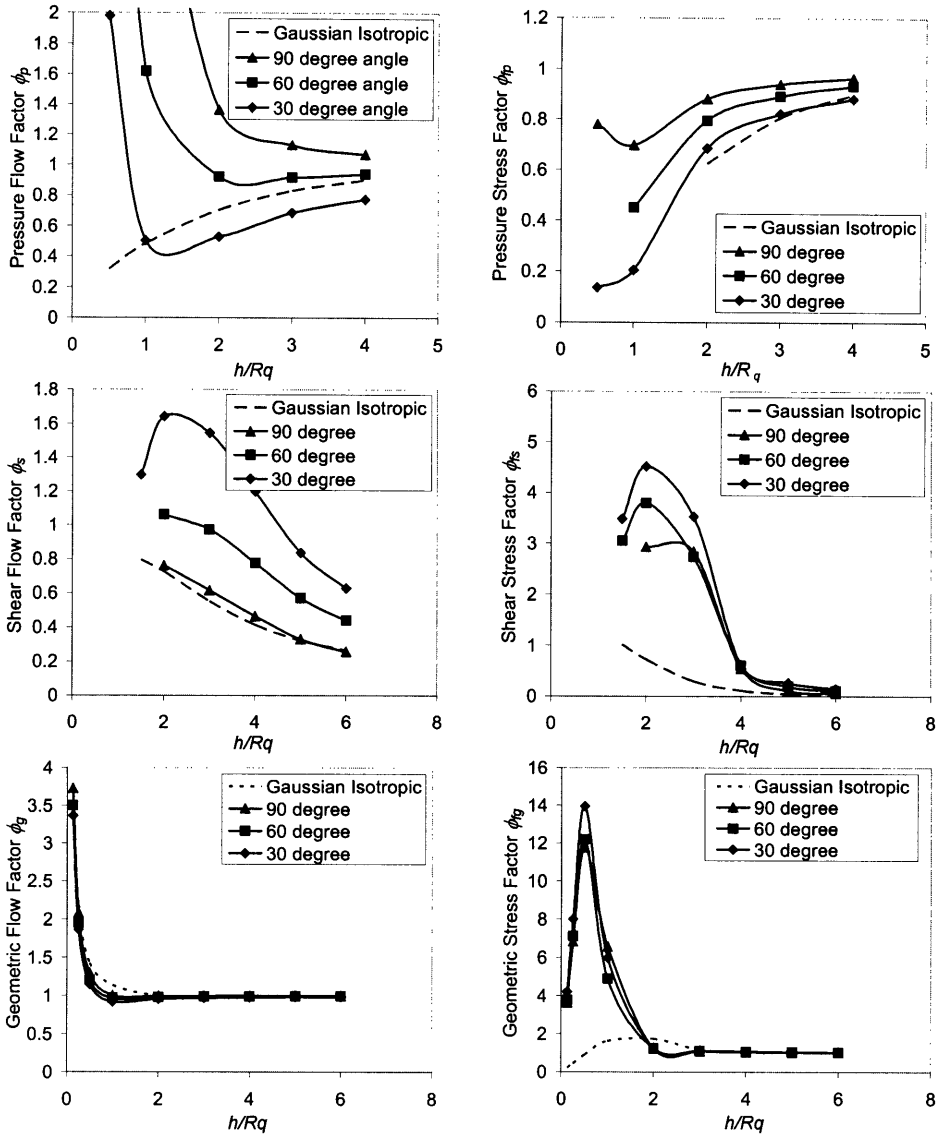

Fig. 5.13: Flow and stress factors verses honing angle

Examining Fig. 5.13, several observations can be made. The geometric flow factor and stress factor were very similar for all surfaces. This is a result of maintaining statistically identical surface height distributions for all three surfaces generated, as is shown in Table 5.2. However, varying honing cross-hatch angle affects pressure and flow shear and stress factors.

The difference in pressure flow factor and shear flow factor as a function honing cross-hatch angle suggests that flow blockage increases as the honing cross-hatch angle is decreased. This phenomenon can be understood by considering the relative density and length of the deep honing grooves within the ring wetted area for surfaces with different honing cross-hatch angles, as is shown in Fig. 5.12. As the cross-hatch angle of the surface decreases, the length of the honing groove required to penetrate the radial width of the ring wetted area, L_G in Fig. 5.12, increases and the density of honing grooves present decreases,

$$L_G \propto \cos(\theta/2)$$
$$\eta_G \propto \eta \propto \sin(\theta), \tag{5.10}$$

where η_G is the density of honing grooves.

Since the deep honing grooves provide a pathway for flow, particularly at small film thickness, both increasing the length of a honing groove and decreasing the density of grooves will effectively block both pressure-driven flow and reduce shear-driven flow carried by the ring. Thus, the main effect of decreasing honing cross-hatch angle was an increase in the hydrodynamic pressure generated between the ring and liner. Pressure-driven flow blockage changes the effective lubricant viscosity and shear-driven flow changes the effective ring profile, as was explained in Section 5.3.2.

5.3.5 Predicted Friction Reduction

The effect of varying liner surface honing angle on the Waukesha engine detailed in Section 5.1 was investigated. The effect of varying honing cross-hatch angle on pressure-driven flow dominated all other effects, including the slight difference in generated asperity contact pressure. Thus, the main consequence of decreasing the honing angle was to increase the effective viscosity of the lubrication, especially during mixed lubrication. The end result was a delay in the onset of mixed lubrication. This decreased the amount of asperity contact that occurred during the engine cycle, which in turn decreased the net ring-pack friction for reasons detailed in Section 5.2.3. The effect of decreasing honing cross-hatch angle on total ring-pack normalized FMEP is shown in Fig. 5.14.

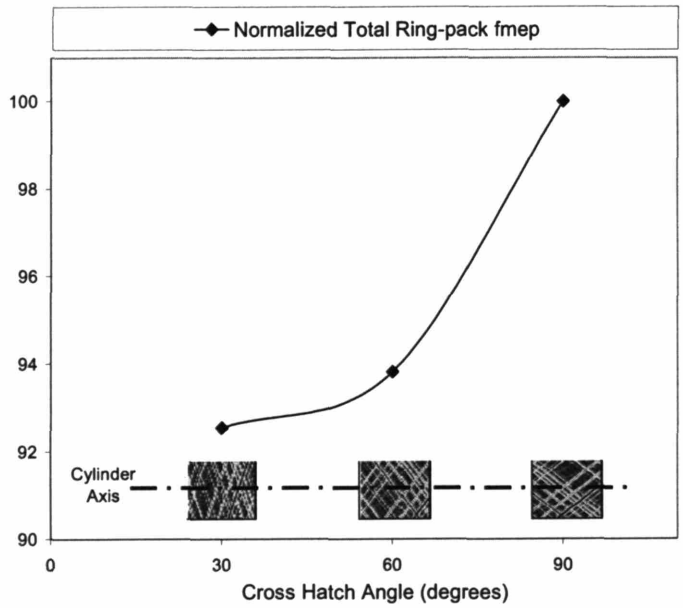

Fig. 5.14: Total Ring-pack FMEP verses honing angle

By examining Fig. 5.14, it can be seen that decreasing honing cross-hatch angle was more effective in reducing predicted ring-pack friction at larger angles. Reducing the honing cross-hatch angle from 90 to 30 degrees decreased total ring-pack FMEP by approximately 6%.

5.3.6 Predicted Minimum Ring Clearance and Scuffing Tendency

Modifying the honing cross-hatch angle also had an effect on predicted ring-to-liner clearance. The dominant effect of modifying the honing cross-hatch angle was to increase the oil effective viscosity through blockage of pressure-driven flow. The top ring minimum clearance during the cycle for the three different honing angles is shown in Fig. 5.15. As a side-note, the predicted top ring minimum clearance is higher during parts of the power and exhaust stroke, when high gas pressure is present, than during the intake and compression stroke. This unusual behavior is due to the onset of second ring radial collapse during the first part of the expansion stroke, which allows the oil film left by the oil control ring to be passed directly to the top ring.

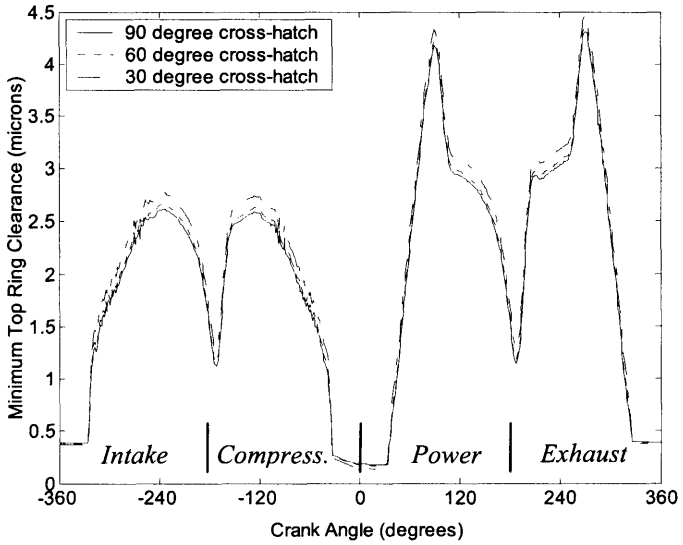

Fig. 5.15: Top ring minimum clearance verses honing angle

Examining Fig. 5.15, it can be seen that as honing angle is decreased, the predicted top ring clearance increased at all points in the cycle except during boundary lubrication near the ring reversal point, where predicted clearance decreased slightly. The increase in clearance during the majority of the stroke was a result of an increase in effective viscosity and hydrodynamic pressure generation due to the increased blockage of pressure-driven flow. The decrease in clearance during boundary lubrication, when the ring wetted width is zero and no hydrodynamic pressure is present, was a result of the slightly lower predicted asperity contact pressure for a given mean separation. This result is also displayed in Fig. 5.16, in which the cycle average and minimum top ring clearances are plotted as a function of honing cross-hatch angle.

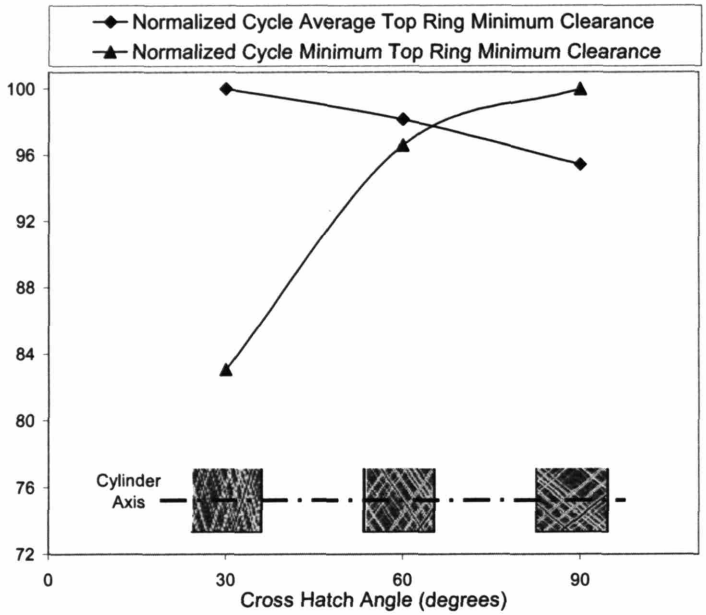

Fig. 5.16: Cycle average and minimum top ring clearance verses honing angle

Top ring clearance during mixed lubrication, and therefore oil film thickness, is increased as the honing cross-hatch angle is decreased. This could lead to an increase in oil consumption because more lubricant is present for transport to the crown land and into the combustion chamber.

The decrease in minimum ring clearance seen in Fig. 5.16 occurs in a boundary lubrication regime just past TDC of the expansion stroke, and corresponds to an increase in the maximum real area of contact between the ring and liner. Therefore, decreasing the honing cross-hatch angle slightly increases the maximum real area of contact, which has been shown experimentally to increase the chances of scuffing failure [21].

5.3.7 Strategy for Minimizing Friction

Decreasing the honing cross-hatch angle decreased predicted ring-pack friction. The decrease in friction is mainly a result of increased pressure-driven flow blockage, which increased the lubricant's effective viscosity as ring clearance decreased. This increase in effective viscosity delayed the onset of mixed lubrication, and led to a friction reduction by decreasing boundary friction.

However, decreasing honing cross-hatch angle increased the predicted oil film thickness throughout most of the stroke, which could lead to an increase in the amount of oil transported to, and consumed in the combustion chamber. In addition, decreasing honing cross-hatch angle slightly increased the predicted maximum real area of contact, which may increase the chances of scuffing failure [21]. Therefore, decreasing honing angle as much as possible without leading to unacceptable oil consumption or durability problems is recommended for minimum ring-pack friction.

5.4 Predicted Optimal Surface Texture for Waukesha Engine

The optimal liner texture will minimize ring-pack friction while avoiding unacceptable compromises in other aspects of ring-pack performance, namely oil consumption and durability. With reference to the aspects of surface finish and texture analyzed in this work, a surface finish is desired that is as smooth and plateau as possible with as low a honing cross-hatch angle as possible without introducing unacceptable side effects. However, it is very difficult to determine analytically the onset of scuffing and the exact effect of surface texture on oil consumption. For a given engine it is not possible using MIT's current modeling capabilities to determine exactly how smooth or plateau a surface, or how low a honing cross-hatch angle is allowable before oil consumption becomes unacceptable or scuffing occurs.

Nonetheless, combining the results from this Section allow for a quantitative estimation of the friction reduction possible, and an educated guess on the corresponding increase in oil consumption and scuffing, if the current liner finish in the Waukesha engine is substituted for a surface that is modified for lower friction. Details of the current Waukesha liner finish and the proposed optimal surface are given in Table 5.3, and are shown in Fig. 5.17.

Table 5.3: Current and proposed surface finish for the Waukesha Engine

Parameter	Current (New)	Proposed	Unit
R_q	0.5	0.5	μm
R_{pk}	0.15	0.1	μm
R_{vk}	0.97	1.37	μm
R_k	0.67	0.35	μm
Sk	-2.28	-3.15	-
Cross-hatch angle	45 ± 5	25	Degrees

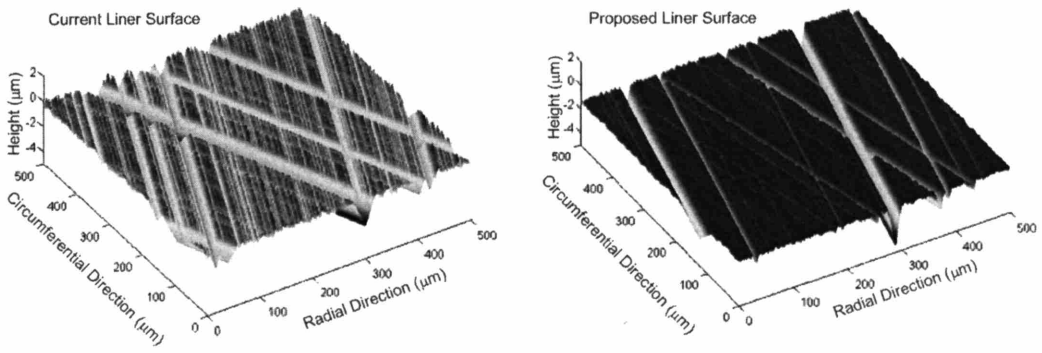

Fig. 5.17: Current and proposed Waukesha surface finish

Examining Table 5.3, it can be seen that the current Waukesha liner is already relative smooth, plateau, and contains a relative low honing cross-hatch angle. In other terms, according the conclusions presented in this chapter, the current liner is already fairly well optimized for low friction. The proposed liner finish has the same surface roughness as the current finish, and lower liner skewness and honing cross-hatch angle. It should be stressed that the results in this work demonstrate that reducing liner roughness has the strongest effect on reducing ring-pack friction

of all parameters considered. Therefore, ring-pack roughness should also be reduced if possible. The proposed surface demonstrates the additional friction reduction possible by optimizing a surface for a given roughness.

The three-dimensional surface generator was used to simulate a surface that is representative of the current Waukesha engine surface finish and the proposed lower friction surface. The surface information available for the current Waukesha liner does not include spatial roughness characteristics. Therefore, best engineering judgment was used to simulate a surface finish for both the current and proposed surface that has reasonable spatial characteristics, such as asperity density, asperity radii of curvature, and honing groove depth to width ratio. The difference in predicted ring-pack friction between the current and proposed surface finish in the Waukesha engine is given in Table 5.4. The difference in the cycle average oil film thickness and the difference in maximum real area of contact experienced by the top ring during an engine cycle are included to give a rough estimate of the potential side effects of the surface optimization.

Table 5.4: Current and proposed surface finish for the Waukesha Engine

Parameter	Conventional	Proposed
Normalized Total Ring-pack FMEP	100	94.9
Normalized Cycle Average Top Ring Oil Film Thickness	100	99.2
Real Area of Contact	-	Increased

Examining Table 5.4, it can be seen that the optimal surface finish promises an approximately 5% reduction in ring-pack friction as compared to the conventional surface finish. Predicted average oil film thickness decreases slightly with the proposed surface because the decrease in surface skewness decreases oil film thickness, and dominates the increase in oil film thickness caused by increasing the honing cross-hatch angle. However, the difference was very small. There is an increase in predicted maximum real area of contact, which may suggest an increased scuffing tendency.

The relatively small reduction in predicted friction suggests that the current Waukesha liner finish is already well optimized for low friction if surface roughness is left unchanged. Friction reduction through surface finish optimization for a given surface roughness is predicted to be substantially higher, on the order of 10%, for engines currently employing liner surfaces that are less optimized for low friction than the current finish in the Waukesha engine.

6 Effects of Ring Groove Friction on Ring-pack Performance

6.1 Introduction

The effect of friction in the ring groove on piston ring-pack friction and oil film thickness was investigated. The potential sources of groove friction were analyzed using an order-of-magnitude analysis, and subsequently, using the MIT ring pack dynamic models described in Section 2.3. Implementation of groove friction into the equation governing ring radial motion, a quasi-steady radial force balance, is shown schematically in Fig. 6.1 and analytically in equation (2.1b), which is the ring radial force balance presented in Section 2.3 modified to include groove friction.

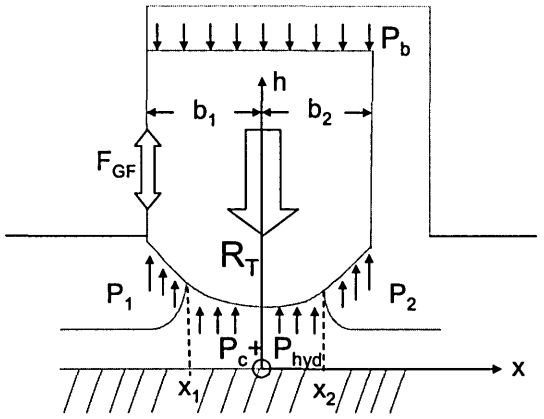

Fig. 6.1: Schematic of radial force balance including groove friction

$$\sum F_{radial} \approx 0$$

$$\int_{x_1}^{x_2} P_{hyd}\,dx + P_1(b_1 + x_1) + P_2(b_2 - x_2) - (R_T + P_b)\cdot(b_1 + b_2) + W_c + F_{GF} \approx 0, \tag{2.1b}$$

where

$$W_c \equiv \int_{-b_1}^{b_2} P_c\,dx \tag{6.1}$$

and

$$F_{GF} = \pm F_{GFA} \pm F_{GFP} \pm F_{GFV}. \tag{6.2}$$

In equations (2.1b) and (6.1), P_c is asperity contact pressure, P_{hyd} is hydrodynamic pressure generated between the running face of the ring and the cylinder liner, P_1 and P_2 are the pressures on either side of the ring running surface, P_b is the pressure behind the ring, R_T is the ring tension, W_c is the running face asperity contact force, and F_{GF} is the radial groove friction force. Equation (6.2) describes the total groove friction force, which is potentially due to three sources:

1. Asperity contact friction, F_{GFA},
2. Hydrodynamic friction due to a non-symmetric pressure profile, F_{GFP}, and
3. Hydrodynamic friction due to ring radial motion, F_{GFV}.

Each of these sources is defined in detail below.

6.1.1 Groove Asperity Contact Friction

Groove asperity contact friction was assumed to be proportional to the asperity contact normal load between the groove face on the piston and the side of the ring. Therefore, groove asperity friction was determined by multiplying the normal asperity contact force by a coefficient of boundary contact friction,

$$F_{FGA} \equiv \pm a_b \left(N_{lower\ groove} + N_{upper\ groove} \right), \tag{6.3}$$

where a_b is the coefficient of friction in the groove, and $N_{lower\ groove}$ and $N_{upper\ groove}$ are the integrated asperity contact forces on the upper and lower groove surfaces, respectively. It should be noted that the ring will only contact one side of the groove at any instant. The direction of F_{FGA} is always opposite the instantaneous direction of radial motion of the ring, since boundary contact friction is a non-conservative force.

6.1.2 Groove Hydrodynamic Friction

Hydrodynamic friction may be generated if there is some lubricant in the gap between the groove and the side of the ring. Under this condition, oil flow between the ring and the groove may be developed by a non-symmetrical pressure gradient or relative motion between the ring and groove in the radial direction of the cylinder, causing hydrodynamic friction. The groove friction per unit ring length in the circumferential direction due to a non-symmetrical pressure gradient and relative motion between the ring and the groove are

$$F_{GFP} = \int \frac{h}{2} \left(\frac{dP}{dx} \right) dx \tag{6.4}$$

and

$$F_{GFV} = -\mu \frac{dh}{dt} \int_{wetted\ area} \frac{dx}{h}, \tag{6.5}$$

respectively, where h is the local oil film thickness, μ is the oil dynamic viscosity, dP/dx is the local fluid pressure gradient, and dh/dt is the ring radial velocity relative to the piston. The integration is carried out over the wetted area of the ring.

6.2 Dimensional Analysis

An order-of-magnitude analysis was performed to place bounds on the importance of groove friction on ring-pack performance. The relative importance of groove friction due to asperity contact and due to hydrodynamic shear was compared, and the effect of groove friction on ring load was analyzed in detail.

6.2.1 Groove Asperity Contact Friction

Ring axial loading is due to a combination of gas pressure acting on the side of the ring, F_{GA}, and ring inertia in the axial direction, I_R. These forces, per unit length in the circumferential direction, are approximated by

$$F_{GA} = P_b r \tag{6.6}$$

and

$$I_R \approx m_R a_{R,avg} \approx (\rho r b) \cdot \left(\frac{4 S_p^2}{B} \right), \tag{6.7}$$

where P_b is the gas pressure acting on the side of the ring, r is the ring radial width, m_R is the mass of the ring per unit circumferential length, $a_{R,avg}$ is the ring average acceleration, ρ is the ring density, S_P is the average piston velocity, and B is the cylinder bore. Assuming that asperity contact supports the entire ring axial load, the groove friction force due to boundary contact per unit length in the circumferential direction is given by

$$F_{GFA} = a_b \left(P_b r \pm \frac{4 \rho r b S_P^2}{B} \right), \tag{6.8}$$

where a_b is the coefficient of boundary contact friction. The left term in the brackets represents the axial load on the ring due to gas pressure, and the right term in the brackets represents axial load due to ring inertia. A comparison can be made between the axial load on the ring due to gas pressure and inertia,

$$\frac{F_{GA}}{I_R} = \frac{P_b}{\frac{4 \rho b S_P^2}{B}} = \frac{B P_b}{4 \rho b S_P^2}. \tag{6.9}$$

Typical values for the various parameters related to engine geometry and operation conditions, and a typical range of pressures observed in an engine, are given in Table 6.1.

Table 6.1: Typical engine parameters

Parameter	Typical Value	Unit
Engine speed, N	50	rev/s
Cylinder bore, B	0.1	m
Ring tension, T	$900B$	N
Average piston velocity, S_p	10	m/s
Ring density, ρ	7000	kg/m^3
Ring radial width, b	0.002	m
Ring axial width, r	$2b$	m
Ring back pressure, P_b	1→100	bar
Lubricant dynamic viscosity, μ	0.01	Pa·s
Coefficient of friction, a_b	0.1	-

Substituting the typical engine geometric and operating parameters given in Table 6.1 into equation (6.9), the relative importance of axial force due to gas pressure and due to ring inertia on groove friction becomes

$$0.2 \leq \frac{F_{GA}}{I_R} \leq 200. \tag{6.10}$$

Under these conditions, the axial force due to gas pressure is much larger than the axial force due to ring inertia during the majority of the piston's stroke. Thus, the effect of ring inertia on ring axial loading has been neglected to simplify the analysis. The groove friction force due to asperity contact per unit length in the circumferential direction is given by

$$F_{GFA} = a_b P_b r. \tag{6.11}$$

6.2.2 Groove Hydrodynamic Friction

By examining equations (6.4) and (6.5), the groove hydrodynamic friction forces due to a non-symmetrical pressure gradient and due to relative motion between the ring and groove can be approximated by

$$F_{GFP} = \frac{h}{2}\left(\frac{\Delta P}{r}\right)r = \frac{h}{2}\Delta P \tag{6.12}$$

and

$$F_{GFV} = \frac{\mu r}{h}\cdot\left(\frac{dh}{dt}\right) = \frac{\mu r}{h}\cdot\left(\frac{h}{1/N}\right) = \mu N r, \tag{6.13}$$

respectively, where h is the local oil film thickness, ΔP is the average fluid pressure gradient, μ is the oil dynamic viscosity, and N is the engine speed in revolutions per second. The characteristic time is assumed to be that for one engine revolution.

6.2.3 A Comparison of Groove Friction Contributors

Using the estimations of hydrodynamic groove friction given in equations (6.12) and (6.13), the relative significance of the components of hydrodynamic friction to boundary contact friction in the groove can be estimated, and are given by

$$\frac{F_{GFP}}{F_{GFA}} = \frac{1}{2a_b}\left(\frac{h}{r}\right)\left(\frac{\Delta P}{P_b}\right) \tag{6.14}$$

and

$$\frac{F_{GFV}}{F_{GFA}} = \frac{\mu N}{a_b P_b}. \tag{6.15}$$

Based on the operating characteristics of a piston ring pack, equation (6.14) can be simplified using the following observations:

$$\left(\frac{\Delta P}{P_b}\right) \leq 1 \tag{6.16}$$

and

$$\left(\frac{h}{r}\right) \approx \frac{1x10^{-6}}{5x10^{-3}} \approx 2x10^{-4}. \tag{6.17}$$

The pressure difference across the running face of a ring can range from zero, at points in the stroke where ambient pressure surrounds the entire ring, to the same magnitude as the pressure acting on the back of the ring during the early parts of the expansion stroke when high pressure exists on only one side of a ring, as is shown in equation (6.16). In addition, the thickness of the oil film observed between the ring and the groove is typically three orders of magnitude smaller than the radial width of the ring, as is demonstrated in equation (6.17). Combining these results with equation (6.14), the groove friction due to a non-symmetrical pressure gradient is much smaller the groove asperity contact friction,

$$\frac{F_{GFP}}{F_{GFV}} \leq 0.01 << 1. \tag{6.18}$$

Using typical values for engine geometric and operating parameters given in Table 6.1, the relative strength of hydrodynamic friction due to relative motion and boundary contact friction can be simplified to give

$$1x10^{-7} \leq \left(\frac{F_{GFV}}{F_{GFA}}\right) \leq 1x10^{-5}. \tag{6.19}$$

Therefore, the effect of hydrodynamic friction due to relative motion between the ring and groove will also be small compared to asperity contact friction,

$$\frac{F_{GFV}}{F_{GFA}} << 1. \tag{6.20}$$

The groove friction force due to asperity contact is dominant friction force. Thus, hydrodynamic friction is neglected in the remainder of the order-of-magnitude analysis.

6.2.4 The Effect of Groove Friction on Ring Pack Performance

It has been demonstrated in the previous section that groove friction due to asperity contact will dominate groove friction due to hydrodynamic friction. Therefore, to establish an upper bound on the potential effect of groove friction on ring pack performance, it is assumed in the following analysis that the ring is completely seated against one side of the groove, and no oil squeezing between the groove surface and the ring is present to generate hydrodynamic pressure. Under these conditions, all axial force on the ring due to gas pressure and ring inertia will be supported by asperity contact. This situation will lead to the highest possible groove friction force.

Total ring radial load, excluding groove friction, consists of the force due to gas pressure acting on the back of the ring, F_{GR}, and the force due to ring tension, R_T. The force per unit length in the circumferential direction of these quantities is given by

$$F_{GR} = P_b b \tag{6.21}$$

and

$$R_T = \frac{2T}{bB}, \tag{6.22}$$

where T is the ring tension. Total ring radial load can be defined as the summation of the force due to ring tension, gas pressure acting on the back of the ring, and the force due to groove friction. Total ring load is counteracted by a combination of hydrodynamic pressure generated if a lubricant film is present in the groove, asperity contact pressure, and gas pressure acting on the un-wetted running face of the ring. Total ring radial load is

$$F_{ring\ radial\ load} \equiv F_{GR} + R_T \pm F_{GF}. \tag{6.23}$$

Comparing the force due to groove friction with the two other components of ring load,

$$\frac{F_{GF}}{F_{GR}} = a_b\left(\frac{r}{b}\right) \tag{6.24}$$

and

$$\frac{F_{GF}}{R_T} = \frac{a_b b B P_b}{2T} \tag{6.25}$$

are obtained. Combining equations (6.23) through (6.25), the relative contribution of groove friction to total ring load can be estimated, and is given by

$$\frac{F_{ring\ radial\ load}}{F_{GF}} = 1 + \left[\frac{2T}{a_b b B P_b}\right] + \left[\frac{b}{a_b r}\right]. \tag{6.26}$$

The range of engine operating conditions seen by a ring during a cycle is considered by examining two ring load conditions: Maximum ring back pressure representative of the beginning of the expansion stroke and ambient ring back pressure typical of mid-stroke conditions.

In equation (6.26), the relative contributions of groove friction, ring tension, and back pressure, respectively, to ring radial load are given in terms of ring groove friction. By examining the final term in equation (6.26), it is seen that the relative importance of ring back pressure and ring groove friction on ring radial load is independent of ring back pressure, and therefore engine load. Combining equation (6.26) with typical engine operating conditions given in Table 6.1, the relative contributions of groove friction can be estimated, and are given in Table 6.2.

Table 6.2: Relative importance of groove friction on ring radial load

Relative Contribution	Mid-Stroke (P_b = 1 bar)	Expansion Stroke (P_b = 100 bar)
Groove friction	1	1
Ring tension, $2T/(a_b b B P_b)$	29	0.29
Ring back pressure, $b/(a_b r)$	5	5
Groove friction fraction of total ring load (%)	3	16

Examining Table 6.2, it can be seen that groove friction depends on the engine operating conditions, and can be a small but significant proportion of the total ring radial load. The preceding analysis demonstrated that groove friction can be significant relative to total ring load under worst-case conditions. In reality, ring twist and the dynamic behavior of the ring will generally prevent the ring from seating fully against one side of the groove, allowing gas pressure between the ring and groove to decrease groove asperity contact force. Also, any oil film present in the groove may generate hydrodynamic pressure as the ring approaches the groove surface and film thicknesses become very small, further decreasing the groove asperity contact force. Figure 6.2 shows these phenomenons. It should be noted that the analysis in Section 6.2.3 demonstrated that even if hydrodynamic pressure generated by oil squeezing carries a significant portion of the ring axial load, its contribution to groove friction would still be small.

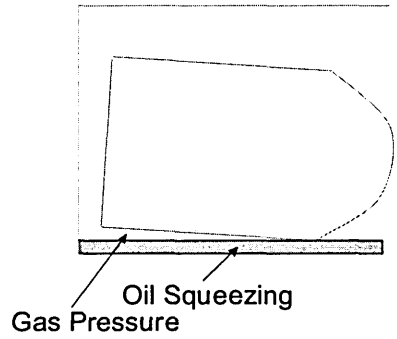

Fig. 6.2: Forces that will reduce groove asperity contact loading

6.3 Modeling a Stick-Slip Condition

Both hydrodynamic friction and boundary friction due to asperity contact were included into a modified version of MIT's ring pack models, described in detail in Section 2.3. The non-conservative nature of groove friction generates a discontinuity in ring radial load when the ring radial velocity changes direction, referred to as a stick-slip condition. This discontinuity will cause convergence problems in the ring pack model solution algorithm. To alleviate this problem, behavior of groove friction is approximated with an exponential function when ring radial velocity is very small,

$$F_{GF} = C \cdot F_{GF},\ C = \frac{V^*}{|V^*|}\left[1 - \exp\left(-a|V^*|\right)\right],\ V^* \equiv \frac{dh}{dt} \cdot \left(\frac{1/N}{h_0}\right), \tag{6.27}$$

where V^* is the non-dimensional ring radial velocity, h_0 is the characteristic oil film thickness, which was chosen as 4μm, N is the engine speed in revolutions per second, and a is an arbitrary positive constant, which is set as large a possible while still allowing convergence of the numerical algorithm. A non-dimensional ring radial velocity was used to keep its value near unity for program numerical stability. In practice, setting a to a value of 500 worked well. The effect of scaling around zero ring radial velocity is shown in Fig. 6.3.

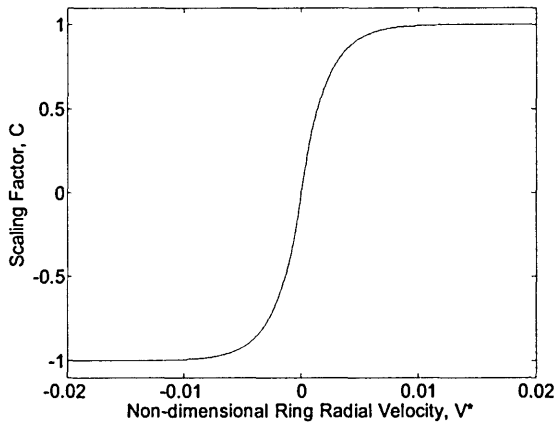

Fig. 6.3: Discontinuity in ring radial force balance due to groove friction

6.4 Effects of Groove Friction on Ring-pack Performance

The effects of groove friction were evaluated on a Waukesha natural gas power generation engine. The geometric details of this engine, and the operating conditions considered, are given in Table 5.1. A modified version of MIT's ring pack friction model was used to evaluate the effect of groove friction on ring pack performance. The contribution of groove friction due to both asperity contact and hydrodynamic shear were included using the methodology described in Section 6.1. The effect of groove friction proved to be significantly smaller than those predicted by the order-of-magnitude analysis in Section 6.2 because oil squeezing and gas pressure between the twisted ring and groove supported the majority of the axial ring load. This phenomenon is shown in Fig. 6.4, in which the ratio of lower groove asperity contact force to the total applied ring axial load is plotted for the top ring for the compression and power stroke. Due to the high gas pressures present in the combustion chamber during the second half of the compression stroke and first half of the power stroke, the top ring remains in contact with the lower groove surface on the piston.

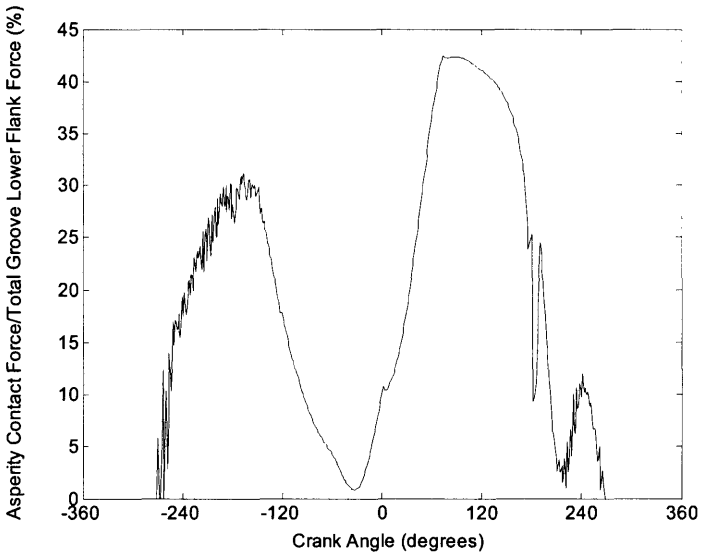

Fig. 6.4: Percentage of top ring axial load supported by asperity contact pressure

As a result of the high proportion of axial ring load carried by a combination of gas pressure and oil pressure, the groove asperity contact force will be substantially lower than the total axial force applied to the ring. It follows that the groove friction force will also be substantially lower than the worst-case scenario analyzed in the order-of-magnitude analysis in Section 6.2.4. From examining Fig. 6.4, groove asperity contact force, and subsequently groove friction, will be approximately five times smaller than that predicted by the order-of-magnitude analysis, since the that analysis assumed that the total ring axial load was supported by asperity contact. Adjusting the order-of-magnitude estimates accordingly, groove friction is expected to account for between approximately 0.5% and 3% of total ring radial load during the stroke.

Although hydrodynamic pressure in practice can carry a substantial fraction of the ring axial load, the effect of hydrodynamic groove friction will remain small in comparison to the groove friction due to asperity contact as was demonstrated by the order-of-magnitude analysis. This

result is shown for the Waukesha engine in Table 6.3 in which the normalized cycle average and maximum values for each component of the groove friction force for the top ring is tabulated.

Table 6.3: Normalized contribution of groove friction sources

Friction Source	Normalized Mean Value Over Cycle	Normalized Maximum Value Over Cycle
Total Ring Radial Load	100	100
Asperity Contact, F_{GFA}	2.72	30.99
Fluid Pressure Gradient, F_{GFP}	0.0288	0.0355
Ring/groove Relative Motion, F_{GFV}	0.00012	0.00018

The groove friction model results for the Waukesha engine agreed strongly with the order-of-magnitude estimates, adjusted for the lower groove asperity contact force. This comparison is shown in Table 6.4.

Table 6.4: Comparison of groove friction model results with order-of-magnitude analysis

Comparison	Order-of-Magnitude Analysis	Simulation Results (Using Mean Value)
$F_{GF}/F_{ring\ radial\ load}$ (%)	~0.5 – 3	2.67
F_{GFP}/F_{GFA} (%)	~1	1
F_{GFV}/F_{GFA} (%)	~0.01	0.046

For the Waukesha engine, the effect of groove friction is significantly smaller than the worst-case scenario considered in the order-of-magnitude analysis. As a result, the effect of groove friction on ring-pack oil film thickness and friction predictions was small, although not negligible. The predicted top ring minimum clearance including groove friction is contrasted with the clearance predicted neglecting its effect in Fig. 6.5. As a side-note, the predicted top ring minimum clearance is higher during parts of the power and exhaust stroke, when high gas pressure is present, than during the intake and compression stroke. This unusual behavior is due to the onset of second ring radial collapse during the first part of the expansion stroke, which allows the oil film left by the oil control ring to be passed directly to the top ring.

In Fig. 6.5, the observed effects of groove friction on ring clearance are a direct result of the non-conservative nature of the groove friction force. When ring clearance is increasing, or the ring is traveling away from the liner, friction will increase the effective ring load. This increase in effective ring load decreases the ring clearance predicted with groove friction included, as can be seen by examining the sections of the oil film trace where ring clearance is increasing. The opposite is also true. When ring clearance is decreasing, the friction force decreases effective ring load, increasing predicted ring clearance with groove friction included. This effect can be seen in the oil film trace when ring clearance is decreasing. The inclusion of groove friction leads to flatter and lower peaks in the ring clearance trace. Groove friction also tends to increase minimum ring clearance predictions.

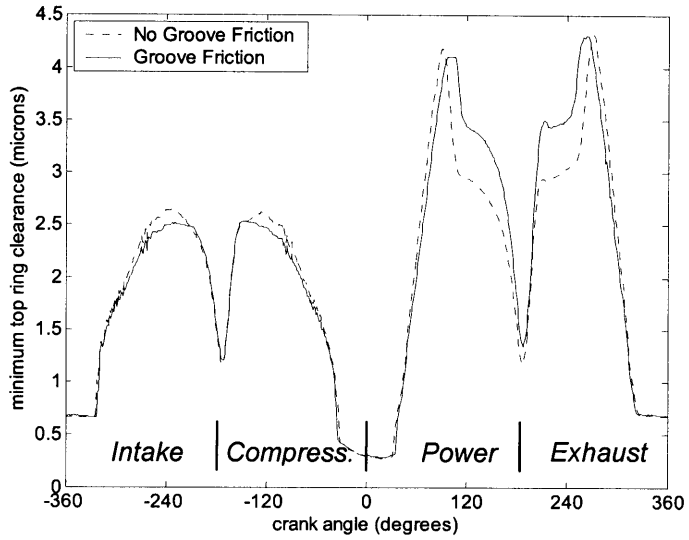

Fig. 6.5: The effect of groove friction on top ring minimum clearance

In Fig. 6.5, it was assumed that a two micron thick oil film existed on all groove surfaces. The effect of groove friction on ring-pack friction and ring clearance depends on the thickness of oil assumed to exist in the groove because it affects how much axial ring load can supported by hydrodynamic pressure. This effect on predicted ring-pack friction is shown in Table 6.5.

Table 6.5: The effect of groove friction on ring-pack FMEP

Condition	Groove Film Thickness (μm)	Change in FMEP (%)
Without groove friction	-	-
With groove friction	5	2.97
With groove friction	2	1.95
With groove friction	1.5	1.52

The inclusion of groove friction increased predicted ring pack friction. As was explained above, including groove friction tends to decrease maximum ring radial clearance, which leads to an increase in hydrodynamic friction. This causes an increase in total ring pack friction. Examining Table 6.5, a decrease in oil film thickness in the groove decreased the predicted ring-pack friction very slightly. This decrease in ring-pack friction was a result of higher hydrodynamic shear stress, and therefore higher hydrodynamic pressure, generated between the ring and groove thereby decreasing the ring axial load supported by asperity contact pressure. This in turn increased maximum ring radial clearance. It should be noted that if oil film thickness in the groove is decreased sufficiently, an increase in predicted ring-pack friction will result as asperity contact begins to carry a larger portion of the ring load. The limiting case is when there in no oil in the ring groove, and all ring axial load will be carried by asperity contact between the ring and groove. Under this condition, maximum ring radial clearance will decrease, and ring-pack friction prediction will be higher than any of the cases presented in Table 6.5.

It should be noted that the observed effects of groove friction on ring-pack FMEP and ring clearance are relatively small. This is expected because asperity contact carries only a small proportion of the axial ring load in the Waukesha engine, as was discussed above.

6.5 General Conclusions

The effect of friction in the ring groove on ring-pack FMEP and ring clearance predictions was considered. An order-of-magnitude analysis demonstrated that the groove friction due to asperity contact will dominate any hydrodynamic friction created by the oil between the ring and groove. The order-of-magnitude analysis also demonstrated that groove friction due to asperity contact could be significant if the groove is starved of lubricant and asperity contact in the groove carries a large proportion of the axial ring load, or if ring radial collapse occurs.

The effect of groove friction proved to be small, but significant, especially in terms of its effect on ring clearance. Including groove friction will decrease ring clearance when the ring is moving away from the liner, and increase ring clearance when the ring is moving towards the liner. In general, with the inclusion of groove friction, maximum predicted ring clearance will decrease and minimum predicted ring clearance will increase. Groove friction could be a significant factor if very accurate ring clearance predictions are required, or if the groove is starved of lubricant, and asperity contact carries a large portion of the ring axial load.

These results also suggest that for minimum ring-pack friction, some lubricant should be present in the ring groove. The lubricant film reduces ring groove friction relative to a dry groove, which would subsequently lower ring-pack friction for reasons discussed in this section. The lubricant film would also reduce groove wear, but could pose problems with oil consumption and carbon build up if excessive lubricant were present in the top ring groove.

7 Summary

The piston ring-pack is a significant contributor to overall engine friction. Therefore, an engine friction reduction strategy should address the friction reduction potential within the piston-ring pack and power cylinder system. The optimization of cylinder liner finish, in this work for reduced friction, is a topic of increased interest as the demands on engine performance, durability and emissions all increase. For this work, optimization of the cylinder liner finish within the limitations of current production honing processes was investigated.

The development of optimization strategies for cylinder liner finish requires accurate modeling of rough surface effects in a lubricated system. The focus of the first half of this work was on improving the characterization and modeling of rough surface asperity contact and oil flow resistance within MIT's current ring-pack models. The previously employed assumption of Gaussian isotropic surface roughness was removed and the ability to model any given surface, both measured and simulated, was included in the ring-pack model. Experimental verification of the surface roughness models developed was performed using a production ring and two different production liner specimens in a reciprocating bench tester, which operated over the whole range of mixed lubrication. Very good agreement was reached between experimental and model friction predictions, providing some confidence in the improved surface roughness models.

The second half of this work was focused on developing ring-pack friction reduction strategies with the use of the improved surface models and MIT's ring-pack program. A Waukesha natural gas engine was the focus of the friction reduction strategy, although the results obtained are general and can potentially be applied to any reciprocating engine.

Ring-pack friction reduction was predicted for surface finishes that were smoother, more negatively skewed or plateau, and for smaller honing cross-hatch angles. A negatively skewed surface is characterized by roughness with flat peaks and deeps valleys. Honing cross-hatch angle is measured perpendicular to the cylinder axis; a 90° cross-hatch angle corresponds to honing grooves running along the length of the cylinder and a 0° cross-hatch angle corresponds to honing grooves running circumferentially around the cylinder. Smoother and more negatively skewed surfaces decreased friction by allowing smaller film thicknesses between the ring and liner before the occurrence of asperity contact. This delayed the onset of mixed lubrication and decreased the amount of boundary contact per cycle, which reduced ring-pack friction. Decreasing honing cross-hatch angle also reduced friction by delaying the onset of mixed lubrication. Lower cross-hatch angles effectively blocked flow at small separations of the ring and liner, which increased the lubricant's effective viscosity during these conditions. This in turn increased the load carrying capacity of the hydrodynamic film, reducing boundary contact and subsequently total ring-pack friction.

The potential for adverse side-effects on oil consumption and durability must also be considered when modifying liner surface finish. Both oil consumption and ring-pack failure through scuffing are complex phenomena that are difficult to predict. Nonetheless, an attempt was made to estimate the relative oil consumption and scuffing tendencies of different liner finishes.

Smoother surfaces, more negatively skewed or plateau surfaces, and surfaces with smaller honing cross-hatch angles all increased the cycle maximum real area of contact between the top ring and liner. This may suggest an increase in scuffing tendency when the surface roughness, skewness, or honing cross-hatch angle is decreased. Cycle average top ring oil film thickness decreases with decreasing surface roughness and skewness, but increases with decreasing honing cross-hatch angle. This suggests making a surface smoother and more plateau may decrease oil consumption, while decreasing honing cross angles on a surface may have the opposite effect and increase oil consumption.

These results suggest that optimizing a surface for lower ring-pack friction may increase its scuffing tendency. However, it interesting to note that a lower friction surface finish may be possible without affecting oil consumption. Reducing surface skewness and honing-cross hatch angle appear to have counteracting effects on oil consumption if cycle average top ring oil film thickness is used as a gauge. To demonstrate the friction reduction potential of liner finish optimization in addition to simply making the finish smoother, the current liner used in the Waukesha engine was substituted with a more plateau liner with a 25° cross-hatch angle and the same surface roughness. A ring-pack friction reduction of only 5% was predicted in large part because the current liner finish in the Waukesha is already well optimized for low friction, for a fixed surface roughness, according to the trends presented in this work. If a cylinder liner with a conventional honing finish and higher cross-hatch angle is compared with a low friction liner with the same roughness, the predicted friction savings will be more substantial, on the order of 10%.

The final section of this work focused on the effects of friction between the ring and piston groove on ring-pack performance. Groove friction was found to decrease the maximum oil film thickness and increase minimum oil film thickness predicted during an engine cycle between the ring and liner. The results suggest that for minimum ring-pack friction, some lubricant should be present in the ring groove. The lubricant film reduces ring groove friction relative to a dry groove, which increases maximum predicted oil film thickness and subsequently lowers ring-pack friction. The lubricant film would also likely reduce groove wear, but could pose problems with oil consumption and carbon build up if excessive lubricant were present in the top ring groove.

This work has developed methodologies to better characterize the effects of surface finish and texture on piston ring-pack performance. The resulting surface roughness models were used in conjunction with MIT's current ring-pack models to develop ring-pack friction reduction strategies through surface finish optimization. The current work focused on surface modifications that are possible using current liner honing procedures. Therefore, the proposed friction reduction strategies will add little or no additional cost to the engine.

8 Recommendations

This work has hopefully laid a foundation upon which future work can be based. Through the process of completing this work, several related areas of study were uncovered. Some of these areas deal with the refinement and improvement of the models developed in this work, and other areas deal with the application of the proposed friction reduction strategies. It is hoped that these recommendations will serve as a rough guideline for future work in this area.

In the short term, it is suggested that further refinements to the asperity contact model be investigated. With the availability of three-dimensional surface measurements, the current asperity contact model should be adapted to use three-dimensional surface parameters as input. This is a natural extension of the work on two-dimensional surface trace analysis presented in this work. Additionally, the determination of asperity contact pressure directly from the measured surface, instead of using a stochastic contact model, should be investigated. This would remove many of the limiting assumptions inherent in the Greenwood and Tripp model, such assuming asperity shape, although it will be more computationally expensive.

There are also refinements to the oil flow resistance model that should be investigated. Inter-asperity cavitation should be included in the MIT flow simulation program to create a more physically correct flow simulation. However, flow and stress factors will subsequently become dependent on the pressure gradient across the ring. This greatly complicates the flow factor approach used in this work, and may require the inclusion of the three-dimensional flow simulation directly into the ring-pack model to allow simultaneous solution of ring-pack lubrication and rough surface flow effects. In addition, the flow simulation should be modified to include the ring surface roughness instead of assuming its surface is smooth. A limiting shear stress was assumed in this work when local asperity contact occurred. Fundamental research is required to verify the accuracy of this assumption. In general, the sensitivity of the flow simulation program to the underlying assumptions made in this work should be investigated further.

Additionally, experimental verification of the aforementioned reduced friction liner finish on a Waukesha engine is necessary. Engine testing will allow the verification of predicted friction reduction amounts and, equally importantly, will allow the quantification of the effects of the proposed liner finish modifications on oil consumption and scuffing tendency. It is suggested that surface textures with successively smoother more plateau finishes and smaller honing cross-hatch angles are tested to determine the optimum surface finish that will lower ring-pack friction while not leading to durability or oil consumption problems. In addition, the surface texture on the piston skirt should be investigated for its friction reduction potential, as piston frictional losses are similar to that of the ring-pack. The surface texture characterization and modeling developed in this work are general, and could be used in conjunction with a piston friction model to better understand surface finish effects, including tooling marks and waviness, on piston skirt friction.

In the long term, if and when laser honing becomes a production reality, it is suggested that the increased flexibility in surface texture modification allowed by laser honing be investigated.

Laser honing enables precise surface features, such as circular pockets or rectangular grooves, to be replicated. Laser honing also allows different finishes to be applied to different sections the cylinder. Thus, the ability to engineer an optimum surface texture is greatly enhanced.

References

[1] Richardson, D. E., "Review of Power Cylinder Friction for Diesel Engines", Internal Document, Cummins Engine Company.
[2] Heywood, J. B., 1988, *Internal Combustion Engine Fundamentals*, McGraw Hill Inc., New York, 729-730.
[3] Sprague de Camp, L., 1970, *The Ancient Engineers*, MIT Press.
[4] Economou, P. N., Dowson, D., Baker, A. J. S., 1979, "Piston Ring Lubrication – Part I: The Historical Development of Piston Ring Technology", Energy Conservation Through Fluid Film Lubrication Technology: Frontiers in Research and Design, Winter Annual Meeting of the ASME, 1-22.
[5] Dowson, D., Economou, P. N., Baker, A. J. S., 1979, "Piston Ring Lubrication – Part II: Theoretical Analysis of a Single Ring and a Complete Ring-Pack, Winter Annual Meeting of the ASME, 23-52.
[6] Rhode, S. M., 1980, "A Mixed Friction Model for Dynamically Loaded Contacts with Application to Piston Ring Lubrication", Proc. Of the 7th Leeds-Lyon Symposium on Tribology, Westbury House, 262.
[7] Dowson, D., Economou, P. N., Baker, A. J. S., 1979, "Piston Ring Lubrication – Part III: The Influence of Ring Dynamics and Twist", Energy Conservation Through Fluid Film Lubrication Technology: Frontiers in Research and Design, Winter Annual Meeting of the ASME, 23-52.
[8] Hu, Y., Cheng, H.S., Arai, T., Kobayashi, Y. and Aoyama, S., 1993, "Numerical Simulation of Piston Ring in Mixed Lubrication – A Nonaxisymmetrical Analysis", ASME Journal of Tribology, 93-Trib-9.
[9] Keribar, R., Dursunkaya, Z., and Flemming, M. F., "An Integrated Model of Ring-Pack Performance", ASME Journal of Engineering for Gas Turbines and Power, **113**, 382-389.
[10] Tian, T., Wong, V. W., Heywood, J. B., 1996, "A Piston Ring-Pack Film Thickness and Friction Model for Multigrade Oils and Rough Surfaces", SAE paper 962032 and SAE Transactions, Journal of Fuels and Lubricants, **105**, pp. 1783-1795.
[11] Tian, T., Noordzij, L. B., Wong, V. W., Heywood J. B., 1996, "Modeling Piston-Ring Dynamics, Blowby, and Ring-Twist Effects", ICE-Vol. 27-2, 1996 ASME Fall Technical Conference, **2**, 67-80.
[12] Greenwood, J. A. and Tripp, J., 1971 "The Contact of Two Nominally Flat Surfaces", Proc. Inst. Mech. Engrs., 185, 625-633.
[13] Patir, N. and Cheng, H. S., 1979, "Application of Average Flow Model to Lubrication Between Rough Sliding Surfaces", ASME Journal of Lubrication Technology, 101, 220-230.
[14] Sato, O., Takiguchi, M., Aihara, T., Seki, Y., Fujimura, K., Tateishi, Y., "Improvement of Piston Lubrication in a Diesel Engine by Means of Cylinder Surface Roughness", SAE Paper 2004-01-0604.
[15] Hill, S. H., Brown, J. R., Hamelink, J. C., 1995, "An Experimental Study of the Effect of Cylinder Bore Finish on Engine Oil Consumption", SAE paper 950938.
[16] Hill, S. H., "Cylinder Bore Finishes and their Effect on Oil Consumption", ASME paper 2001-01-3550.

[17] Bolander, N. W., Steenwyk, B. D., Kumar, A., Sadeghi, F., 2004, "Film Thickness and Friction Measurement of Piston Ring Cylinder Liner Contact with Corresponding Modeling including Mixed Lubrication", ICED Fall Technical Conference Proceedings, ASME Paper ICEF2004-903.
[18] Jocsak, J., Wong, V., Tian, T., 2004, "The Effects of Cylinder Liner Finish on Piston Ring-pack Friction", ASME-ICED Fall Technical Conference Proceedings, ASME Paper ICEF2004-952, 2004.
[19] Waters, Fred, 1996, *Fundamentals of Manufacturing for Engineers*, UCL Press, London, 200.
[20] Hegemier, T., Stewart, M., 1993, "Some Effects of Liner Finish on Diesel Engine Operating Characteristics", SAE paper 930716.
[21] Jeng, Y., 1996, "Impact of Plateaued Surface on Tribological Performance", Tribology Transactions, 39, 354-361.
[22] Lemke, H., 2003, "Characteristic Parameters of the Abbot Curve", MTZ 5/2003, **64**, pp. 438-444.
[23] MAHLE, 2000, "Recommendation for the Specification of Cast Iron Cylinder Bore Surfaces" Technical Information. Publication.
[24] Tian T., Wong, V. W., "Modeling the Lubrication, Dynamics, and Effects of Piston Dynamic Tilt of Twin-land Oil Control Rings in Internal Combustion Engines", ASME-ICED Fall Technical Conference Proceedings, ASME Paper 98-ICE-130.
[25] Hamrock, B. J., 1994, *Fundamentals of fluid film lubrication*, McGraw Hill, New York, pp. 227.
[26] Tian, T., 2002, "Dynamic behaviors of piston rings and their practical impact. Part 2: oil transport, friction and wear of ring/liner interface and the effects of piston and ring dynamics", Proc. Instn Mech Engrs, 216 Part J.
[27] Elderton, P. E. and Johnson, L. J., 1969, "Systems of Frequency Curves", Cambridge Univ. Press, London.
[28] Kotwal, C. A., Bhushan, B., 1996, "Contact Analysis of Non-Gaussian Surfaces for Minimum Static and Kinetic Friction and Wear", Tribology Transactions, 39, 890-898.
[29] Mainsah, E.; Greenwood, J.A.; Chetwynd, D.G, 2001, *Metrology and Properties of Engineering Surfaces*, Springer Verlag, London, 246.
[30] McCool, J.I., 1986, "Comparison of models for the contact of rough surfaces", Wear, **107**.
[31] Greenwood, J. A., 1984, "A Unified Theory of Surface Roughness", Proc. Roy. Soc. Lon., **393**, 133-157.
[32] Montgomery, D. C., Runger, G.C., Norma, F. H., 2001, *Engineering Statistics, Second Edition*, John Wiley and Sons Inc., New York.
[33] Visscher, M., Dowson, D. and Taylor, C. M., 1995 (Elsevier, Amsterdam, 1996), "Surface Roughness Modeling for Piston Ring Lubrication: Solving the Problems" in The Third Body Concept: Interpretation of Tribological Phenomenon, Proc. of the 22nd Leeds-Lyon Symposium on Tribology.
[34] Johnson, K. L., 1985, *Contact Mechanics*, Cambridge University Press, London.
[35] Bair, S., Winer, W. O., 1991, "The High Shear Stress Rheology of Liquid Lubricants at Pressures of 2 to 200 MPa" ASME Journal of Tribology, **114** Paper 91-Trib-9.
[36] Jocsak, J., Tomanik, E., Wong, V. W., Tian, T., 2005, "The Characterization and Simulation of Cylinder Liner Surface Finishes", ASME-ICED Spring Technical Conference Proceedings, ASME Paper ICES2005-1080, 2005.

[37] Hutchings, I. M., 1992, *Tribology: Friction and Wear of Engineering Materials*, Eduard Arnold, London.
[38] Tomanik, E. Nigro, F., 2001, "Piston Ring Pack and Cylinder Wear Modeling" SAE paper 2001-01-0572.

(This page was intentionally left blank)

Appendix A: Derivation of Pearson Frequency Curves

A.1 Derivation of Pearson Frequency Curves

The Pearson system of frequency curves is a curve-fitting system that infers the shape of the probability distribution based on the three discrete statistical parameters: The standard deviation, skewness, and kurtosis of a data set [27,28]. These three parameters are the proportional to the second through fourth moments of the distribution. The nth distribution moment is defined as

$$m_n \equiv \int z^n \phi \, dx, \tag{A.1}$$

where z is an independent variable that represents some measurable quantity of a sample population and ϕ represents the probability distribution of that independent variable. A typical probability distribution curve approaches zero at some upper and lower bound of z, rises and hits a maximum, and decreases at a different rate. Therefore, a curve-fitting method for probability distributions should reflect these characteristics. The curve must be smooth, and its derivative must approach zero at the maximum point, and at both ends. The basic form of the curve-fitting equation that underlies the Pearson system is

$$\frac{d\phi}{dz} = \frac{\phi \cdot (z-a)}{F(z)}, \tag{A.2}$$

where $F(z)$ is some function that describes the distribution [27]. The slope of probability distribution, $d\phi/dz$, is equal to zero at the maximum point, a, and at both ends, $\phi = 0$. Using a Taylor series expansion around zero to determine $F(z)$, it follows that

$$\frac{1}{\phi}\frac{d\phi}{dz} = \frac{(z-a)}{\phi \cdot F(z)} = \frac{(z-a)}{\phi \cdot (b_0 + b_1 z + b_2 z^2 + \ldots)}, \tag{A.3}$$

where b_n is the nth coefficient of the Taylor series expansion [27]. The recursion formula,

$$a m_n + n b_0 m_{n-1} + (n+1) b_1 m_n + (n+2) b_2 m_{n+1} + \ldots = -m_{n+1}, \; n = 0, 1, 2, \ldots, \tag{A.4}$$

is obtained by multiplying both sides of equation (A.3) by $\phi \cdot F(z)$, integrating by parts, and applying the boundary condition that the probability distribution tends to zero at some upper and lower bound.

By setting the area under the distribution (0-th moment) to unity, setting the mean of the distribution (1st moment) to zero, and neglecting moments higher than fourth-order, the system of equations given by equations (A.5) – (A.8) is produced. Higher order moments of the distribution are neglected because they will make the curve-fit very sensitive to extreme values in the sample population [27].

$$\begin{bmatrix} a+b_1 & 0 & 0 & 0 \\ b_0 & 3b_2 & 0 & 0 \\ 0 & a+3b_1 & 4b_2 & 0 \\ 0 & 3b_0 & a+4b_1 & 5b_2 \end{bmatrix} \cdot \begin{bmatrix} 1 \\ m_2 \\ m_3 \\ m_4 \end{bmatrix} = \begin{bmatrix} 0 \\ -m_2 \\ -m_3 \\ -m_4 \end{bmatrix} \qquad \text{(A.5) – (A.8)}$$

The system of equations given by equations (A.5) – (A.8) is easily solved for the first three coefficients of the Taylor series expansion and a when the moments of the distribution (standard deviation, skewness, and kurtosis) are known. The probability distribution is then defined by

$$\phi(z) = \exp\left[\int \frac{(z-a)dz}{b_0 + b_1 z + b_2 z^2}\right]. \qquad \text{(A.9)}$$

The solution of the integral in equation (A.9) will take on different values depending on the roots of the quadratic equation in the denominator of the integrand. This property leads to different forms for the probability distribution depending on the roots of the quadratic equation. By examining these roots, a criterion factor, κ, that determines the form of the solution can be defined in terms of the skewness and kurtosis of the distribution [28].

$$\kappa \equiv \frac{b_1^2}{b_0 b_2} = \frac{Sk^2(K+3)^2}{4(2K-3Sk^2-6)\cdot(4K-3Sk^2)}. \qquad \text{(A.10)}$$

There are three main types of curves that arise from the roots of the quadratic denominator. The first main type occurs when κ is negative, meaning the roots are real and of opposite sign. The second main type occurs when κ is between zero and one, meaning the roots are real and of the same sign. The third main type occurs when κ is greater than one, meaning the roots are imaginary. There are also transition curves that deal with the cases when κ is equal to exactly zero or one. The probability distribution functions for all the curves necessary for this work are given in Table A.1. In Table A.1, c_n is a constant that is a function of the standard deviation, skewness, and kurtosis of the distribution. Formulae for determination of the constants given in the equations in Table A.1 are detailed below for each curve type [28].

Table A.1: Equations for probability density functions

Curve Number	κ	*Sk*	*K*	Equation
Main Types				
I	<0	-	-	$\phi(z) = c_1(1+z/c_2)^{c_3}\cdot(1-z/c_4)^{c_5}$
IV	$0 \rightarrow 1$	-	-	$\phi(z) = c_1\left[1+(z/c_2-c_3/c_4)^2\right]^{-c_5-c_3\arctan(z/c_2-c_3/c_4)}$
VI	>1	-	-	$\phi(z) = c_1(1+z/c_2)^{-c_3}\cdot(1+z/c_4)^{c_5}$

Curve Number	κ	*Sk*	*K*	Equation
Transition Types				
Gaussian	0	0	3	$\phi(z) = c_1 \exp\left(\frac{-z^2}{2\sigma^2}\right)$
II	0	0	< 3	$\phi(z) = c_1(1 - z^2 / c_2^2)^{c_3}$
VII	0	0	> 3	$\phi(z) = c_1(1 + z^2 / c_2^2)^{-c_3}$

A.2 Curve Constants

A.2.1 Curve Type I

For convenience, a sixth constant

$$r \equiv \frac{6(K - Sk^2 - 1)}{(6 + 3Sk^2 - 2K)} \tag{A.11}$$

is used to describe the five constants, c_1 to c_5, required to uniquely define curve type I given in Table A.1. The five constants are determined by equations (A.12) – (A.16):

$$(c_3 + 1)/c_2 = (c_5 + 1)/c_4, \tag{A.12}$$

$$c_2 + c_4 = \frac{\sigma}{2}\sqrt{Sk^2(r+2)^2 + 16(r+1)}, \tag{A.13}$$

$$c_5, c_3 = \frac{1}{2}\left[r - 2 \pm r(r+2)\sqrt{\frac{Sk^2}{Sk^2(r+2)^2 + 16(r+1)}}\right], \tag{A.14}$$

and

$$c_1 = \frac{1}{c_2 + c_4} \cdot \frac{(c_3 + 1)^{c_3}(c_5 + 1)^{c_5}}{(c_3 + c_5 + 2)^{c_3 + c_5}} \cdot \frac{\Gamma(c_3 + c_5 + 2)}{\Gamma(c_3 + 1)\Gamma(c_5 + 1)}. \tag{A.15}$$

In equation (A.14), c_5 is the positive root when *Sk* is positive. In equation (A.15) $\Gamma(z)$ is the gamma function,

$$\Gamma(z) \equiv \int_0^\infty e^{-x} x^{z-1} dx, \tag{A.16}$$

which is the continuous equivalent of the factorial function. It should be noted that equation (A.15) may present some numerical difficulties because the gamma function is exponential in

nature and can take on very large values. Therefore, equation (A.15) should be evaluated using logarithms.

A.2.2 Curve Type IV

The constant given in equation (A.11) is also used for convenience to describe the three constants, c_1 to c_3, required to determine curve type IV, given in Table A.1. The three constants are determined by equations (A.17) – (A.21):

$$c_2 = \frac{\sigma}{4}\sqrt{-16(r+1) - Sk^2(r+2)^2}\,, \tag{A.17}$$

$$c_3 = \frac{-r(r+2)Sk}{\sqrt{-16(r+1) - Sk^2(r+2)^2}}\,, \tag{A.18}$$

$$c_4 = -r, \tag{A.19}$$

$$c_5 = \frac{2-r}{2}\,, \tag{A.20}$$

and

$$c_1 = \frac{1}{c_2 \exp(-c_3\pi/2)\int_0^{\pi}\exp(c_3\phi)\sin^{-r}(\phi)d\phi}\,. \tag{A.21}$$

A.2.3 Curve Type VI

Using the constants defined in equations (A.11) and (A.22) for convenience, the five constants, c_1 to c_5, required to determine curve type VI given in Table A.1 are defined in equations (A.23) to (A.26):

$$a \equiv \frac{\sigma}{2}\sqrt{Sk^2(r+2)^2 + 16(r+1)^2}\,, \tag{A.22}$$

$$c_5, (-c_3) = \frac{1}{2}\left[r - 2 \pm r(r+2)\sqrt{\frac{Sk^2}{Sk^2(r+2)^2 + 16(r+1)}}\right], \tag{A.23}$$

$$c_2 = \frac{a(c_3 - 1)}{(c_3 - 1) - (c_5 + 1)}\,, \tag{A.24}$$

$$c_4 = \frac{a(c_5+1)}{(c_3-1)-(c_5+1)}, \tag{A.25}$$

and

$$c_1 = \frac{(c_5+1)^{c_5}(c_3-c_5-2)^{c_3-c_5}}{a(c_3-1)^{c_3}} \cdot \frac{\Gamma(c_3)}{\Gamma(c_5+1)\Gamma(c_3-c_5-1)}. \tag{A.26}$$

In equation (A.23), c_5 is the positive root and $(-c_3)$ is the negative root, respectively. Similar to equation (A.15), (A.26) involves division of gamma functions, which are exponential in nature. Therefore, equation (A.26) should be evaluated logarithmically.

A.2.4 Gaussian Transition Curve

The Gaussian curve is the appropriate transition curve when the kurtosis of the distribution is three, and the skewness of the distribution is zero. The constant, c_1, required to define the normal curve given in Table A.1 is simply

$$c_1 = \frac{1}{\sigma\sqrt{2\pi}}. \tag{A.27}$$

A.2.5 Type II Transition Curve

The three constants, c_1 to c_3, required to determine the type II transition curve given in Table A.1 are defined by equations (A.28) to (A.30):

$$c_3 = \frac{5K-9}{2(3-K)}, \tag{A.28}$$

$$c_2 = \sqrt{\frac{2\sigma^2 K}{3-K}}, \tag{A.29}$$

and

$$c_1 = \frac{1}{c_2\sqrt{\pi}} \cdot \frac{\Gamma(c_3+3/2)}{\Gamma(c_3)}. \tag{A.30}$$

Like equations (A.15) and (A.26), equation (A.30) should be evaluated logarithmically as result of the division of two gamma functions.

A.2.6 Type VII Transition Curve

The three constants, c_1 to c_3, required to determine the type VII transition curve given in Table A.1 are defined by equations (A.31) to (A.33):

$$c_3 = \frac{5K-9}{2(K-3)}, \tag{A.31}$$

$$c_2 = \sqrt{\frac{2\sigma^2 K}{K-3}}, \tag{A.32}$$

and

$$c_1 = \frac{1}{c_2\sqrt{\pi}} \cdot \frac{\Gamma(c_3)}{\Gamma(c_3 - 1/2)}. \tag{A.33}$$

Similar to equations (A.15), (A.26), and (A.30), equation (A.33) should be evaluated logarithmically as result of the division of two gamma functions.

Appendix B: Flow Factor Curve Fits

Regression was employed to determine best-fit curves for the flow and stress factors derived for various liner surfaces using MIT's flow factor program. These best-fit curves could be easily differentiated, and included into the ring-pack program. The flow factors are given as a function of non-dimensional surface separation,

$$H = h / R_q. \tag{B.1}$$

The geometric flow factor for all surfaces proved to be closely approximated using a uniform distribution,

$$\phi_g = \frac{1}{\sqrt{6}H} + \frac{1}{2} + \frac{H}{2\sqrt{6}} + \frac{H^2}{36}, H > 0.5. \tag{B.2}$$

The remaining five flow and stress factors were approximated by equations (B.3) through (B.7):

$$\phi_p = 1 - \alpha_1 / H - \alpha_2 / H^2 - \alpha_3 / H^3, H > 0.5, \tag{B.3}$$

$$\begin{aligned} \phi_s &= H^{\alpha_4} \exp\left(\alpha_5 + \alpha_6 H + \alpha_7 H^2\right), 0.5 < H < 5 \\ &= \exp\left(\alpha_8 + \alpha_9 H\right) H > 5, \end{aligned} \tag{B.4}$$

$$\phi_{fp} = 1 - \exp\left(\alpha_{10} + \alpha_{11} H\right) H > 0.5, \tag{B.5}$$

$$\begin{aligned} \phi_{fs} &= H^{\alpha_{12}} \exp\left(\alpha_{13} + \alpha_{14} H + \alpha_{15} H^2\right), 0.5 < H < 5 \\ &= \exp\left(\alpha_{16} + \alpha_{17} H\right) H > 5, \end{aligned} \tag{B.6}$$

and

$$\begin{aligned} \phi_{fg} &= 1 + H^{\alpha_{18}} \exp\left(\alpha_{19} + \alpha_{20} H + \alpha_{21} H^2\right), 0.5 < H < 5 \\ &= 1, H > 5. \end{aligned} \tag{B.7}$$

The 21 required coefficients for the flow and stress factors in equations (B.3) through (B.7) were determined using regression analysis. Values for these coefficients are given for the liner surfaces analyzed in this work in Table B.1. The plateau and slide honed surfaces are actual measured production liner surfaces finishes, and the remaining surfaces are artificial surfaces created using a statistical surface generator. Surface roughness parameters for each surface are also included in Table B.1.

Table B.1: Regression coefficients for flow and stress factors

Parameter	Plateau Honed	Slide Honed	Simulated 30° hone angle	Simulated 60° hone angle	Simulated 90° hone angle
R_q [μm]	0.84	0.49	0.5	0.5	0.5
R_k [μm]	0.74	0.39	0.6	0.6	0.6
R_{vk} [μm]	1.85	1.85	1.0	1.0	1.0
R_{pk} [μm]	0.25	0.28	0.1	0.1	0.1
Sk	-2.79	-3.85	-0.5	-0.5	-0.5
Hone Angle	40	40	30	60	90
α_1	-0.924	-1.03	-1.14	-0.712	-0.123
α_2	0.461	0.502	0.453	1.28	1.41
α_3	-0.0436	-0.049	0.181	0.036	0.928
α_4	1.4	2.03	1.12	0.772	0.683
α_5	1.29	1.64	0.727	0.28	0.197
α_6	-1.52	-1.83	-0.462	-0.341	-0.469
α_7	0.115	0.123	-0.0156	-0.015	-0.00215
α_8	-0.588	-0.514	1.02	0.478	-0.329
α_9	-0.125	-0.139	-0.243	-0.212	-0.162
α_{10}	0.34	0.34	0.26	-0.036	-0.588
α_{11}	-0.66	-0.66	-0.629	-0.699	-0.714
α_{12}	8	3.7	1.47	1.69	0.23
α_{13}	12.3	5.61	1.97	1.89	-0.51
α_{14}	-12	-4.79	-0.5	-0.57	1.53
α_{15}	1.38	0.406	-0.133	-0.138	-0.393
α_{16}	-1.3	0.499	0.125	0.523	-0.232
α_{17}	-0.315	-0.588	-0.31	-0.444	-0.414
α_{18}	2.41	2.24	2.05	1.99	2.23
α_{19}	6.7	4.57	6.14	5.87	6.3
α_{20}	-5.61	-3.56	-5.25	-5.16	-5.49
α_{21}	0.572	0.261	0.563	0.551	0.577